The University of Manitoba

Novel Schemes for Sidelobe Reduction in Aperture Antennas

by

Walid Afif Chamma

A Thesis
Submitted to the Faculty of Graduate Studies
in Partial Fulfillment of the Requirements for the Degree
of Master of Science in Electrical Engineering

Department of Electrical Engineering
Winnipeg, Manitoba
Canada

November 1987

ISBN 0-315-44122-4

NOVEL SCHEMES FOR SIDELOBE REDUCTION IN APERTURE ANTENNAS

BY

WALID AFIF CHAMMA

A thesis submitted to the Faculty of Graduate Studies of
the University of Manitoba in partial fulfillment of the requirements
of the degree of

MASTER OF SCIENCE

ABSTRACT

This thesis makes use of a well-known integral equation to study numerically different schemes for reducing side and back lobe power levels in the far field patterns of aperture antennas such as waveguides, pyramidal horns, and cylindrical reflectors. A review of the work done in reducing the side and back lobe levels of multi- and hybrid-mode horns and more recently, aperture-matched horns is presented first. The scattering problem is then formulated for an arbitrary shaped cylinder excited by a magnetic line source. The integral equation resulting from this formulation is then transformed into a moment-method problem.

The performance of aperture matching of waveguides, horns, and cylindrical reflectors, with their electrical dimensions and operating frequencies as variables, is reported on the basis of an extensive use of a moment-method computer program. Aperture matching is done by attaching different geometric shaped flanges to the edges of these antennas such as flat, elliptic, and spiral flanges. These shapes are chosen so as to reduce the magnitude of the diffraction coefficient at the edges which in turn affects side and backlobe levels. A reduction of 5 to 15dB in these lobe levels together with broader beam widths is reported for the cases of the aperture-matched waveguides and horns. A similar reduction in the far lobe levels with slightly narrower beam width is observed for aperture-matched cylindrical parabolic reflectors.

Two other alternative approaches for sidelobe and backlobe level reduction of horn antennas are then introduced. The first approach is to shield the edges of the antenna by the use of proper metallic structures, hence isolating the edge diffracted fields of the antenna and minimizing their destructive interference. A reduction of more than 20dB in the sidelobe levels is achieved in the so called "capped-edge" horn. The second approach deals with introducing an active source, placed at an optimum position inside the horn, and excited with proper phase relative to the edge field. These active sources which are simulated by magnetic line sources will radiate fields that will add destructively with the fields incident from the feed waveguide on the edges of the horn. A reduction of more than 20dB is achieved with the so called "active loaded" horn.

ACKNOWLEDGEMENTS

The author wishes to express his appreciation to Dr. M. Hamid who proposed and supervised the research throughout.

The financial assistance by the National Research Council of Canada and the Department of Electrical Engineering of the University of Manitoba are gratefully acknowledged.

Special acknowledgement go to Dr. M. Sanad for many profitable and helpful discussions.

TABLE OF CONTENTS

List of Figures

CHAPTER I

Introduction

A broad class of antennas commonly known as aperture antennas are those in which radiation is considered to occur from an aperture. Examples are reflector antennas, waveguides, and horn (flared waveguides)antennas. An aperture type antenna must have an aperture size of at least several wavelengths in order to have a high gain. Typically, the E-plane pattern associated with an optimum-gain design of these antennas has high side and backlobe levels due to large edge diffracted fields.

Horns and waveguides are mainly used as primary feeds for reflectors, and their high side and backlobe levels affect the performance and efficiency of the reflector antenna as a whole. Aside from the power loss due to the feed spillover, the thermal energy from the spillover region contributes to the reflector antenna noise temperature and provides an additional reason for its minimization. To maximize the antenna gain, one needs a uniform illumination over its aperture, which in turn requires a feed pattern, as shown in Fig.-1.1. Such a feed pattern maximizes the gain but at the same time causes a high edge illumination of the reflector. This high edge illumination gives high sidelobes, thus deteriorating the reflector performance. An ideal feed pattern therefore must generate a nearly uniform illumination and a nearly zero edge illumination. Such a feed must have relatively low side and backlobe levels. Extensive work has been done to reduce these levels. One approach is to reduce the magnitude of the fields incident on the edges of the feed horn from the feed waveguide. This was done by Potter [1] in designing a dual-mode horn as shown in Fig.-1.2. The basic concept is to introduce a metallic step in the wall of a conical horn in order to excite a TM_{11} mode which travels independent of the incident TE_{11} mode. The position of the step is such that the two modes with their relative phases and amplitudes adjust to lower the electric field at the edges, hence suppressing the

E-plane sidelobes. Later, Potter and Ludwing [2] analyzed the possibilities of beam shaping through the superposition of higher order modes in conical horns. About the same time, Jensen [3] described the extension of the multimode technique to pyramidal horns. In this case, the dominant mode, of course, is the TE_{10} mode, while the appropriate higher modes are a mixture of TE_{12} and TM_{12} modes. Turrin [4] combined a very compact TM_{11} mode transducer and a circular horn to form a small prime focus feed possessing all the attributes of a multimode horn. Here, generation of the TM_{11} mode occurs due to an abrupt flare angle change in the guide. Another simple method of obtaining a dual-mode feed is done with an internal bifurcation Fig.-1.3 as reported by Collin and Schilling [5]. Their design depends on the distance between the aperture and the internal waveguide to obtain the correct addition of the two modes at the aperture. Since the dominant and the desired higher order modes propagate with different phase velocities as they travel from the point of the mode generation to the horn aperture, they will arrive in the correct phase only at one frequency. For this reason, bandwidth is quite limited, and this appears to be the principal disadvantage of the multimode horns. Nevertheless, one can achieve improved pattern performance over about ten percent frequency band using a carefully designed dual-mode horn.

Another simple and effective dual-mode horn was developed by Satoh [6], shown in Fig.-1.4. The Satoh horn uses a dielectric ring mounted on the flared wall of the horn. A bandwidth of 1.5:1 is attributed to the use of the dielectric ring instead of a metallic discontinuity.

A recent extension of the Satoh horn has been developed by Wong [7] involving two concentric dielectric rings placed in a conical horn as shown in Fig.-1.5, and a wider bandwidth was achieved compared to Satoh's single ring horn.

Reduction of the edge-diffracted fields over a broader frequency was achieved also by hybrid-mode feeds. These structures include the dielectric loaded circular waveguide [8], and the corrugated waveguide or horn shown in Fig.-1.6 [9]. The dielguide [10], where a low permitivity dielectric cone loading the horn and extends

beyond the horn aperture and all the way to the subreflector of a cassegrainian reflector antenna, to compromise between illumination uniformity and the energy lost in spillover. The dielectric filled conical horn is introduced by Lier [11] and is shown in Fig.-1.7. Dielectric lined horn [12] shown in Fig.-1.8, and the absorber lined horn [13] also use the concept of hybrid mode generation for sidelobe level reduction and achieving axial symmetry. In such horns both TE_{11} and TM_{11} locked components of the fundamental HE_{11} mode satisfy the same boundary conditions at the walls of the horn, and thus travel together as a new single hybrid mode. Under balanced hybrid-mode conditions the transverse fileds of the HE_{11} mode in the corrugated waveguide shown in Fig.-1.9 [5] are given by

$$\begin{aligned} E_r &= J_0(k_0 r)\cos(\phi) \\ E_\phi &= -J_0(k_0 r)\sin(\phi) \\ H_r &= -Y_0 E_\phi \\ H_\phi &= Y_0 E_r \end{aligned} \tag{1.1}$$

from which we find that $E_x = J_0(k_0 r)$ and $E_y = 0$, where E_r and H_r are the radial components of the electric and magnetic fields, respectively. E_ϕ and H_ϕ are the polar components of the electric and magnetic fields, respectively. Y_0 is the free space intrinsic admittance, k_0 is the free space wave number, and J_0 is the zero order Bessel function. The above expression for the mode pattern satisfies the so called Rumsey's conditions and radiates with very little cross polarization. Rumsey claimed that for no cross polarization, the aperture field in a horn must have the electric and magnetic fields related as in a plane wave [14].

In corrugated waveguides the **E** and **H** fields are found to be identical in form and satisfy the relation $\mathbf{E} = j\eta\mathbf{H}$ where η is the intrinsic impedance of free space. A study of the structure of these fields also led to the hypothesis that waves could be confined in a cylindrical metal tube, provided that the walls are corrugated either circumferentially or longitudinally with resonant slots. It was found [15], in

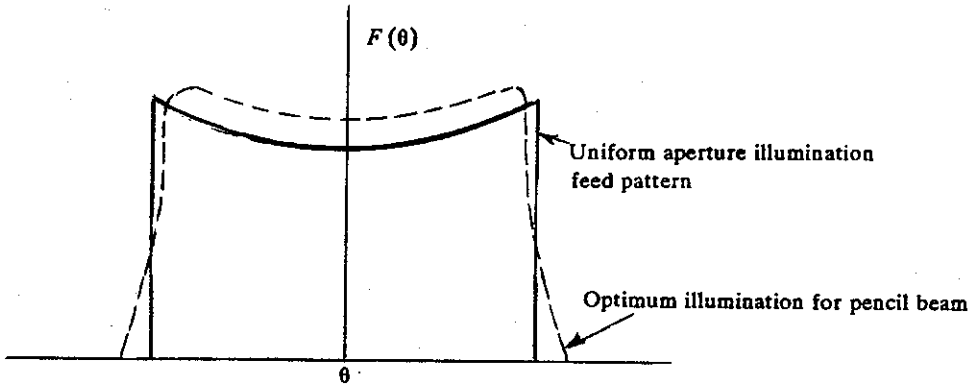

Fig.-1.1 A feed pattern of the optimum form.

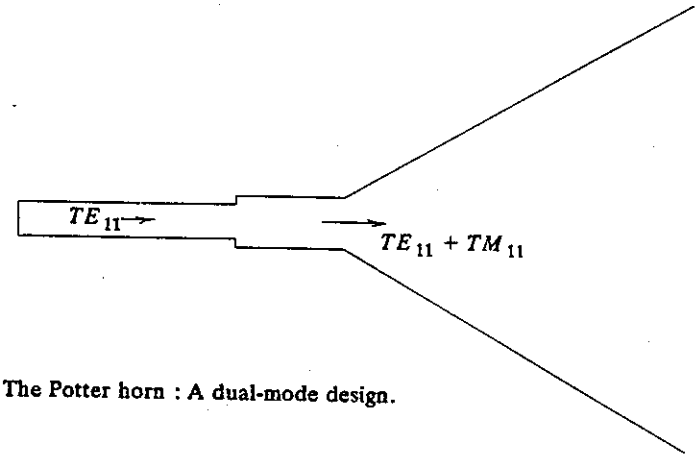

Fig.-1.2 The Potter horn : A dual-mode design.

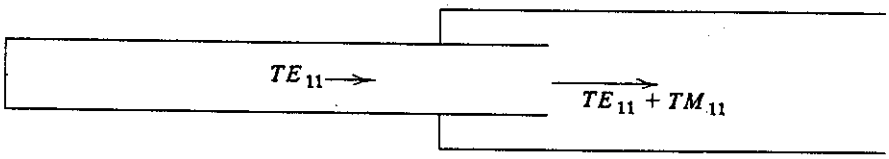

Fig.-1.3 A dual-mode horn design by Collin and Schilling.

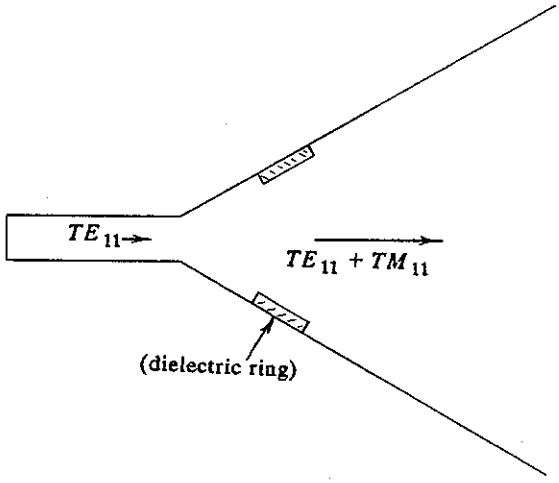

Fig.-1.4 A dual-mode horn design by Satoh.

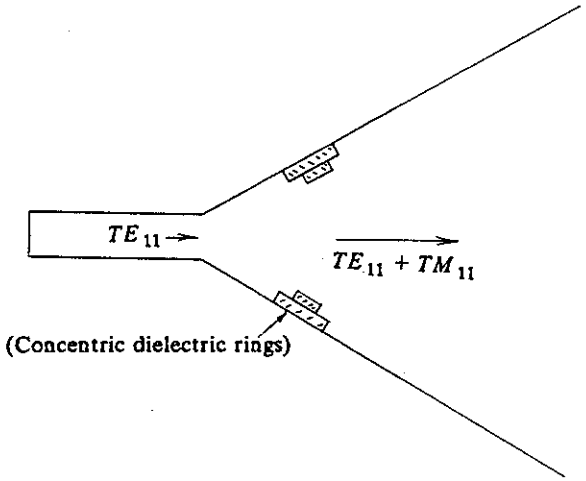

Fig.-1.5 A dual-mode horn design by Wong.

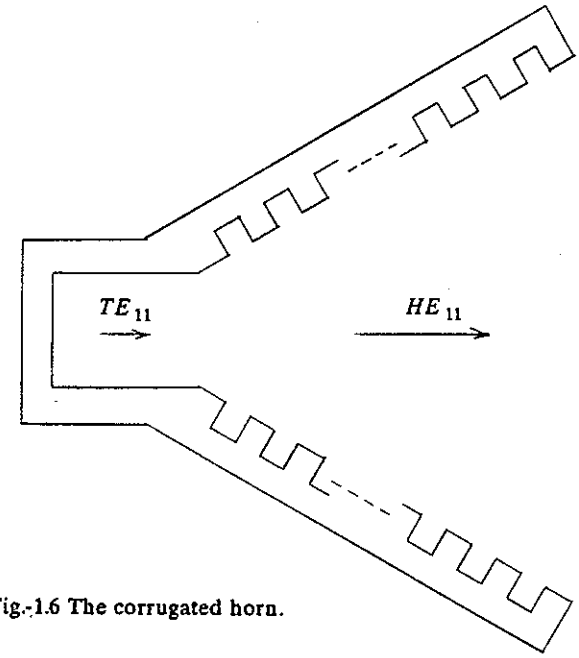

Fig.-1.6 The corrugated horn.

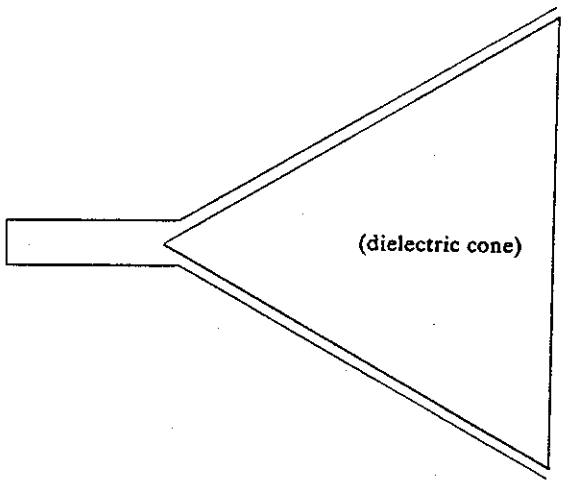

Fig.-1.7 A hybrid-mode horn design by Lier.

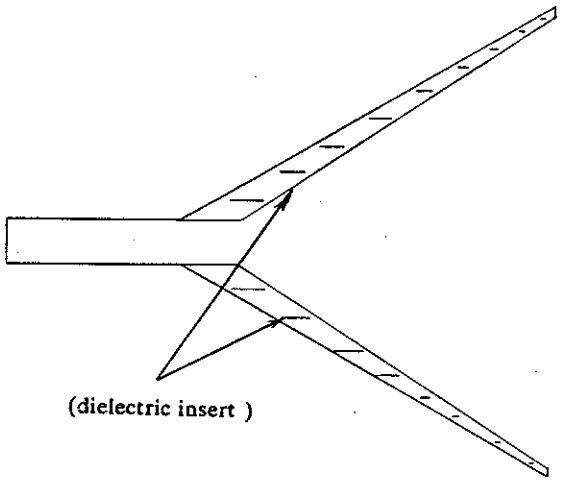

Fig.-1.8 Dielectric lined horn.

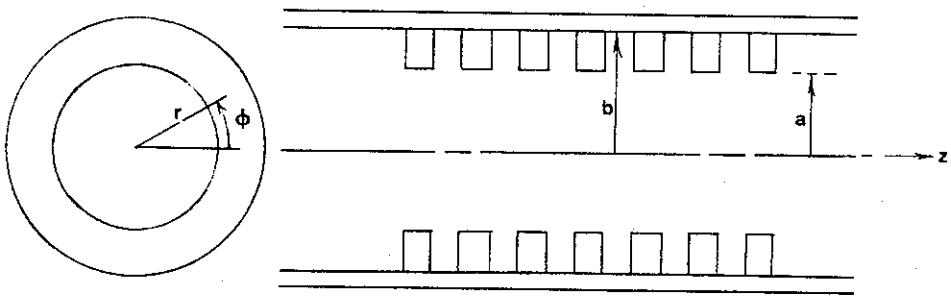

Fig.-1.9 A corrugated circular waveguide.

particular, that the required surface reactance X_ϕ and X_z on the inner wall of the supporting waveguide, defined as

$$X_\phi = -jE_\phi/H_z \quad \text{and} \quad X_z = jE_z/H_\phi \tag{1.2}$$

where the subscripts refer to a circular cylindrical system of coordinates (ρ,ϕ,z), should satisfy the relation $X_\phi X_z = -\eta^2$. Thus to match X_ϕ and X_z at every point, the boundary must be anisotropic. This requirement may be realized in practice with corrugated metal surfaces. For example, a cylindrical surface with circumferential slots may be designed so that $H_\phi = 0$ at the surface. Also the edges of flanges between slots require $E_\phi = 0$. With sufficient slots per wavelength, the structure approximates a continuous anisotropic surface with $X_\phi = 0$ and $X_z = \infty$. It will be noted that these boundaries affect the **E** and **H** fields in the same way, in agreement with the fact that the fields are identical. A second result follows immediately by reciprocity: balanced hybrid modes radiating from the focal plane must illuminate the paraboloid aperture without cross-polarization. Consequently, the radiation fields of these modes had to possess axial symmetry of the polarization. Hence, using specially designed corrugated surfaces on the inner horn walls will force the energy away from the horn walls in the *E*-plane and the boundary conditions accomplish the same in the *H*-plane resulting in increased antenna efficiency [16].

When looking back at the concept of operation of the types of horns just discussed above it might seem at a first glance that the multimode and corrugated horns accomplish similar results, namely axisymmetric radiation patterns, by quite different means. In reality, the modal contents of the fields in the two cases are, with one important difference, the same. In Potter's multimode horn, TE_{11} and TM_{11} modes have different phase velocities by virtue of the fact that the modes have different cutoffs, since the boundary conditions on **E** and **H** are not the same. In corrugated horn, however, a hybrid mixture of TE_{11} and TM_{11} waves behaves as a single mode, in which both components propagate with the same velocity, resulting in a wider operating bandwidth. Given an application can afford the complexities of such a design, and construction, the corrugated horn can provide significantly better

performance than a conventional horn over a rather broader frequency band of 2:1.

Reduction of side and backlobe levels in aperture antennas is done also in "tunnel" antennas [17]. The most common form of the tunnel antenna is a reflector type antenna with a tunnel or shroud extending out from the reflector. The tunnel is lined with absorbent material to minimize the radiated off-axis energy. The object of the tunnel is to reduce the amount of energy spilled over the main dish and subreflector. The sidelobe radiation is due entirely to the field illuminating the edges of the tunnel. The tunnel is placed in such a way around the antenna as to obstruct the antenna's original sidelobes as shown in Fig.-1.10. The choice of tunnel length would appear to be that for which the illumination from the two sources(the main beam from the parabolic reflector and the edge of the tunnel) is about the same. It is observed in such antennas that although there is a reduction in sidelobe level with increase in length of the tunnel, experimental investigation [18] proves that there is a decrease in the gain of the main beam as the tunnel length is increased. Corrugated horn millimeter wave antennas with absorber tunnels have been also developed for communication systems, and a significant reduction in sidelobes down to more than 60dB is achieved.

An approach which eliminates the troublesome edge diffraction involves reducing the aperture edge diffraction itself [19] [20], rather than reducing the incident field on the aperture, as in the case of dual and hybrid-mode horns. This is accomplished by adding aperture curved surfaces which form smooth matching sections between the horn modes and the free space radiation. Burnside [19] designated this type of horns as "aperture-matched" horn shown in Fig.-1.11. These rolled edges allow much of the energy striking the edge to travel along the curved surface gradually shedding energy into the sidelobe and backlobe regions. In addition, the curved surfaces decrease the amount of energy reflected back to the throat of the horn resulting in a much lower voltage standing-wave ratio (VSWR) [19]. Elliptic cylinder sections were attached to the edges of a conventional horn. It was mentioned also that aperture matching can be achieved by the use of arbitrary convex shapes which are attached to the horn such that the junction forms a smooth surface to the touch.

Investigation of such shapes is done in this thesis. Because of the frequency dependence of dual-mode horns and the complexity and cost of corrugated horns, Burnside [19] claimed that a horn with improved pattern and impedance performance can be achieved by his "aperture-matched" horn without greatly sacrificing the size and bandwidth or increasing the cost.

The curved edge concept has been used for parabolic reflectors for many years for purposes of mechanical strength and improved electrical performance. Rolled edges were used for mechanical reasons to hold the shape of the reflector at the edge. This rolled edge had a very small radius and is very close to being an ordinary sharp edge. Recently, curved edges were introduced [21] for compact range measurements. This involved the use of a curved edge attached to a parabolic reflector and has an electrical size large enough for such an application as shown in Fig.-1.12. Prior to that, the discontinuity at the edge of the reflector interrupted the normal flow of currents, producing stray radiation not in phase with the collimated radiation [22]. This convex curved edge, when added, forces the diffracted field away from the test area causing a more uniform near field distribution.

Although the aperture modification suggested can be applied to a wide variety of horns and reflectors, this thesis focuses on two dimensional structures consisting of E-plane sectoral horns (whose pattern analysis is almost identical to that of the E-plane pyramidal horns), rectangular waveguides, and cylindrical parabolic reflectors. Our analysis of these structures neglects any coupling effects between E- and H-planes.

Chapter II presents the numerical formulation of the problem of scattering by arbitrary shaped cylinders. The integral equation resulting from this formulation is transformed into a moment method problem, where an appropriate computer program is written and the problem is solved numerically. Chapter III deals with the results obtained using the computer program for the far field radiation patterns of waveguides and horns after adding different curved shapes to their apertures, and a related discussion is presented at the end of the chapter. Chapter IV extends the

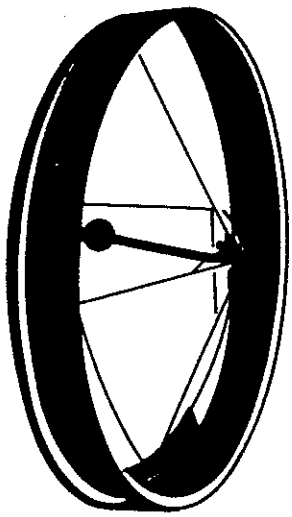

Fig.-1.10 A "Tunnel" reflector antenna.

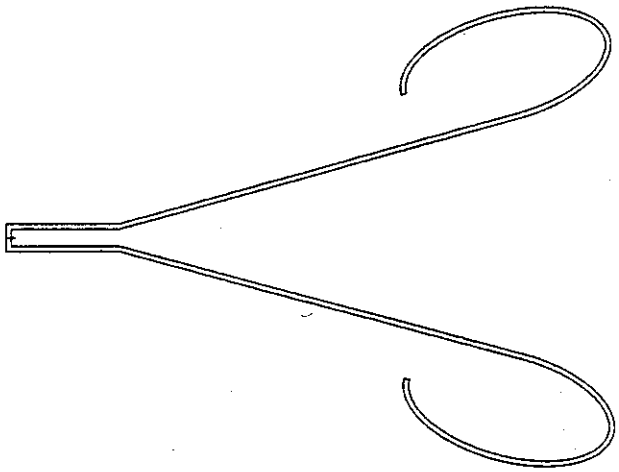

Fig.-1.11 Ellipse aperture-matched sectoral horn.

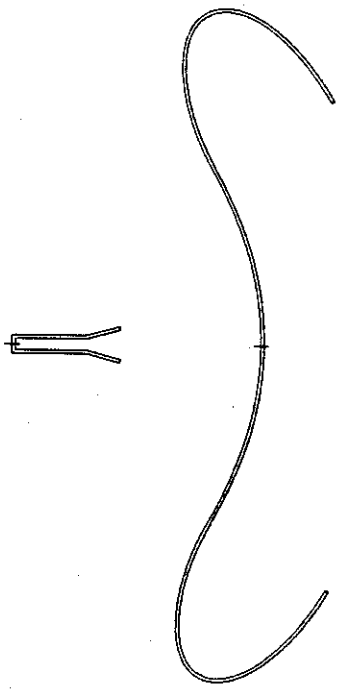

Fig.-1.12 Ellipse aperture-matched cylindrical reflector.

study in Chapter III to the far field patterns of matched cylindrical parabolic reflectors. Chapter V presents a preliminary investigation of the capped edge horn antenna. Chapter VI presents the concept of active loading in reducing the side and backlobe levels in horn antennas. While Chapter VII deals with the main conclusions and suggestions for further applications and research.

CHAPTER II

Numerical Formulation of the Scattering Model

2.1 Introduction

From the point of view of classical theory, any precise treatment of electromagnetic scattering and diffraction phenomena generally involves the complete solution of a boundary value problem. However, there are only few cases in which this rigorous approach is productive. As a result the optimum approach in our case is to find an approximate solution to the original problem.

Due to the high speed and large storage capacity of digital computers in recent years, considerable interest has been shown in the use of numerical solution techniques to the evaluation of scattering and radiation problems [23], and [24]. The scattering properties of complex bodies can be computed with very high accuracy through the application of numerical techniques. However, the difference equation formulation is not efficient for this purpose. Of the many approaches available and, considering the adaptability of the formulation for computer use, the integral equation representation has proven to be an efficient form for the numerical solution [25].

It is the purpose of this chapter to review how simple vector boundary value problems associated with electromagnetic scattering phenomena can be reduced to sets of integral equations suitable for numerical solutions and how the procedure can be applied to the problem of a two dimensional scatterer modelling the surface of the antenna under investigation.

2.2 The Surface Integral Equation of the Scatterer.

When an electromagnetic wave with $e^{(j\omega t)}$ time variation is normally incident on a scattering cylindrical body with constant cross section s along the z direction Fig.-2.1, both the total electric and magnetic fields are functions of the transverse coordinates only. For this case, the magnetic field integral equation (MFIE) [23] becomes completely independent of the electric field. After some manipulation it takes the form

$$\mathbf{H}(\rho) = T\ \mathbf{H}^{inc}(\rho) + T\ \frac{jk}{4} \int_c [\mathbf{H}(\rho')\, H_1^2(k|\rho - \rho'|) \cos(\hat{n}', \rho - \rho') + (\frac{\partial \mathbf{H}}{\partial n'} - \hat{n}' \nabla'_t \,.\, H_t)\, H_0^2(k|\rho - \rho'|)]dc \qquad (2.2.1)$$

where ρ and ρ' represent the position vectors of the field and source points P and Q in the transverse plane, respectively, and $\hat{n}$ is the unit outward normal to the scatterer. In general, primes will be used to indicate vector operations in source coordinates. Also a prime will be used to indicate a normal defined at the source point Q . $\mathbf{H}^{inc}$ is the incident magnetic field while H_0^2 and H_1^2 are the Hankel functions of the second kind of order zero and unity, respectively. The t subscript refers to the transverse plane and c is the linear integration contour around the cross section s of the scatterer. k is the usual wave number while H_t and H_z denote the functional forms of the magnetic field in the transverse plane and the axial direction z , respectively.

T is a constant with value of 1 for ρ outside the surface s , and assumes the value of 2 for ρ on a smooth portion of the surface. Also $\cos(\hat{n}', \rho - \rho')$ is the cosine of the angle between the normal $\hat{n}$ and the vector connecting the observation and the source points P and Q in the transverse plane.

In our problem, the excitation is due to a magnetic line source in the z direction (*i.e.* the *TE* case), and therefore we have only one component of $\mathbf{H}$, namely H_z . Accordingly $\nabla'_t H_t$ vanishes and $\frac{\partial \mathbf{H}}{\partial n'}$ equals $\frac{\partial H_z}{\partial n'} \hat{a}_z$ where $\hat{a}_z$ is a unit vector in the direction of increasing z. Substituting for $\frac{\partial H_z}{\partial n'}$ we find that the term

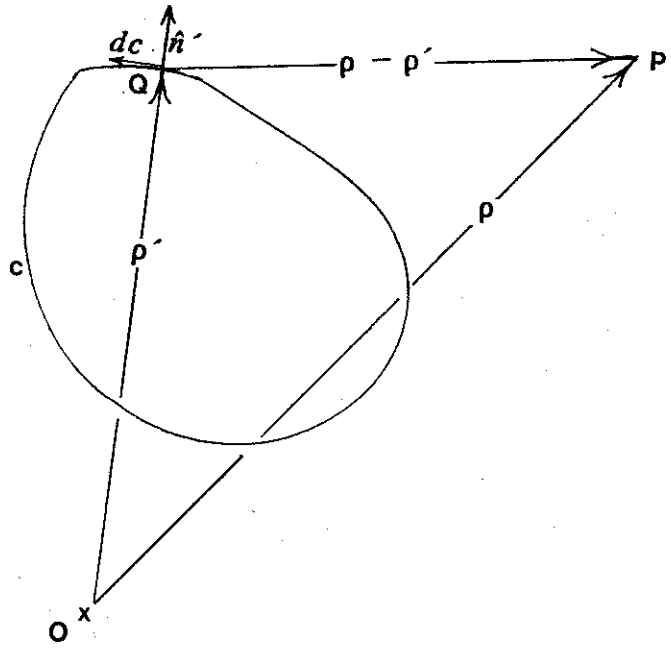

Fig.-2.1 Cross section of the scattering cylinder.

$-j\omega\epsilon E_\phi$ vanishes on the conductor, and for $J_c = H_z$ using the relation $\mathbf{J} = \hat{n} \times \mathbf{H}$ on the conductor surface in equation (2.2.1) gives

$$H_z^{inc}(\rho) = \frac{1}{2} J_c(\rho) - \frac{jk}{4} \int_c J_c(\rho') H_1^2(k|\rho - \rho'|) \cos(\hat{n}', \rho - \rho') dc' \qquad (2.2.2)$$

Equation (2.2.2) is a Fredholm integral equation of the second kind for the ϕ directed surface current J_c on a cylinder illuminated by a TE polarized line source.

2.3 Numerical Solution of the Integral Equation

In the last section, the problem of two dimensional scattering was formulated in the form of an integral equation (2.2.2). This equation however is of little use unless it can be evaluated analytically or can be computed numerically with the aid of a digital computer. The choice between these two different approaches largely depends on the characteristic dimension of the scatterer.

For scatterers of arbitrary shape, whose dimensions are either very small or very large with respect to the wavelength, Rayleigh scattering theory and the physical optics approximation will yield fairly accurate results. In the intermediate range, the numerical procedure known as the method of moments [24] has proven to be the most efficient approximate method for obtaining results of acceptable accuracy. The results of the application of this approach to scattering problems is essentially a transformation of the original integral equation into a set of N linear equations in N unknowns. A linear combination of the N unknowns forms an approximation to the original unknown quantity appearing in the associated integral equation. The above procedure may be written in a matrix equation of the form

$$[\mathbf{A}]\,[\mathbf{f}] = [\mathbf{g}] \qquad (2.3.1)$$

Where [A] is the coefficient matrix, [f] is the unknown quantity, and [g] is the known quantity of the matrix equation. The matrix equation (2.3.1) may be solved numerically. However, in methods using factorization or inversion, the required computer time for solving (2.3.1) is given approximately by [25]

$$T = aN^2 + bN^3 \tag{2.3.2}$$

where a and b are proportionality factors, N is the number of unknowns (matching points), aN^2 and bN^3 account for the calculation of the coefficient matrix and the solution of (2.3.1), respectively.

The accuracy of the solution largely depends on the number of sampling points N and the approximate methods used for evaluation of the elements of the matrix [A] [24], since the determination of [A] requires approximate evaluation of the sub integrals over N, a better accuracy would require more accurate approximation techniques. This in turn results in a higher value for the proportionality factor a appearing in (2.3.2) [25]. In view of the relation (2.3.2), it seems advantageous to keep N as low as possible and use more accurate techniques for evaluating [A], which in fact, within certain limits, yields the same accuracy with less computation time. However, there is a limit on N, beyond which the accuracy of the solution would greatly be impaired. Andreasen [26] has shown that for a smooth portion of the scatterer, the distance between two adjacent sampling points must not exceed $\lambda/4$. Furthermore, for regions close to the sharp edges, additional sampling points must be introduced.

2.4 Formulation by the Method of Moments

In section 2.2 it was shown that a solution of the electromagnetic fields in the presence of an infinitely long conducting cylinder of an arbitrary cross section illuminated by a magnetic line source parallel to the axis of the cylinder can be obtained from the relation

$$H_z^{inc}(\rho) = \frac{1}{2} J_c(\rho) - \frac{jk}{4} \int_c J_c(\rho') H_1^2(k|\rho - \rho'|) \cos(\hat{n}', \rho - \rho') \, dc' \tag{2.4.1}$$

Now, the unknown quantity in the integral equation is J_c and equation (2.4.1) can be solved by the standard moment method procedure.

For illustration purposes, the above formulation is applied to an E-plane horn structure whose axis lies on the x-axis and is excited by a magnetic line source

parallel to the aperture edges and located on the axis of symmetry. The contour of integration c, however, will be as shown in Fig.-2.2, which also shows the procedure for numbering the segments in a clockwise direction in preparation for a moment method solution. The total number of subdivisions is $2S_1$. When pulse functions are used in the expansion of the unknown surface currents, and point matching procedure is applied for testing [24], the appropriate matrix equation for the present case will be in the form

$$[A_{mn}]\,[F_n] = [G_m] \tag{2.4.2}$$

where G is a vector of length $2S_1$ representing the field incident from the magnetic line source of unit intensity and zero phase. Assuming that the line source is located at a distance ρ_s from the origin of coordinates, then the m^{th} element of $[G_m]$ will be given by

$$G_m = -\frac{k}{4\eta} H_0^2(k|\rho_m - \rho_s|) \tag{2.4.3}$$

where ρ_m is the radial coordinate of the center of segment m, and η the characteristic impedance of free space. $[F_n]$ is the vector representing the unknown current coefficients, and $[A_{mn}]$ is a $(2S_1)\times(2S_1)$ coefficient matrix with elements given by [24]

$$A_{mn} = \begin{cases} \dfrac{1}{2} & m = n \\ \dfrac{jk}{4} H_1^2(k|\rho_m - \rho_n|)\cos\nu_{mn}(\Delta\, c\,)_n & otherwise \end{cases} \tag{2.4.4}$$

where

$$\cos\nu_{mn} = \cos\,(\,\hat{n}',|\rho_m - \rho_n|) \tag{2.4.5}$$

Also $(\Delta\, c\,)_n$ is the length of the n^{th} segment while subscripts m and n refer to the observation and source points, respectively.

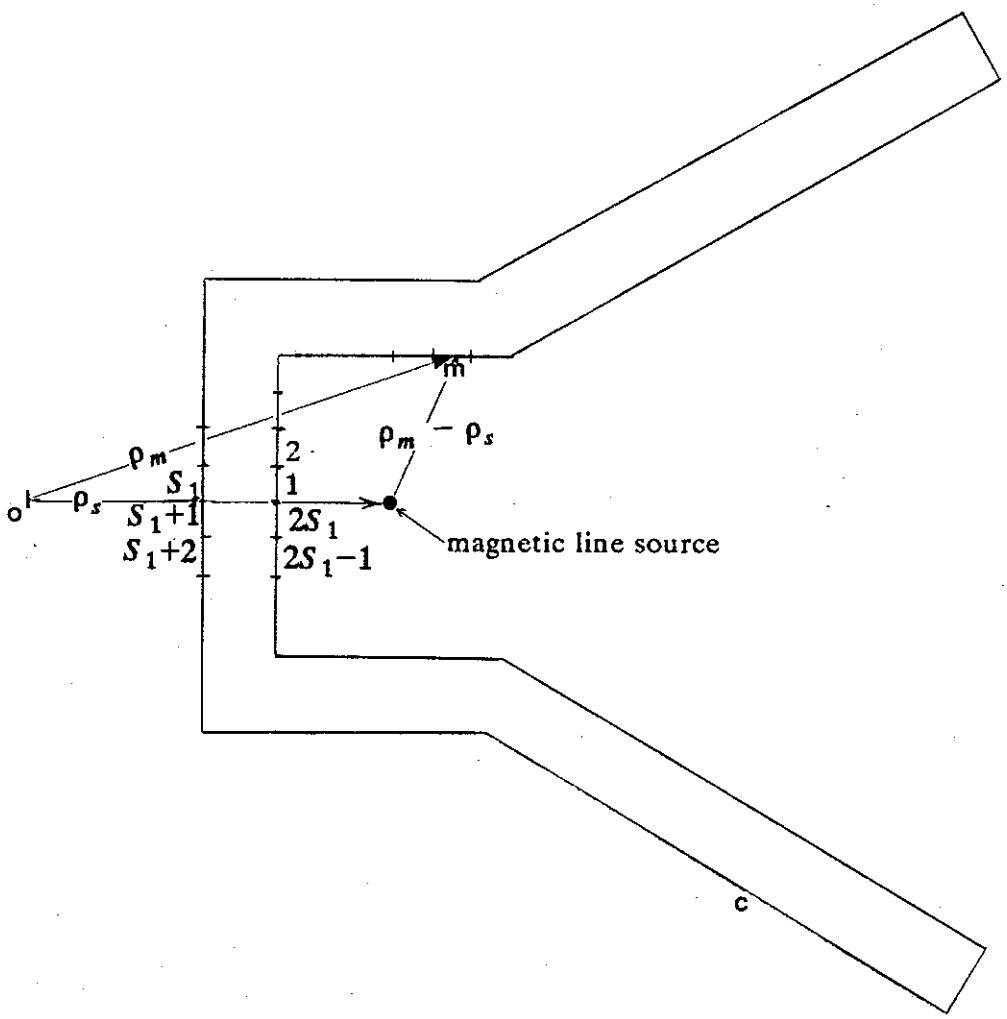

Fig.-2.2 Scattering structure of an E-plane sectoral horn.

Equation (2.4.2) as it stands, might need more computer storage and Central Processing Unit (CPU) time for inversion than is necessary. One can make use of the symmetry properties of the geometry and the excitation to reduce the computer requirements for core storage capacity and execution time. Hence from Fig.-2.2 it is clear that two points on contour c of the horn, symmetrically located with respect to the x −axis, will have exactly the same value for both the incident field and the surface current. Using the segment numbering shown in Fig.-2.2, it might be easily deduced that

$$G_i = G_{(2S_1 + 1 - i)} \tag{2.4.6}$$

and

$$F_i = F_{(2S_1 + 1 - i)} \tag{2.4.7}$$

Using (2.4.6) and (2.4.7) in (2.4.2), one obtains a new matrix equation, namely

$$[A'_{mn}]\,[F'_n] = [G'_m] \tag{2.4.8}$$

where $[F'_n]$ and $[G'_m]$ are now vectors with S_1 elements each, and $[A'_{mn}]$ is an $S_1 \times S_1$ square matrix. Solution for $[F'_n]$ gives the surface current on one side of the horn. The matrix elements will now be given by

$$F'_m = F_m \quad ; \quad G'_m = G_m \qquad m = 1,2,\ldots,S_1 \tag{2.4.9}$$

and

$$A'_{mn} = A_{mn} + A_{m(2s_1+1-n)} \qquad m = n = 1,2,3,\ldots,S_1 \tag{2.4.10}$$

The new coefficient matrix $[A'_{mn}]$ now is stored in a space which is only one quarter of that needed for the original matrix $[A_{mn}]$ of (2.4.2). In addition, since the number of columns and rows has been reduced to half each, the total inversion time is reduced to one eighth of its original value [24].

Since the scattered field $\mathbf{H}^{sc}$ at point ρ is related to the incident field $\mathbf{H}^{inc}$ and the total field $\mathbf{H}$ at the same point through

$$\mathbf{H}^{sc}(\rho) = \mathbf{H}(\rho) - \mathbf{H}^{inc}(\rho) \tag{2.4.11}$$

it is easily realized that the formula needed to compute the scattered field is given by the right-hand-side of (2.2.1), after omitting the term with $\mathbf{H}^{inc}$ and making the substitution $T = 1$. Considering the same argument discussed above in deducing equation (2.2.2) from (2.2.1), one obtains the following expression for the scattered magnetic field at the point (ρ,ϕ) in the transverse plane

$$H_z^{sc}(\rho,\phi) = \frac{jk}{4}\int_c J_c(\rho')\cos\nu\, H_1^2(k|\rho-\rho'|)dc' \tag{2.4.12}$$

where the parameters are defined as before.

In evaluating the scattered field at far distances using (2.4.12) we let ρ tend to infinity and substitute for the Hankel function by its asymptotic form, namely [27]

$$\lim_{\rho\to\infty} H_1^2(k|\rho-\rho'|) = \sqrt{\frac{2j}{\pi k\rho}}\; j e^{-jk\rho}\, e^{jk\rho'\cos(\phi-\phi')} \tag{2.4.13}$$

then using the solution for the current $J_c(\rho')$ as obtained from the solution of (2.4.8) at the discrete points ρ_n' one finally obtains for the scattered field

$$H_z^{sc}(\rho,\phi) = \sqrt{\frac{jk}{8\pi\rho}}\, e^{-jk\rho} \sum_{n=1}^{n=s_1} (J_c)_n \frac{(\rho_n-\rho)}{|\rho_n-\rho|}\cdot\hat{n}\; e^{jk\rho_n\cos(\phi_n-\phi)}\,(\Delta c)_n \tag{2.4.14}$$

The total radiated field at a point (ρ,ϕ) is obtained as the sum of the incident field plus the scattered field. Hence, we have

$$\mathbf{H}^{tot}(\rho,\phi) = \frac{-k}{4\eta} H_0^2(k|\rho-\rho_s|) + \mathbf{H}^{sc}(\rho,\phi) \tag{2.4.15}$$

where ρ_s is the position vector of the excitation line source.

Equation (2.4.8) was programmed on a digital computer and solved using the IMSL [28] program library, for different horn and reflector designs. The

corresponding radiation field patterns were then evaluated using (2.4.15). For structures that have no geometrical symmetry, equations (2.4.2) and (2.4.15) are used for evaluation of their field patterns.

CHAPTER III

Aperture-Matched Horns and Waveguides

3.1 Introduction

In many problems involving far field patterns of horn antennas, analytic solutions are possible for few geometries and can only be generated easily for ordinary conventional horns whose apertures are modified by simple geometries. For geometries involving horns with arbitrary shaped edges such as ellipses and spirals, numerical solutions must be utilized. The first part of this chapter presents the far field patterns of plane-flange aperture matching of horns. The second part deals with convex shaped cylinder aperture matching, and presents field patterns of elliptic and spiral matched horn apertures. For comparison purposes, the unmatched horn is the optimum gain horn defined by Schelkunoff [29].

It should be pointed out that the moment method does not allow infinitely long horn walls or feed waveguides. The latter are selected at 2λ length with line source along the axis at 0.6λ from the shorted end of the waveguide which proved adequate for exciting the TE_{01} mode in a semi infinite waveguide. It should also be pointed out that since the peak of the radiation pattern is always normalized to 0dB, an increase or decrease in the sidelobe level means a corresponding increase or decrease in the radiation pattern envelope (RPE) as done in antenna analysis. Radiation pattern envelope is a curve that describes the trend of the sidelobe peak levels in the radiation pattern plot of an antenna.

3.2 Aperture-Matched Horns

The numerical simulation of the optimum gain horn, which is referred to all throughout as the "conventional" horn, starts with a polygonal cylinder excited by a magnetic line source. Because the formulation of the scattering problem discussed in Chapter II followed an MFIE approach, a closed surface must be used in the simulation. Hence, a finite thickness is introduced for all the metallic walls of the horn. In this case, current magnitudes in the inside and outside walls of the horn are evaluated more accurately. The excitation of the horn is achieved by placing a magnetic line source in an appropriate position inside the feed waveguide of the horn as shown in Fig.-3.1. A sufficient length of the feed waveguide is used to ensure the propagation of a TE_{01} mode in the throat area of the horn [30]. A schematic diagram of the simulated horn with its dimensions is shown in Fig.-3.2. The corresponding field patterns of this horn for different wall thicknesses are calculated and compared with results based on the aperture integration method for an identical horn using equation (3.2.1) [31], *i.e.*

$$E_{\phi} = I\ (1+\cos\phi)\ F(t'_1, t'_2) \tag{3.2.1}$$

where,

$$t'_1 = \sqrt{\frac{k}{\pi\rho_1}}\left(-\frac{b_1}{2} - \rho_1\sin\phi\right) \tag{3.2.2}$$

$$t'_2 = \sqrt{\frac{k}{\pi\rho_1}}\left(+\frac{b_1}{2} - \rho_1\sin\phi\right) \tag{3.2.3}$$

$$F(t'_1, t'_2) = [C(t'_2) - C(t'_1)] - j[S(t'_2) - S(t'_1)] \tag{3.2.4}$$

where b_1, and ρ_1 are dimensions of the E-plane sectoral horn as shown in Fig.-3.3, $C(x)$ and $S(x)$ are known as the cosine and the sine Fresnel integrals, while I is a normalizing factor. The results are shown in Fig.-3.4. These results show that for a wall thickness of 0.1λ the corresponding field pattern is almost identical to that computed using aperture integration method except in the region of $\phi = 90^o$ to 180^o, this

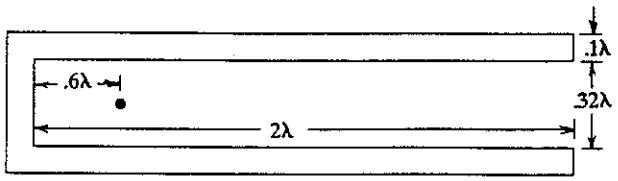

Fig.-3.1 Geometry used in the simulation of the feed waveguide with the magnetic line source placed at 0.6λ from the closed end of the structure.

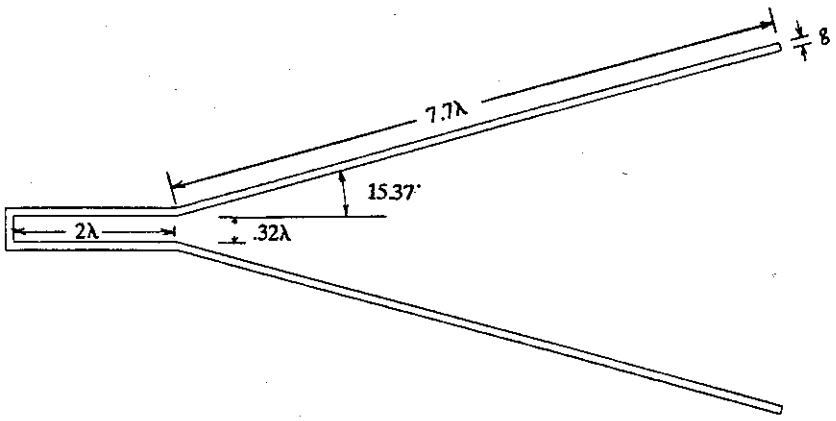

Fig.-3.2 Schematic diagram of the simulated conventional horn having a wall length of 7.7λ, semi flare angle of 15.37^0, and wall thickness g.

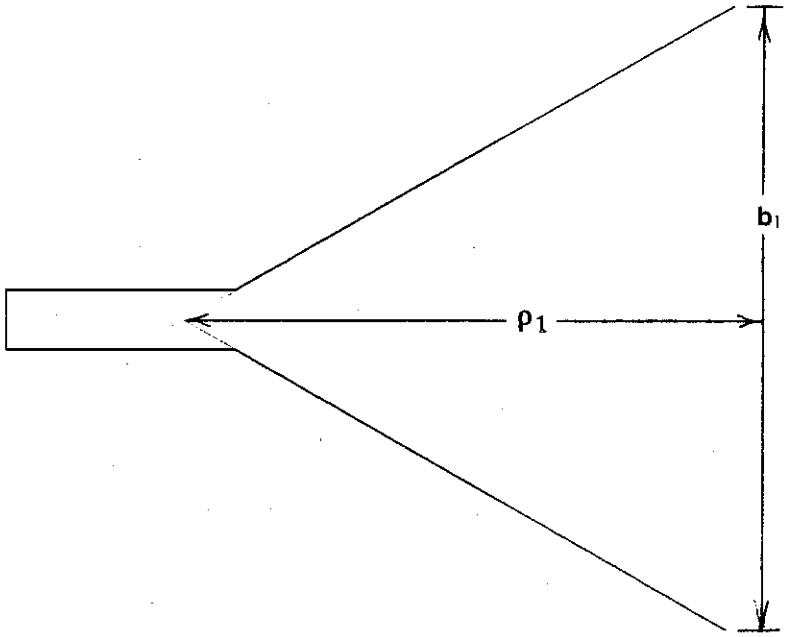

Fig.-3.3 *E* -plane sectoral horn.

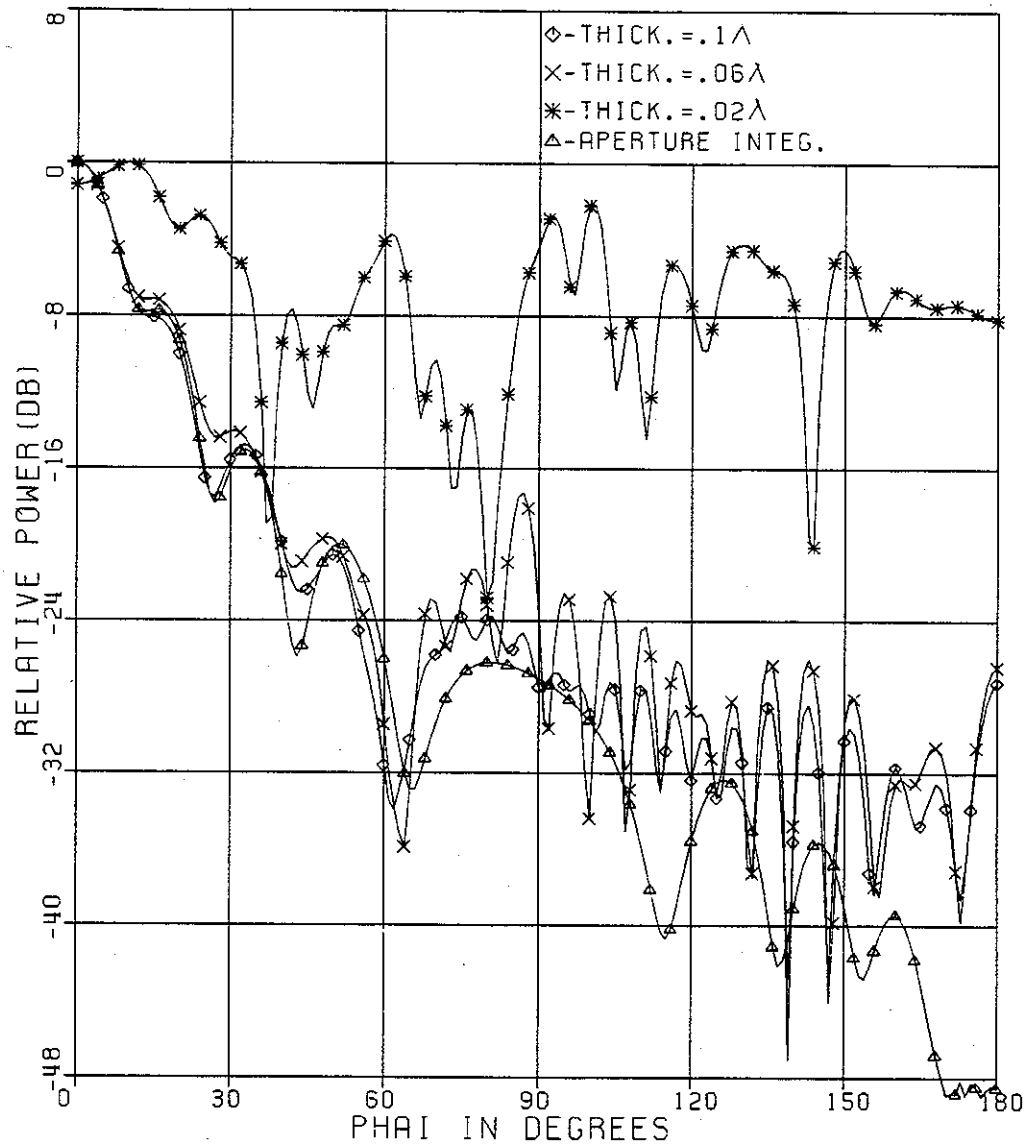

Fig.-3.4 *E*-plane radiation patterns of sectoral horns with different wall thicknesses.

is due to the fact that the edge diffracted fields at the horn edges are not included in the derivation of equation (3.2.1), while the numerical formulation of Chapter II takes such fields into account. As a result, the thickness of 0.1λ is chosen throughout all computations. In the following sections aperture matching of horns is done by attaching flat and convex shaped flanges at the aperture edges of the conventional horn.

3.2.1 Plane Aperture-Matched Horns

In this section the far field pattern of plane aperture-matched horns are calculated. This type of matching involves a flat plane section attached to the aperture edges of an optimum gain horn. This plane flange can have an arbitrary electrical length d and is mounted at an arbitrary angle with respect to the flared walls of the horn.

One type of plane matched horns is shown in Fig.-3.5. This type, which is designated as Case *I*, has a plane flange of length d perpendicular to the axis of the horn. A comparison of Case *I* matched horn for $d=2\lambda$ and the conventional horn field patterns is shown in Fig.-3.6 which shows a reduction in the sidelobe levels in the $\phi=90^o$ to 180^o region achieved by the matched horn. Fig.-3.7 shows the response of the field patterns due to an increase in the electrical length of the plane flanges for Case *I* matched horn. In Fig.-3.8 the patterns of Case *I* horn are computed at different operating frequencies and the plots show a significant frequency dependence for such type of aperture matching.

Another type of plane matched horns designated by Case *II* is shown in Fig.-3.9. The plane flange in this case makes an angle α with the flared walls of the horn. An angle $\alpha=0^o$ corresponds to having the flared walls increased by d. An angle $\alpha=90^o$ corresponds to a plane flange perpendicular to the flared walls of the horn. Fig.-3.10 shows the field patterns for Case *II* matched horn for different values of flange flare angle α and for $d=2\lambda$. It is noticed that for $\alpha=90^o$, where the edges are sharpest relative to the other cases of $\alpha=0^o$ and $\alpha=45^o$, high sidelobe levels are

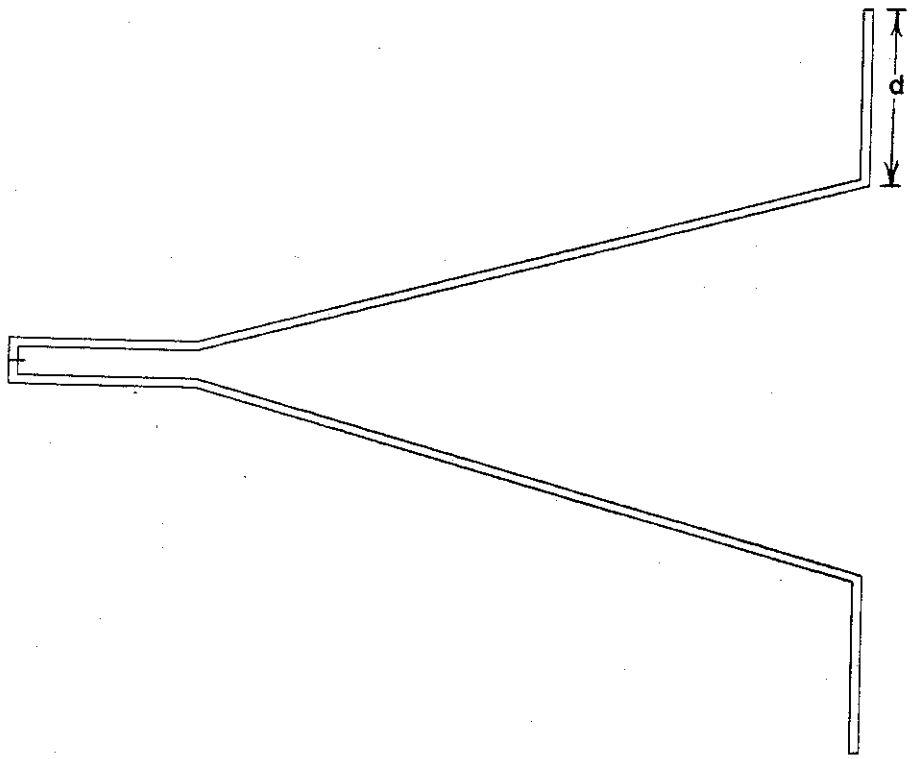

Fig.-3.5 Flat plane aperture-matched horn case I of flange length d.

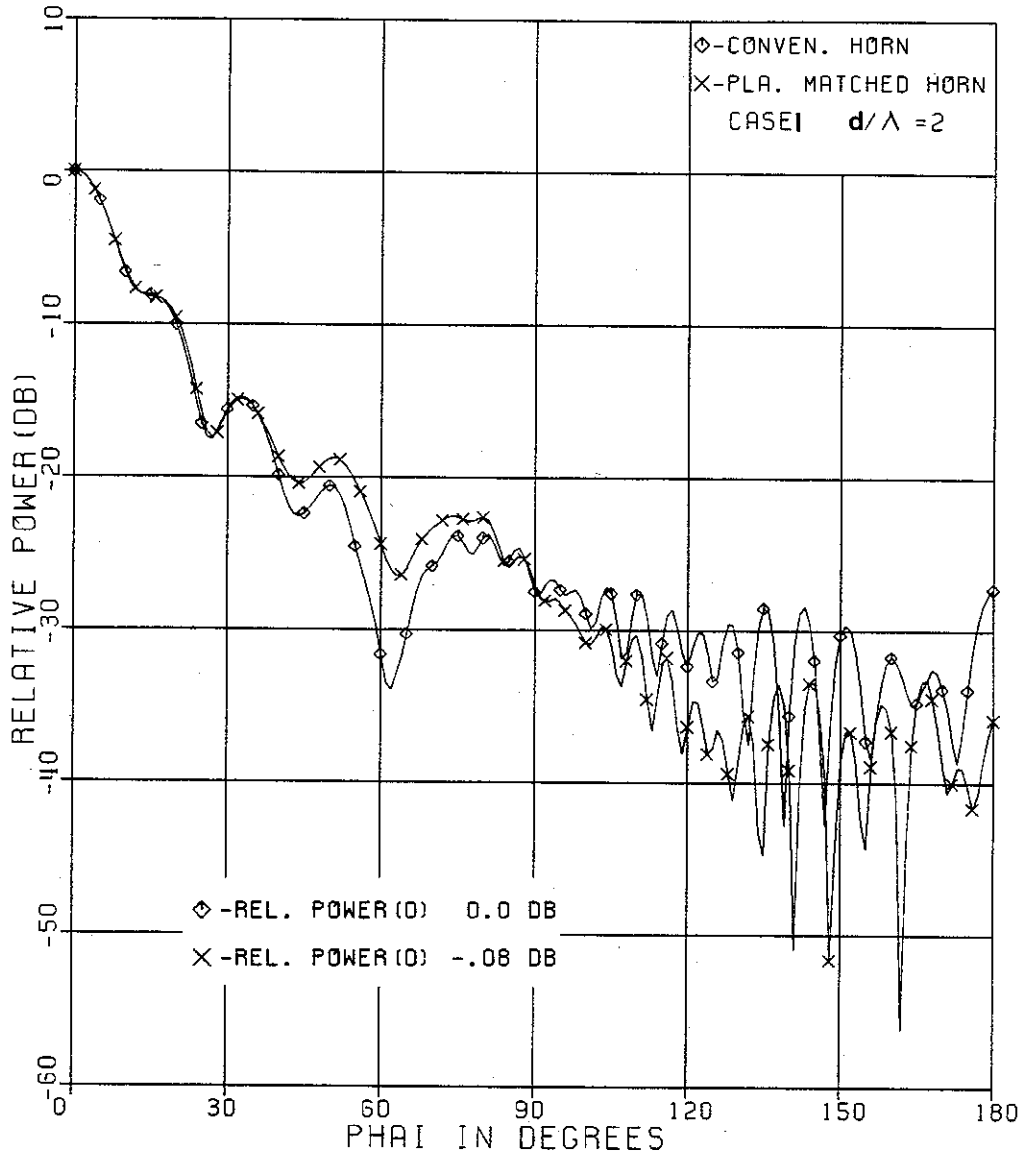

Fig.-3.6 **E-plane radiation pattern of conventional and flat plane matched(case I) sectoral horns.**

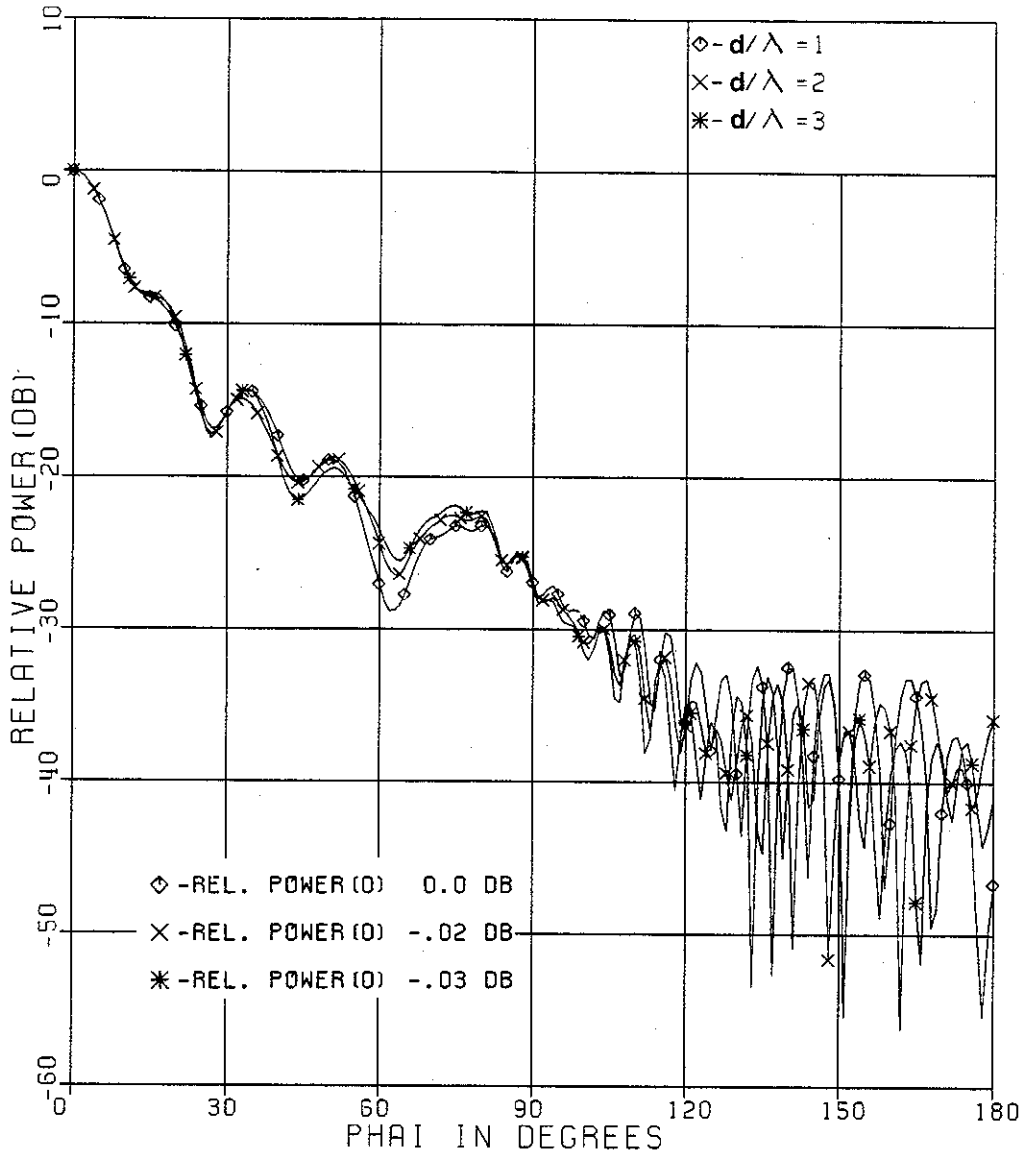

Fig.-3.7 **E-plane radiation patterns of flat plane matched horns case I for different flange length d.**

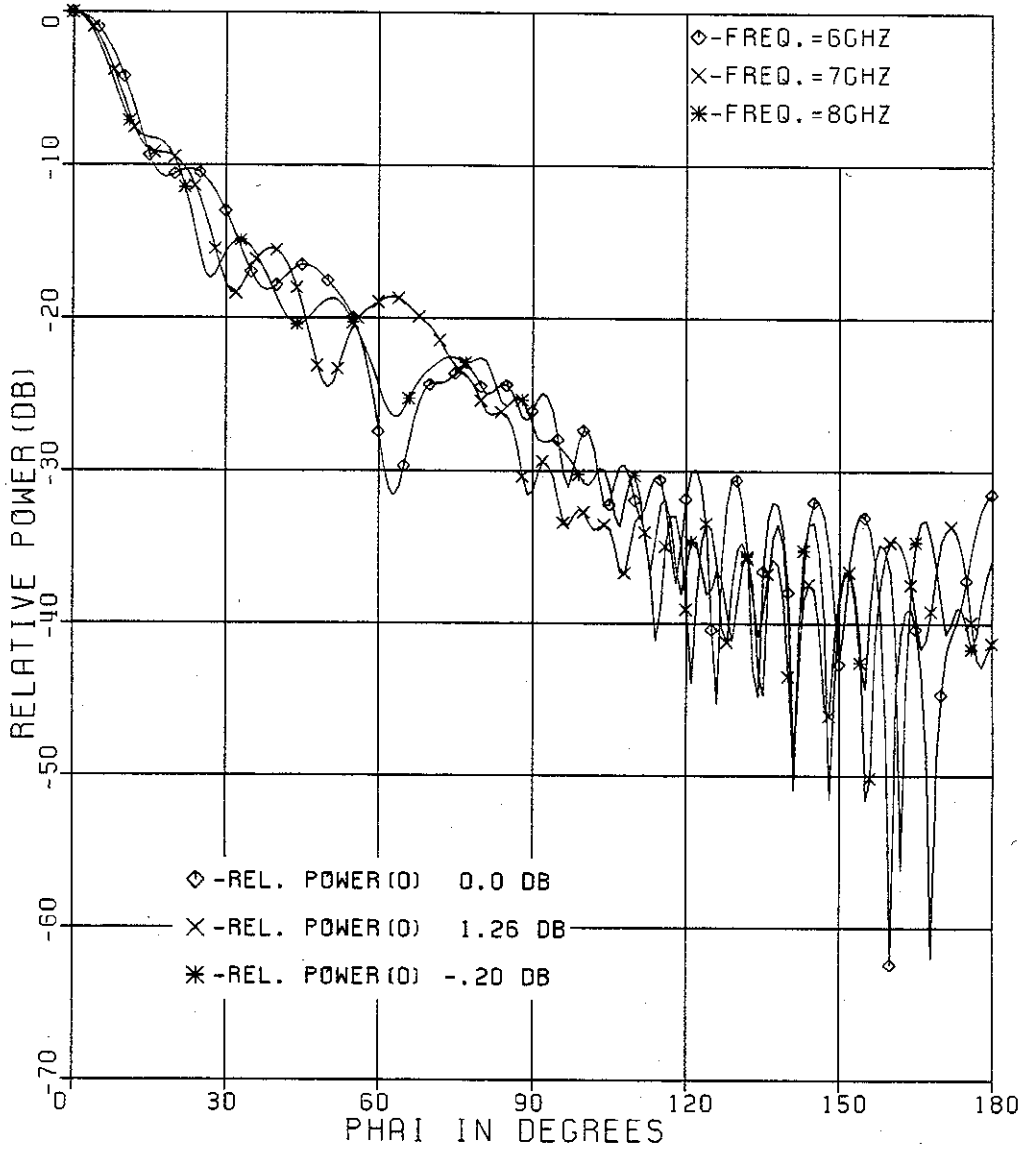

Fig.-3.8 **E-plane radiation patterns of flat plane matched horns case I at different frequencies, d=2λ at F=8 GHZ.**

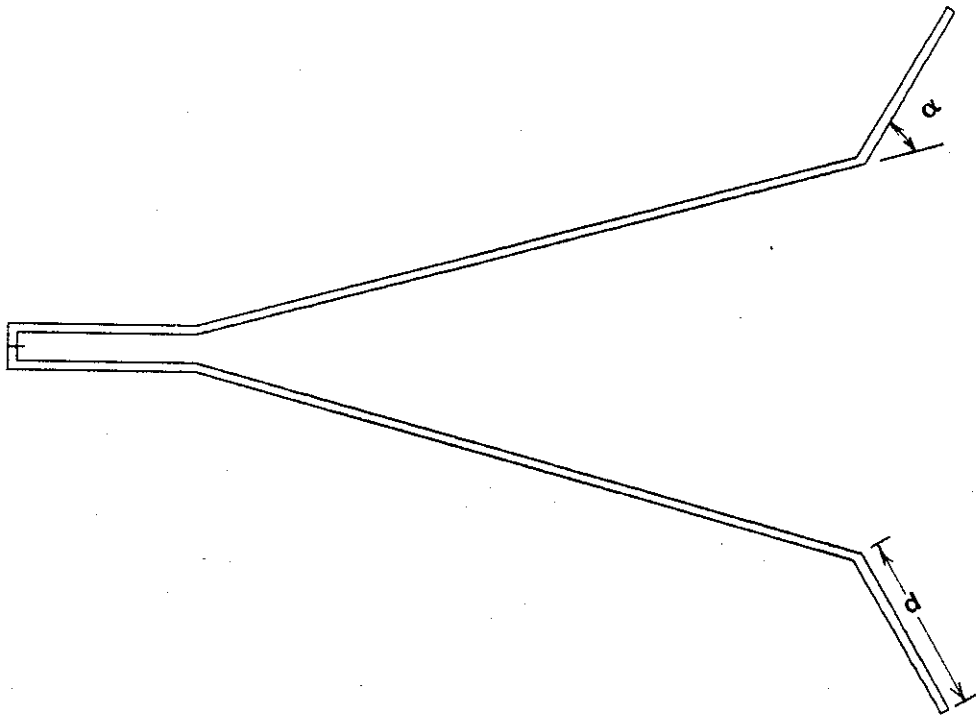

Fig.-3.9 Flat plane aperture-matched horn case II with the matching flange having a length d and making an angle α with the flared wall of the horn.

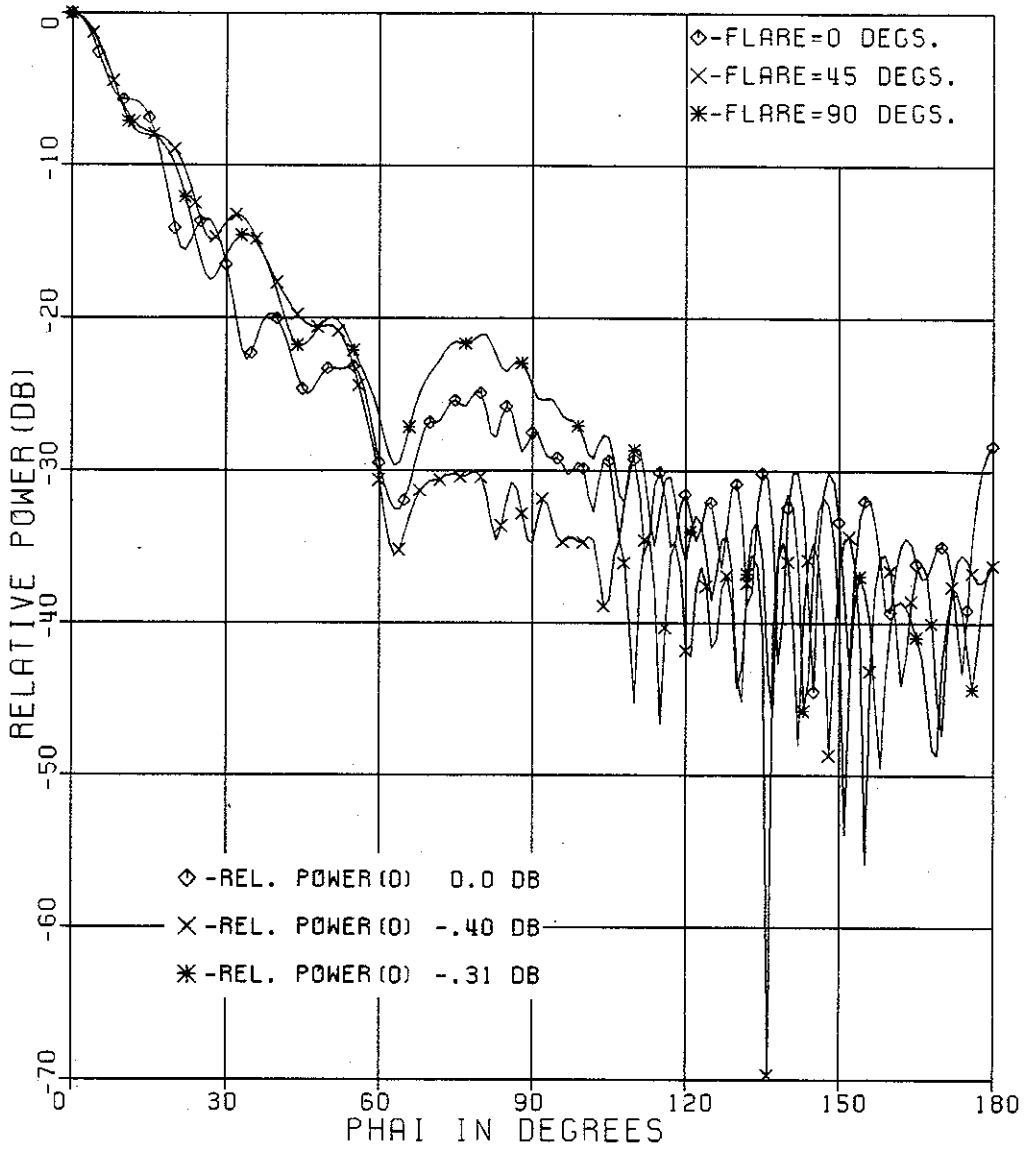

Fig.-3.10 **E-plane radiation patterns of flat plane matched horns case II for different flange flare angle α.**

observed in the $\phi=60^o$ to 120^o region.

3.2.2 Ellipse Aperture-Matched Horns

Another type of aperture matching investigated here is designated as the ellipse-matched horn and is shown schematically in Fig.-3.11, where an ellipse is tangential to each wall at the edge and the major axis of each ellipse is parallel to the adjacent wall. In this type, a section of an elliptic cylinder with semimajor axis A and semiminor axis B is added to our conventional E-plane horn. It should be noted that the segments used to simulate the horn boundary in the numerical solution are the same segments used to draw the shapes of the simulated horns shown in the figures except for a scaling factor. This applies to all structures simulated in this thesis including the horn with elliptical flanges shown in Fig.-3.11. Fig.-3.12 shows a comparison between the computed patterns of an ellipse-matched horn using 3/4 of the cylinder surface for $A=3\lambda$ and $B=1.5\lambda$ and that of a conventional horn. A significant decrease in the sidelobe level over a wide angle range is achieved by the elliptical flange matching of the horn aperture. A broader beam width of the matched horn is also observed and this can be attributed to the tapering of the field in the aperture. In Fig.-3.13 the radiation pattern of the field in the elliptic matched horn of Fig.-3.11 for $A=3\lambda$ and $B=1.5\lambda$, is computed for different lengths of the elliptic cylinder. These patterns show that matching with one quarter of the elliptic cylinder is enough to cause a significant decrease in the level of the near side lobes. A comparison of the far field horn patterns with elliptic and circular cylinder aperture matching are shown in Fig.-3.14.

In order to investigate the frequency dependence of such type of aperture matching, the patterns at different operating frequencies are computed and shown in Fig.-3.15. Smaller dependence on frequency is observed for such aperture matching as compared with plane flange aperture matching already presented in section 3.2.1. An investigation for different electrical sizes of the elliptical cylinders shows that the field patterns in Fig.-3.16 have lower side lobe levels with increasing value of A/λ with $B/A = 0.5$.

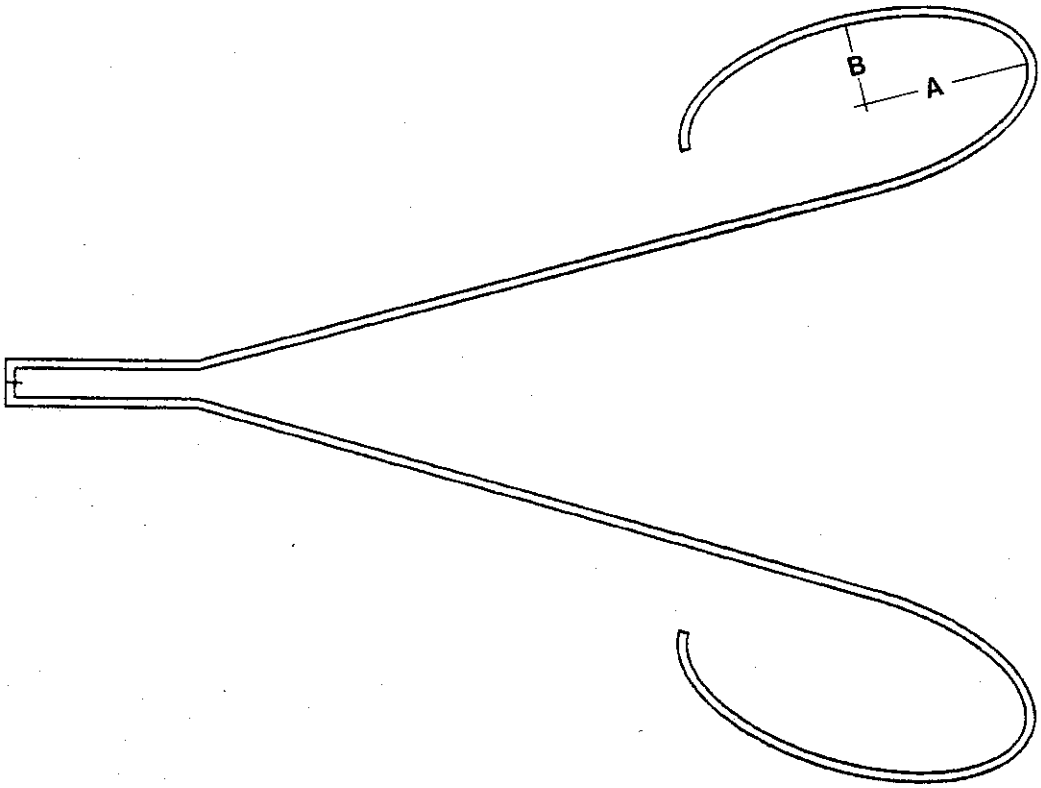

Fig.-3.11 Ellipse aperture-matched horn with the ellipse flange having a semi major axis A , and a semi minor axis B .

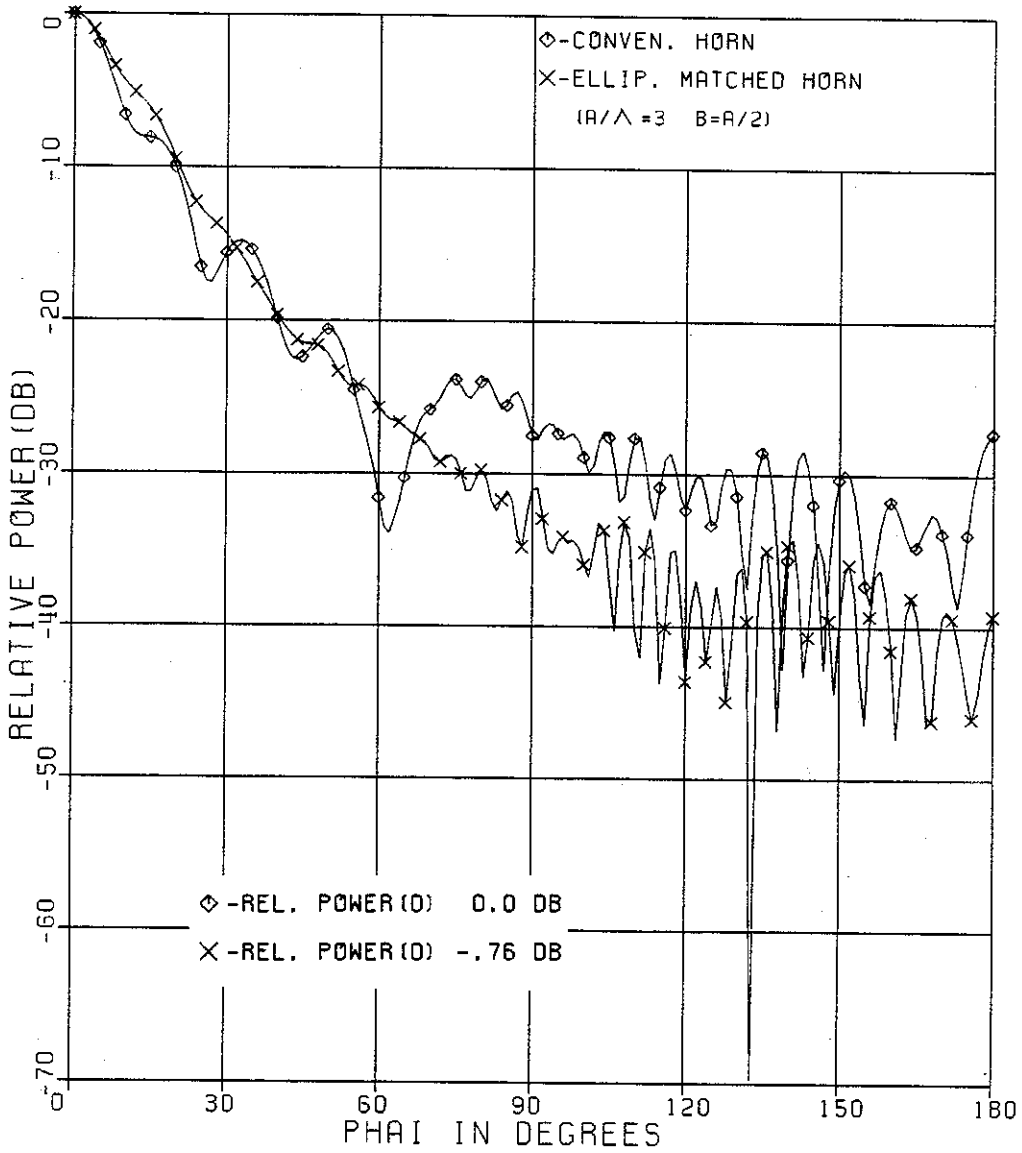

Fig.-3.12 *E*-plane radiation patterns of conventional and ellipse-matched sectoral horns.

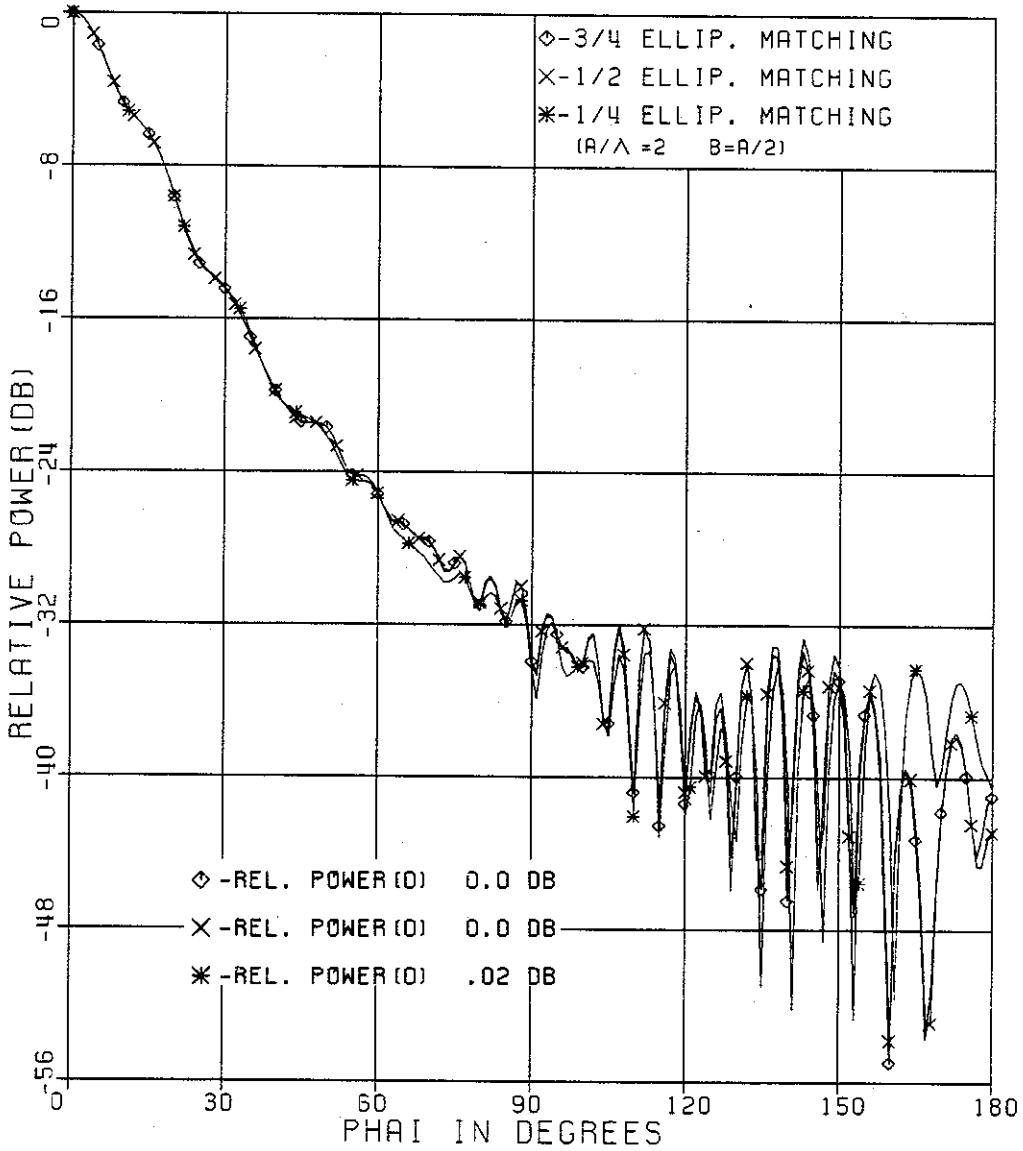

Fig.-3.13 *E*-plane radiation patterns of ellipse matched horns for differnt lengths of the ellipse flange.

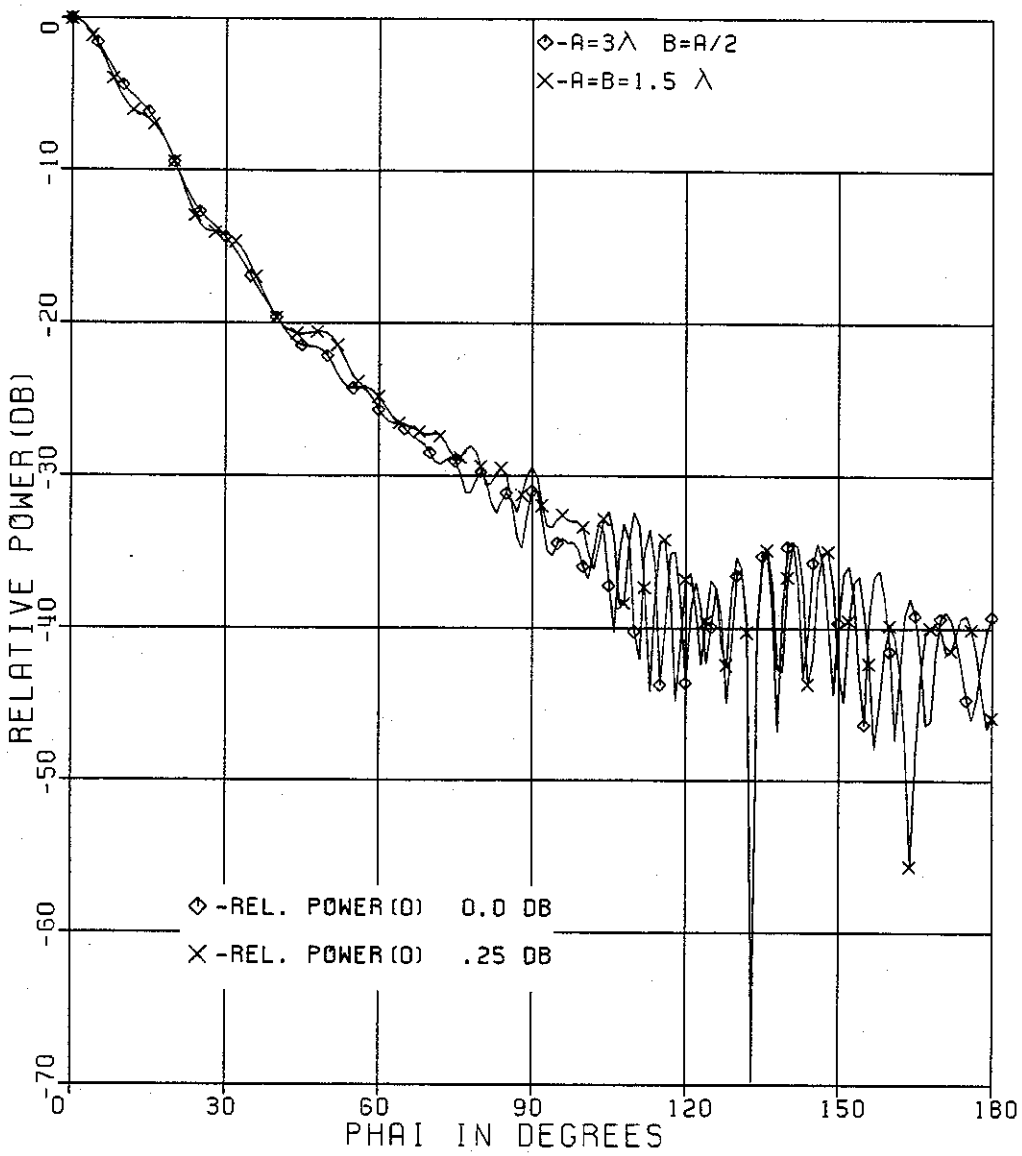

Fig.-3.14 *E*-plane radiation patterns of ellipse and circle matched sectoral horns.

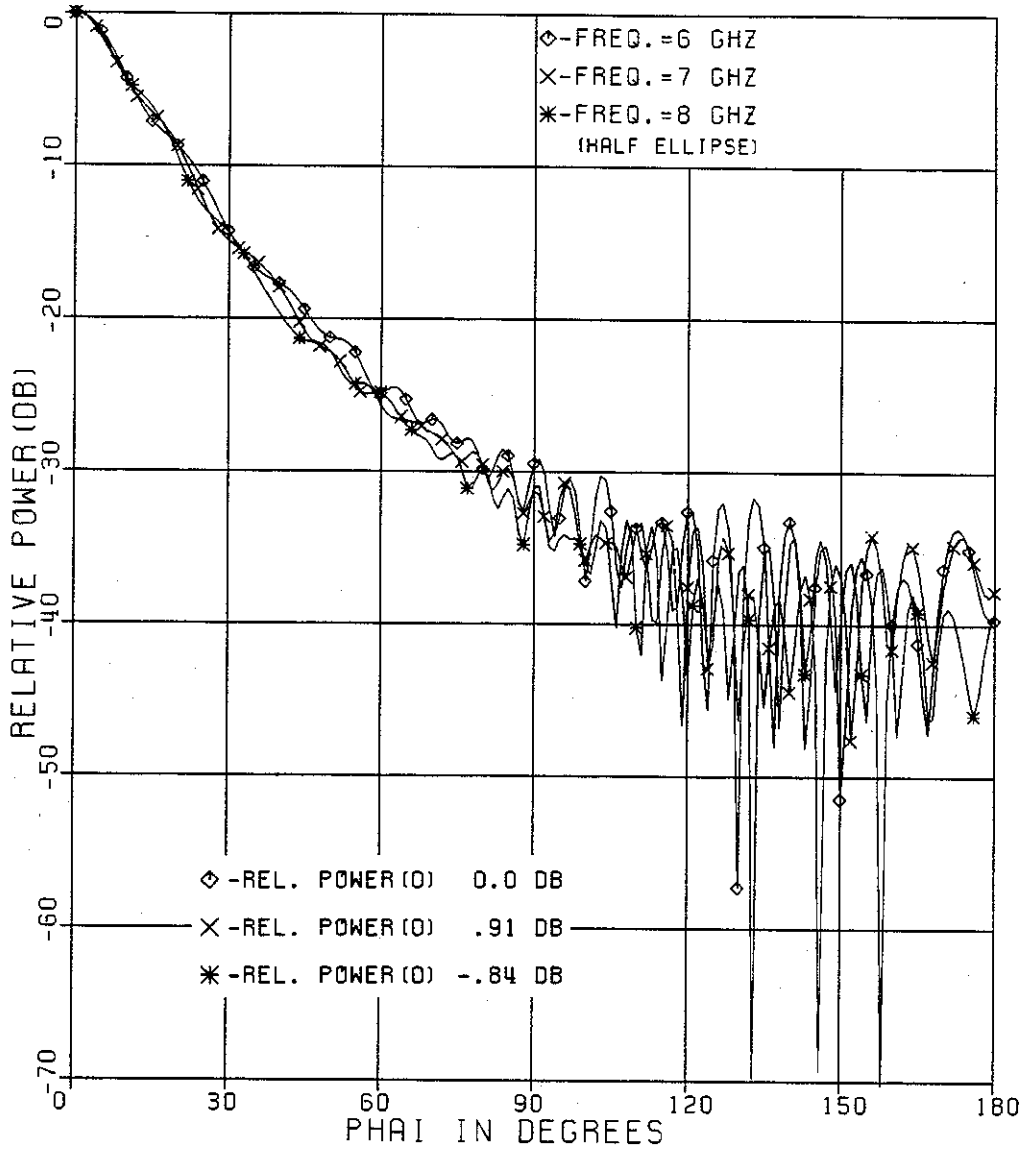

Fig.-3.15 *E* -plane radiation patterns of ellipse matched horns at different frequencies with $A = 3\lambda$, $B = A/2$ at F=8 GHZ.

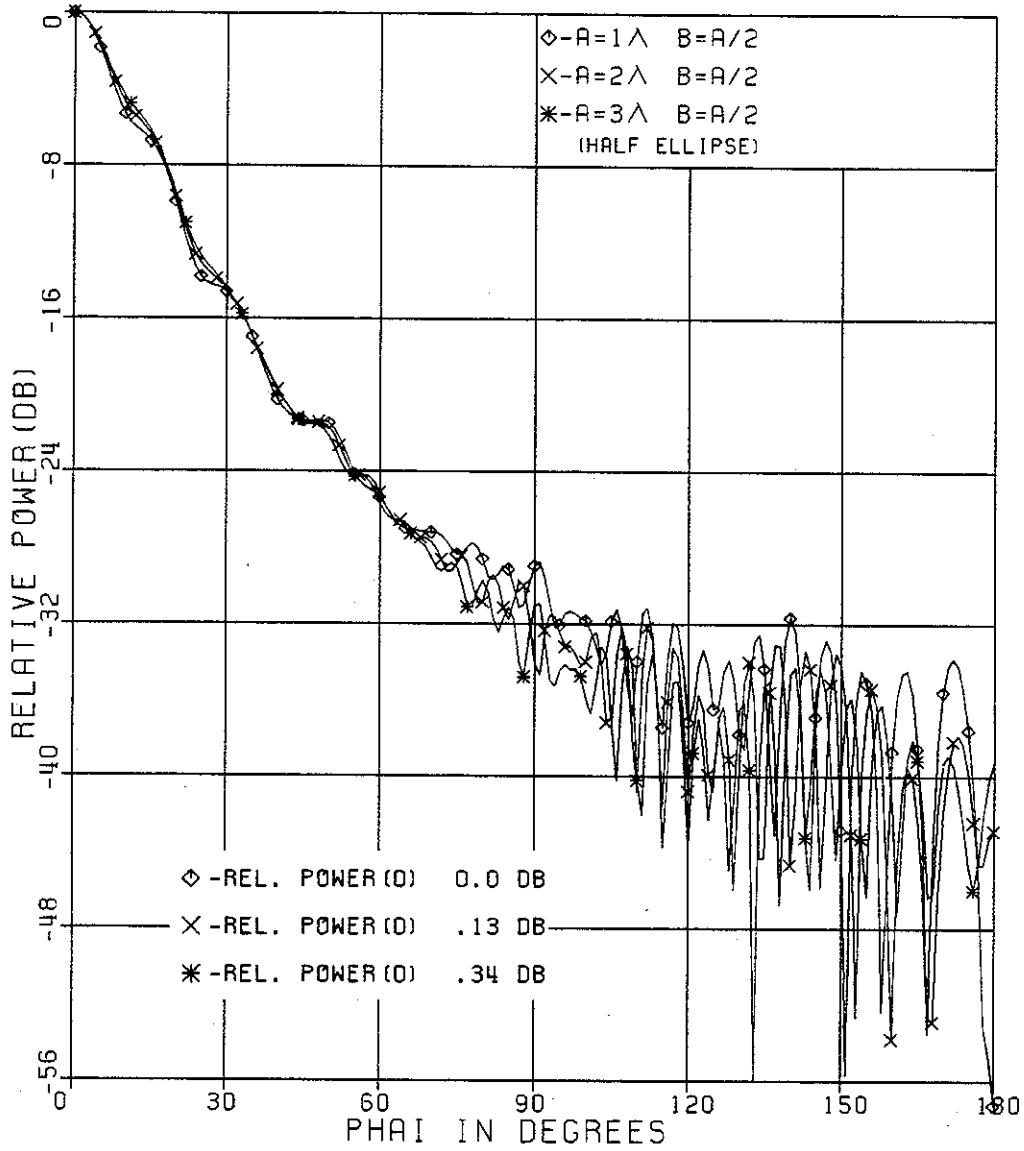

Fig.-3.16 *E*-plane radiation patterns of ellipse matched horns with different ellipse flanges size.

3.2.3 Spiral Aperture-Matched Horns

Fig.-3.17 presents field patterns of elliptic and spiral aperture matched horns compared with the conventional horn pattern. The spiral matched horn is shown in Fig.-3.18, where A' and B' are defined and introduced to match the ellipse dimensions as close as possible so that a fair comparison is made. More analysis of spiral aperture matching is done in the next section. The spiral geometry used is a hyperbolic spiral and has the polar equation $\phi r = B'$, ϕ being the polar angle, r polar radius, and B' is the asymptote of the spiral at small polar angles. The spiral dimensions are defined as:

A' : distance between the starting point of the spiral and the 180^o point, with the 0^o angle as shown on the spiral of Fig.-3.18.

B' : is the asymptote width of the spiral.

γ : tilt angle of the spiral, *i.e.* the angle between the 0^o axis of the spiral and the waveguide axis.

Examination of the far field patterns of plane flange, elliptic and spiral cylinder aperture-matched horns indicates that a convex structure can achieve more sidelobe level reduction and lower frequency sensitivity than flat structures.

3.3 Aperture-Matched Waveguides.

The first part of this section deals with aperture matching of waveguides using elliptical flanges, where in this case the flanges are directly attached to the waveguide aperture with the edges being along the tangency line as before except when the major axis makes an arbitrary tilt angle relative to the waveguide axis.

The flanges have significantly large electrical size compared to the waveguide size. The behaviour of the field patterns is investigated when varying the tilt angle β of the ellipse relative to the waveguide axis. The second part is a similar analysis where spiral shaped flanges are used for aperture matching and the corresponding field patterns are computed. The spiral geometry used here is the same as already described for spiral matched horns.

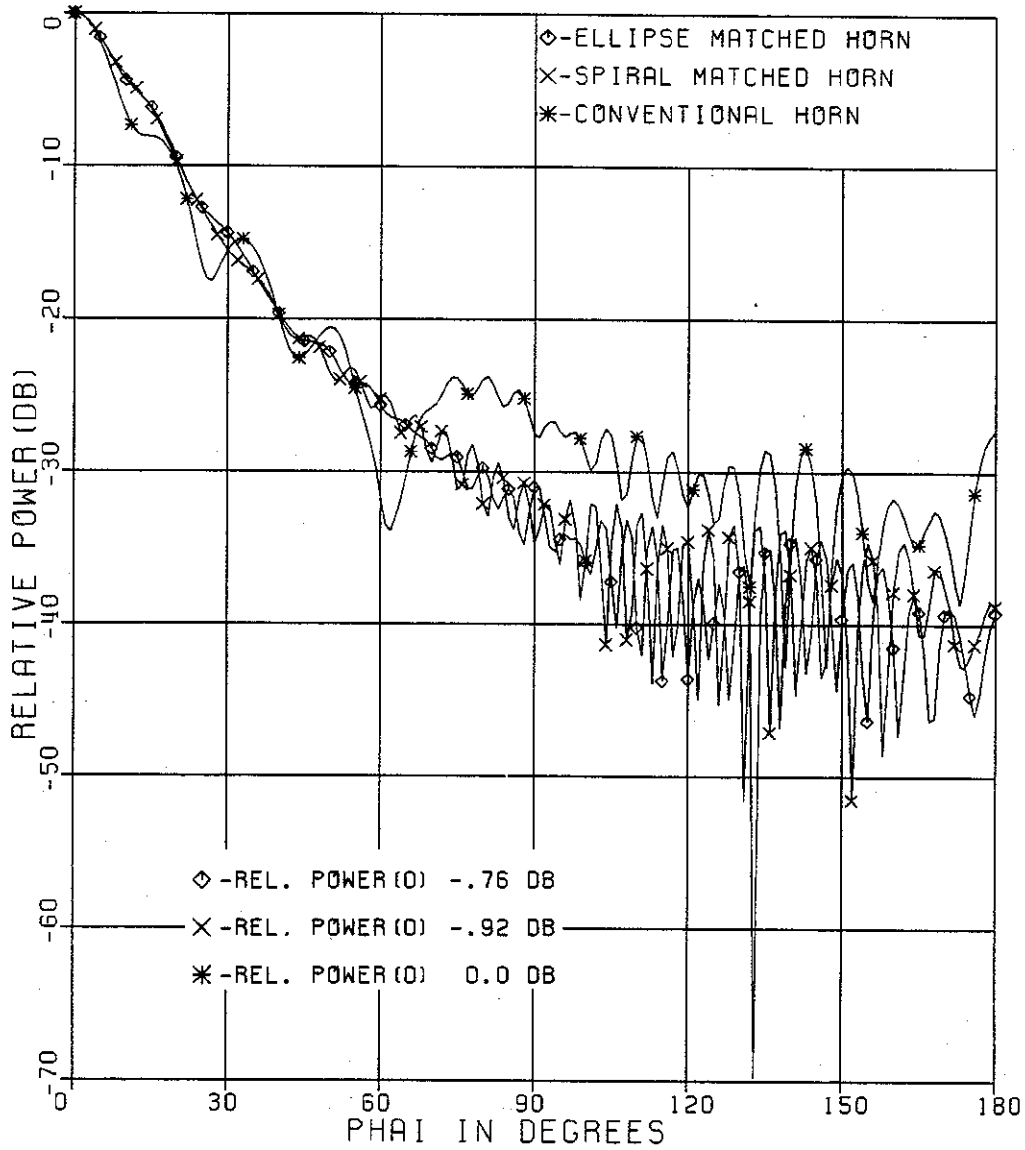

Fig.-3.17 *E*-plane radiation patterns of sectoral horns with $A = 3\lambda$, $B = A/2$ for the ellipse and spiral flanges.

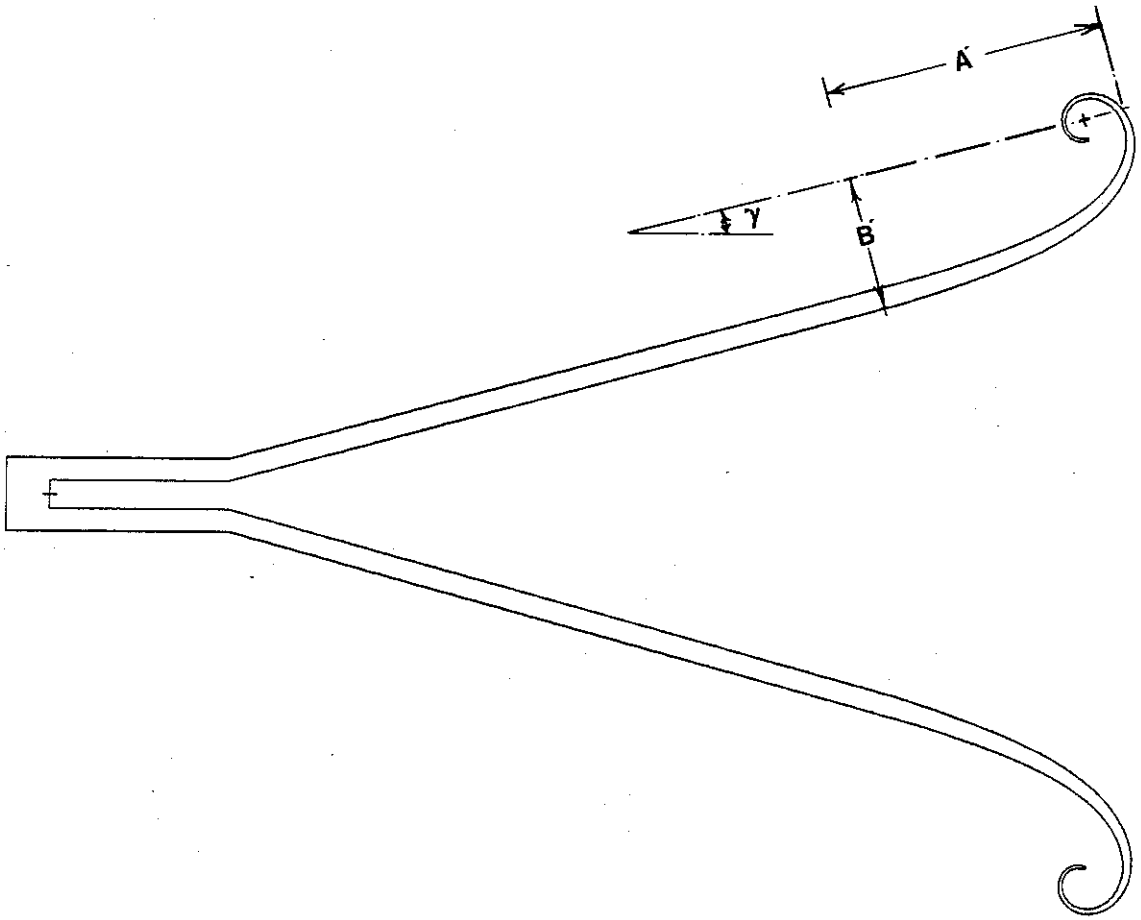

Fig.-3.18 Spiral aperture-matched horn with the spiral flange having dimensions A', B', and a tilt angle γ with the horn axis.

3.3.1 Ellipse Aperture-Matched Waveguides.

The waveguide used in this section is identical to the waveguide used in feeding the conventional horn as described earlier. Fig.-3.19 shows an elliptical cylinder with semimajor axis A and semiminor axis B, added to a waveguide aperture with tilt angle equal 0^o. The tilt angle of this structure is defined by the angle between the major axis of the ellipse and the axis of the waveguide as shown in Fig.-3.19a. Fig.-3.20 shows field patterns of ellipse matched waveguides with zero tilt angle for different sizes of ellipses and fixed minor to major axis ratio of 0.5. A broad beam width and low RPE level are observed. Fig.-3.21 shows field patterns for different minor to major axis ratios. Field patterns are also computed for various lengths of the elliptic cylinder and are shown in Fig.-3.22 which shows that sufficient length of the elliptic flange must be included to achieve a desired pattern. Half a flange corresponds to a half (or 180^o) ellipse. Frequency dependence of such aperture matching is shown in Fig.-3.23. A significantly wide beam width is achieved with tilting of the elliptic flange by angle β as shown in Fig.-3.19a. Field patterns are computed for different values of tilt angle β with A equal to 7.42λ and B equal to $A/2$ and using 120^o (*i.e. one third*) of the ellipse. Plots of these patterns are shown in Fig.-3.24 and indicate slight increase in the RPE level accompanied with broader beam width for an increase in the tilt angle.

3.3.2 Spiral Aperture-Matched Waveguides.

As mentioned earlier the spiral geometry used in this section is a hyperbolic spiral curve with the equation $\phi r = B'$. The dimensions of the spiral used in the simulation of the spiral matched waveguide are shown in Fig.-3.25 and are defined as in section 3.2.3. These dimensions are defined in a way to match as close as possible the dimensions of the ellipse in the inner region of the matched antenna so that, if desired, a fair comparison can be made between the elliptic and the spiral matched apertures. Fig.-3.26 shows far field patterns of a spiral matched waveguide for various electrical sizes of the spiral flange with tilt angle $\gamma=0^o$. A wide beam width and relatively low sidelobes are observed. Fig.-3.27 shows field patterns, with $A'=7.42\lambda$,

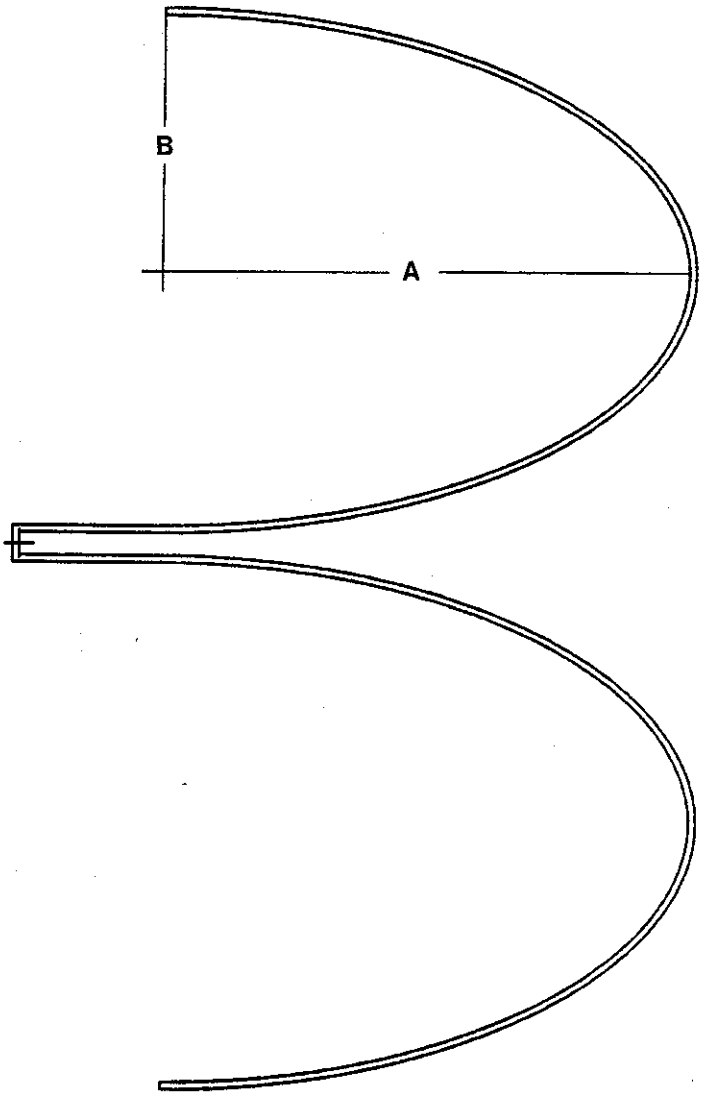

Fig.-3.19 Ellipse aperture-matched waveguide with the ellipse flange having a semi major axis A , a semi minor axis B and tilt $\beta=0^0$.

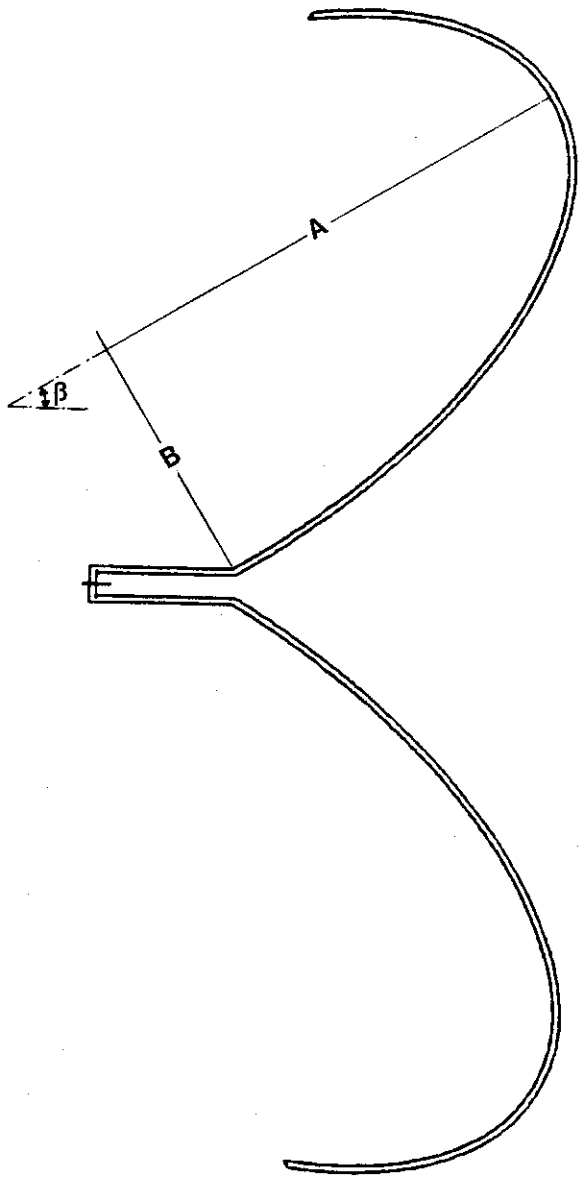

Fig.-3.19a Ellipse aperture-matched waveguide with the ellipse flange having a semi major axis A, a semi minor axis B, and a tilt angle β.

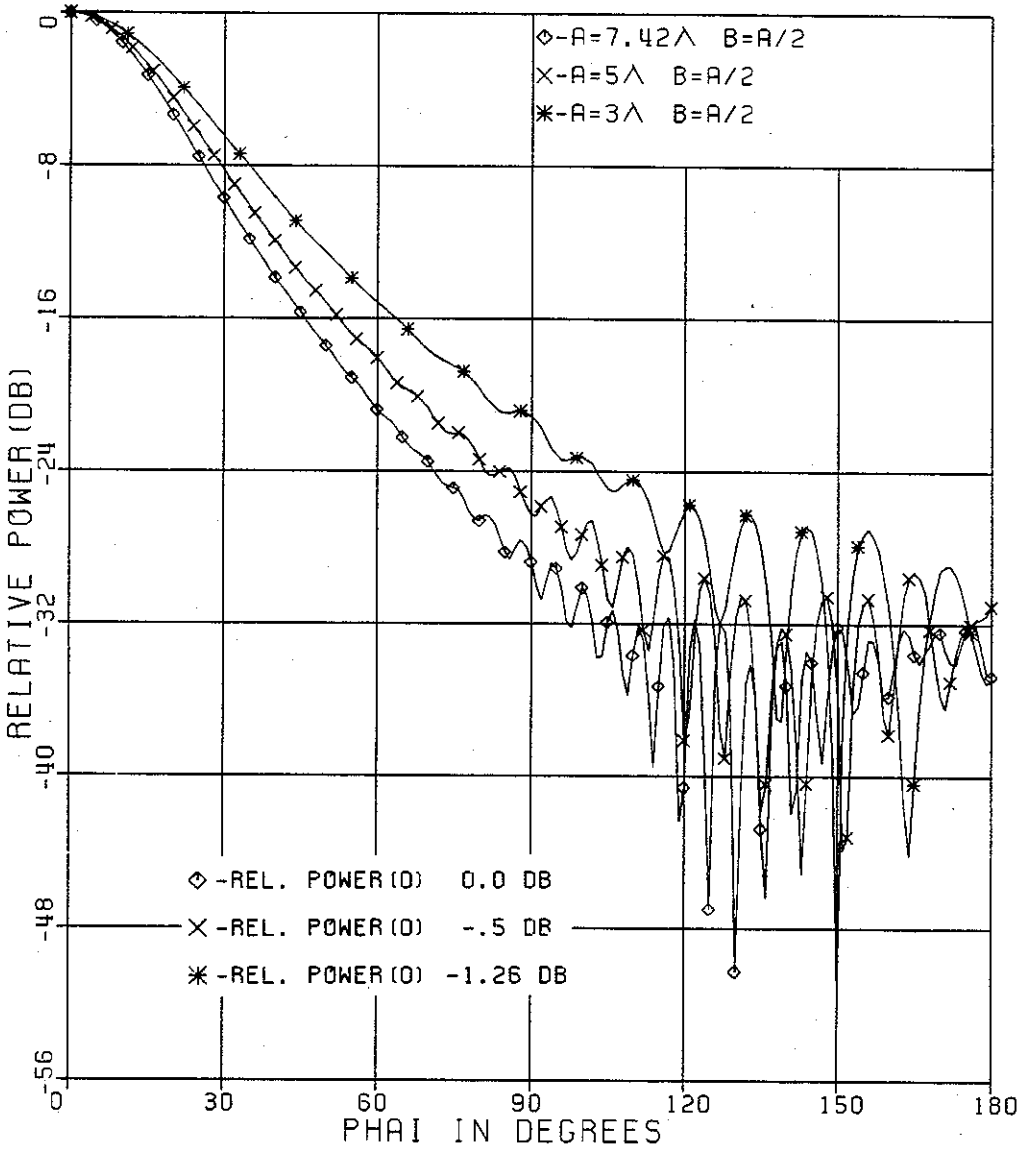

Fig.-3.20 *E*-plane radiation patterns of ellipse matched waveguides for different ellipse flange sizes.

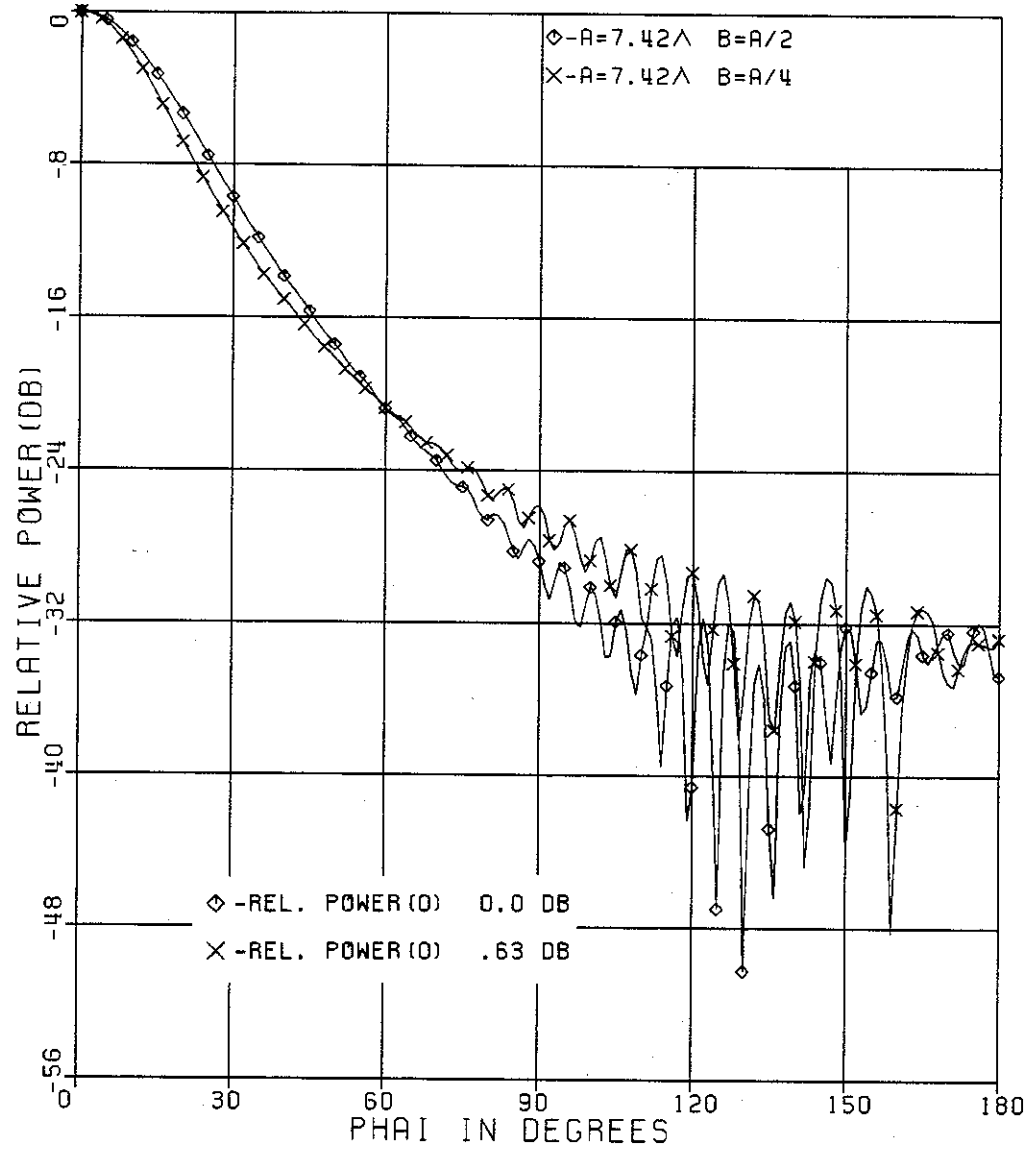

Fig.-3.21 ***E*-plane radiation patterns of ellipse matched waveguides for different major to minor axis ratios.**

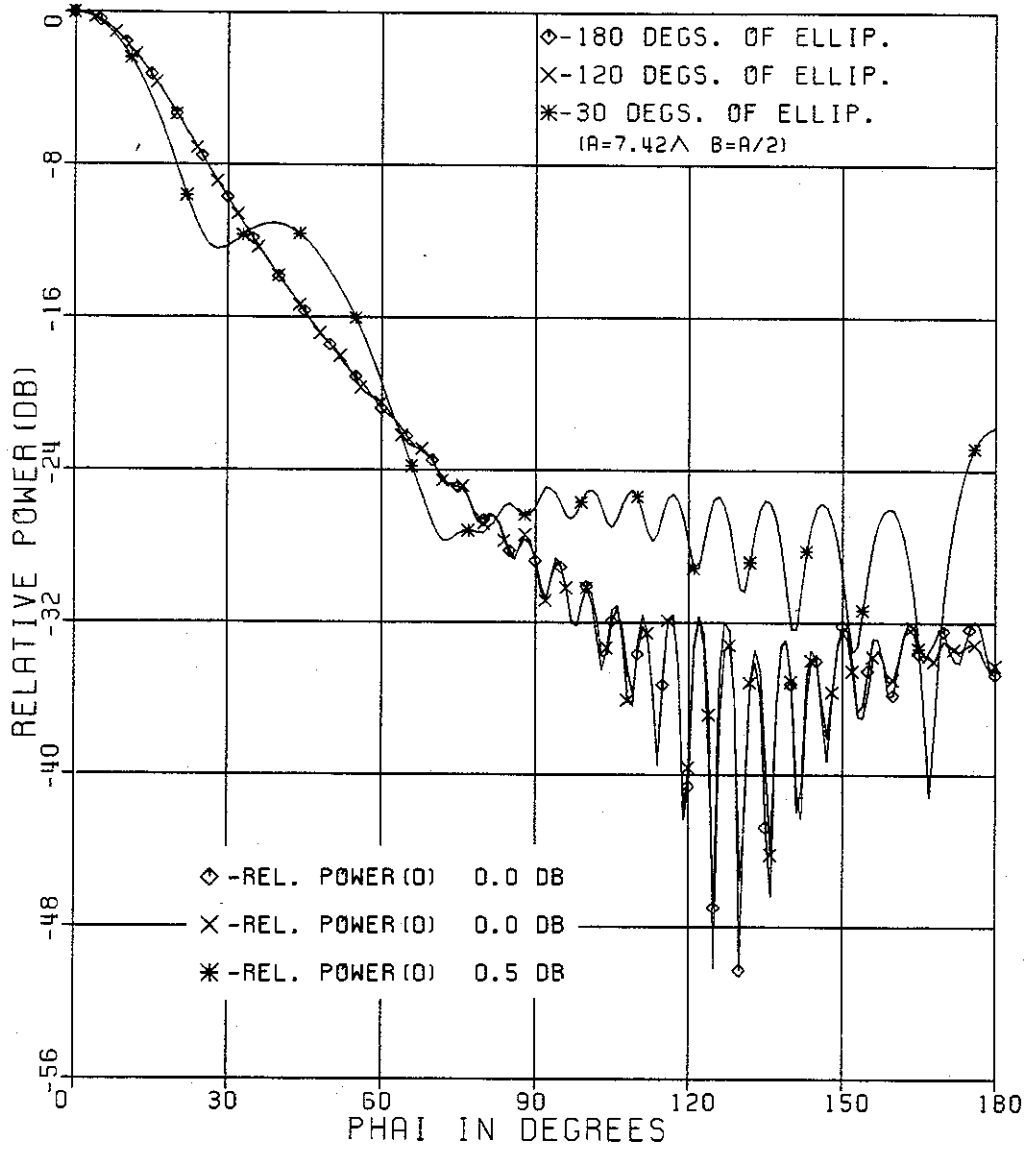

Fig.-3.22 *E*-plane radiation patterns of ellipse matched waveguides with different flange lengths.

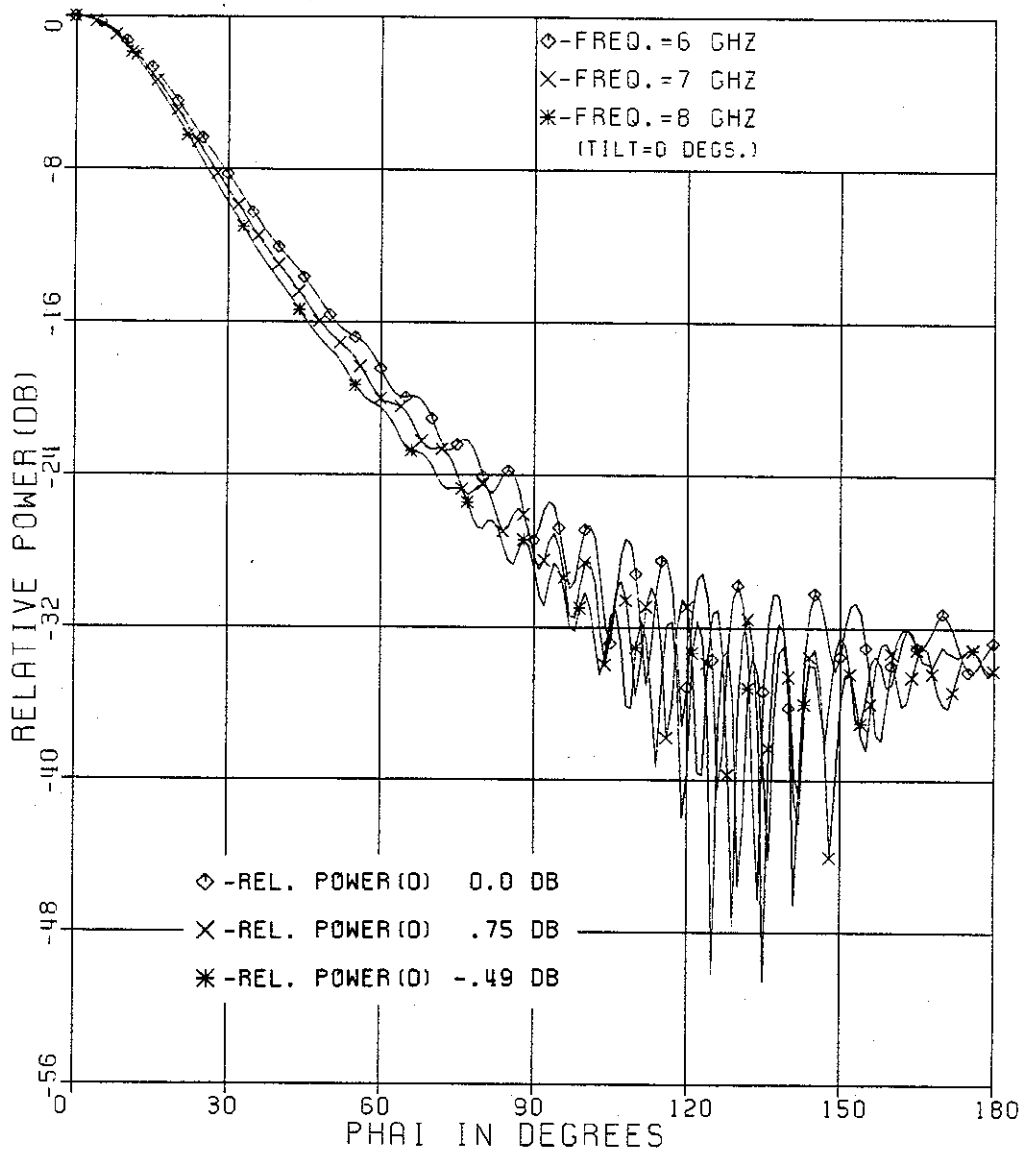

Fig.-3.23 E-plane radiation patterns of ellipse matched waveguides at different frequencies, $A = 7.42\lambda$, $B = A/2$ at F=8 GHZ.

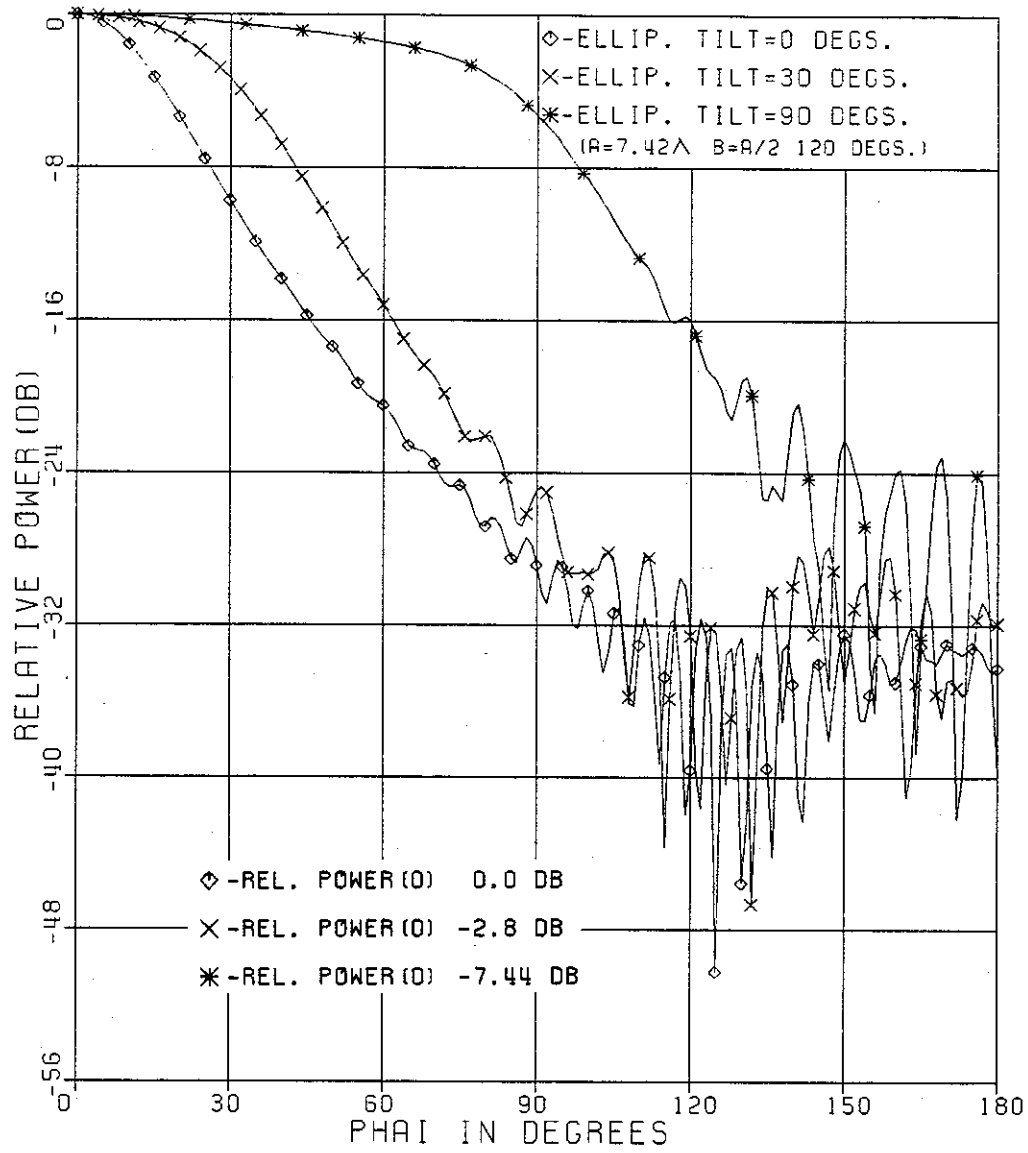

Fig.-3.24 ***E*-plane radiation patterns of ellipse matched waveguides at different tilt angles β.**

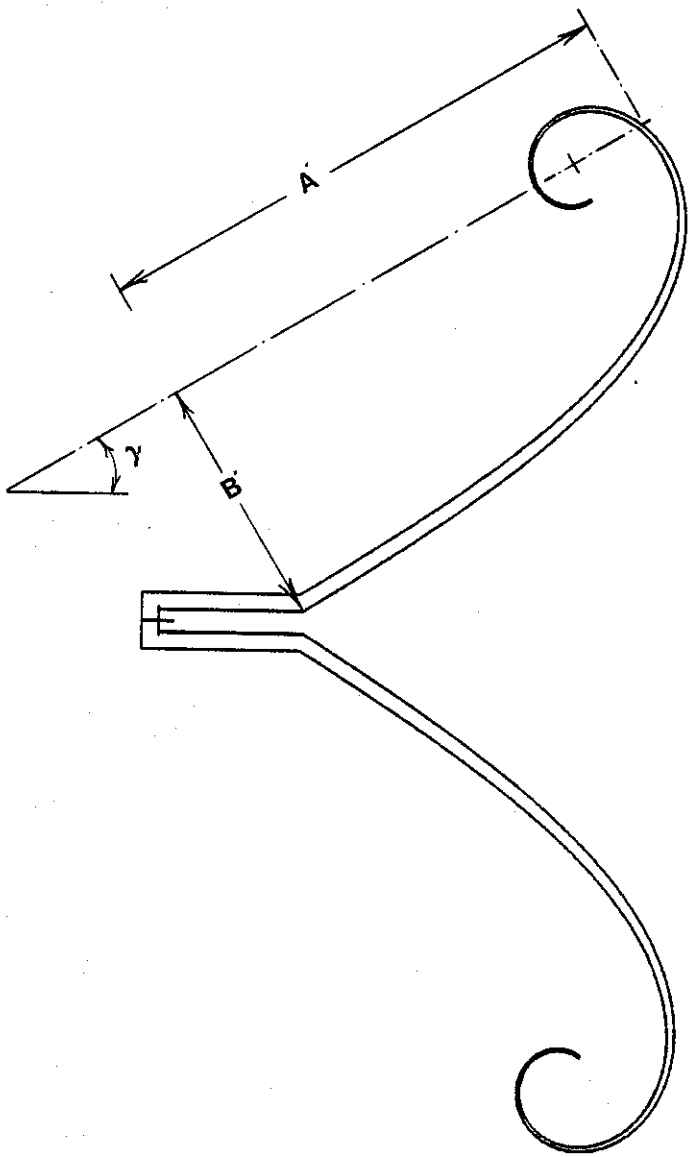

Fig.-3.25 Spiral aperture-matched waveguide with the spiral flange having dimensions A',B', and a tilt angle γ with the waveguide axis.

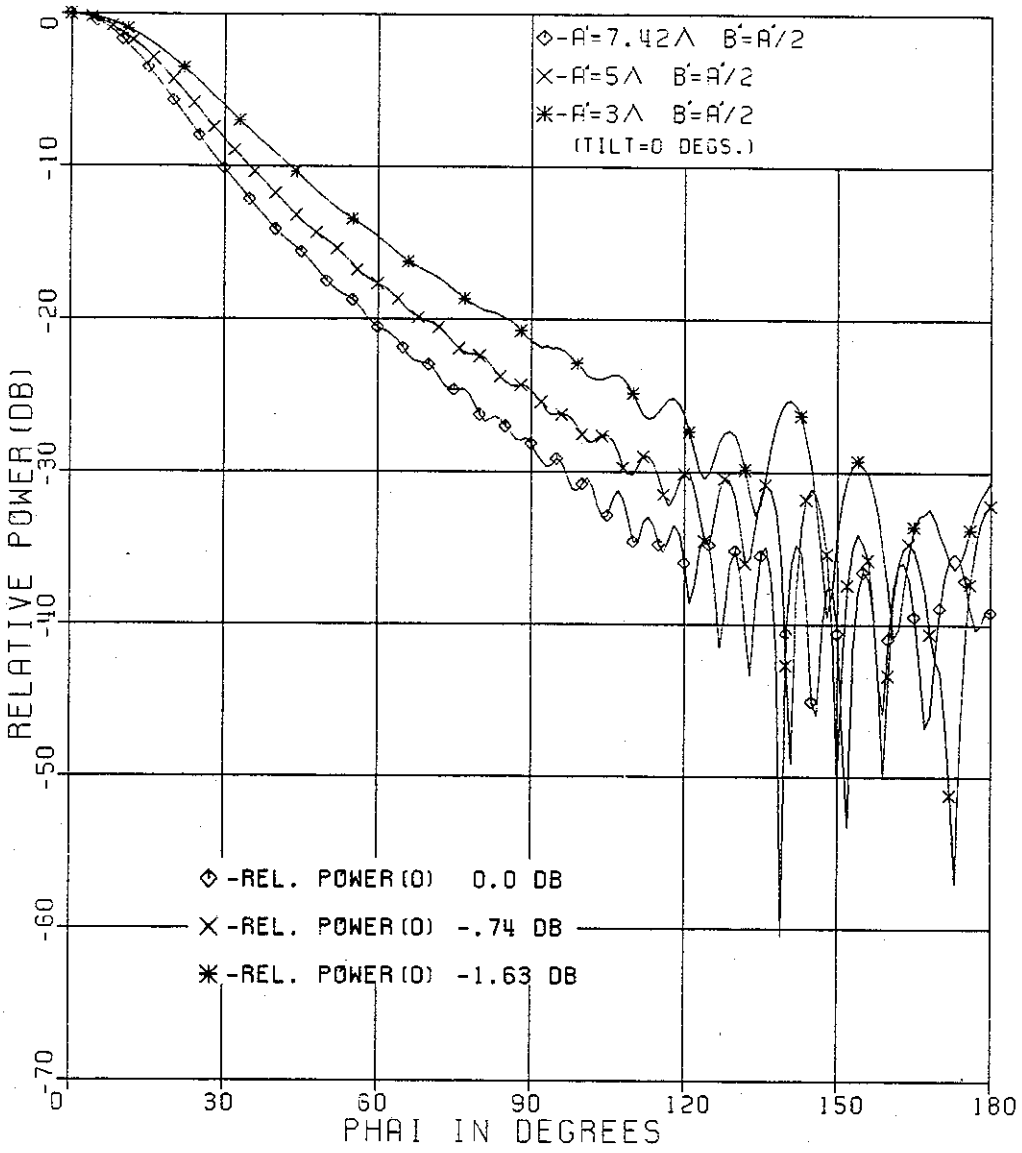

Fig.-3.26 *E*-plane radiation patterns of spiral matched waveguides with different sizes of the spiral flanges and for $\gamma=0$.

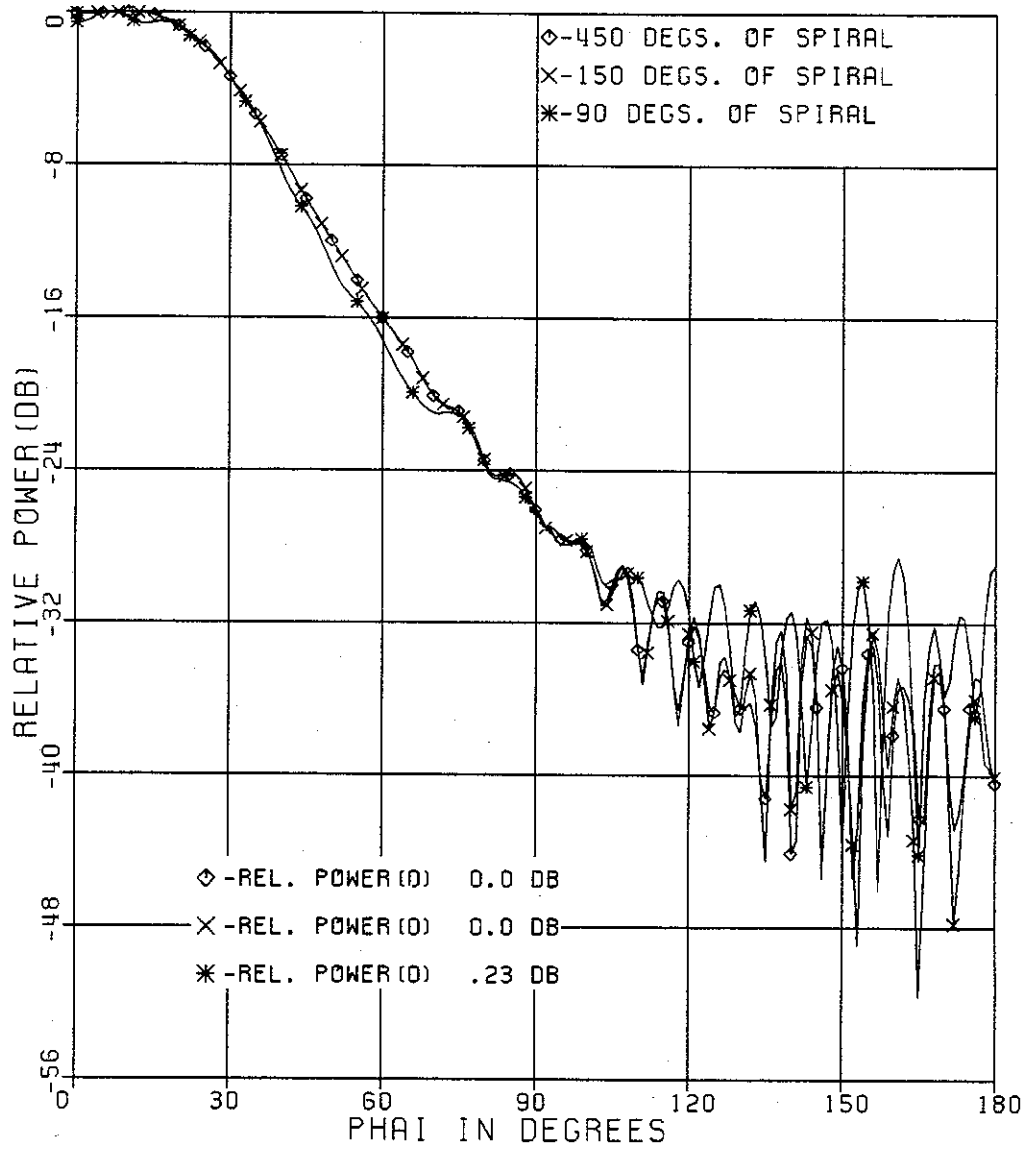

Fig.-3.27 E-plane radiation patterns of spiral matched waveguide with different spiral lengths, for $A'=7.42\lambda$, $B'=A'/2$, and tilt $\gamma=30^0$.

$B' = A'/2$, and a tilt of 30^o, computed for various electrical lengths of the spiral. Low frequency sensitivity is observed in Fig.-3.28 for the matched waveguide patterns computed at different frequencies. Changing the tilt angle of the spiral flange is also investigated and corresponding field patterns are computed and shown in Fig.-3.29. A significantly broad beam is observed with relatively low back lobe levels with increasing tilt angles.

In this section field pattern of ellipse and spiral aperture-matching of waveguides were investigated. It is shown also that very broad pattern (*i.e.* 160^o half power beam width) and back lobes around -30dB can be achieved by using spiral aperture matching of a waveguide. It should be noted that although the numerical method used in solving for the field patterns requires the use of at least 10 segments per wavelength, up to 40 segments per wavelength were used to simulate the curved surfaces, so that more accurate simulation of the geometry is achieved especially in the spiral zone where the slope varies rapidly.

3.4 Discussion

It should be clear that the terms that determines the shape and power level of the horn field pattern are directly related to the geometric shape and excitation of the horn antenna. In the case of a pyramidal horn, the dominant propagating mode within the the horn has uniform amplitude in the E-plane and a sinusoidal amplitude distribution in the H-plane in which the field vanishes at one pair of the walls. Thus, only diffraction by the E-plane edges contributes significantly to the E-plane and H-plane diffraction patterns [32]. Examining the E-plane of a pyramidal horn using the geometrical theory of diffraction (GTD) analysis suggested by Russo *et al.* [32], indicates that the horn pattern is dominated by three terms *i.e.*, direct throat radiation plus two edge diffraction terms as illustrated in Fig.-3.30. The throat region appears as an electrically small radiator having a smooth pattern across the horn flare angle and zero otherwise. On the other hand the aperture edges are widely separated from the throat and they interfere constructively and destructively with the throat radiation especially if the edge diffractions are of significant

magnitude as in the conventional E-plane horn pattern case. The basic first-order diffraction equation that describes the above mentioned situation is given by [33], *i.e.*

$$\mathbf{E}^d = \mathbf{E}^i \vec{\mathbf{D}}(d',s',\gamma')A(d',s')e^{-jks'} \tag{3.4.1}$$

where $\mathbf{E}^i$ is the field incident on the edge, $\vec{\mathbf{D}}(d',s',\gamma')$ is the diffraction coefficient associated with appropriate geometry and $A(d',s')$ is the diffracted field spread factor. d' is the distance from the source to the diffraction point, s' is the distance from the diffraction point to the receiver, and γ' represents the various angular dimensions associated with the shape of the given geometry.

As stated earlier, the dual and hybrid-mode horns reduce the magnitude of the diffracted field $\mathbf{E}^d$ in equation 3.4.1 by reducing the magnitude of the field $\mathbf{E}^i$ incident on the edge and an improved pattern performance was hence achieved. Another approach in reducing $\mathbf{E}^d$ is done by modifying the geometry of the structure at the edges in order to reduce the magnitude of the diffraction coefficient and/or spread factor [19], and this was done by the aperture-matched horns introduced by Burnside [19], and analyzed in this chapter. When an incident ray strikes a smooth, curved perfectly-conducting surface at grazing incidence, part of its energy is diffracted into the shadow region as illustrated by Fig.-3.31 [34]. In Fig.-3.31, the incident wave undergoes reflection from the illuminated portion of the scatterer and undergoes diffraction at the shadow boundary at point A_1 which is a point of tangency for the incident ray. At this point a portion of the energy is trapped resulting in a wave which propagates in directions tangent to the surface(*e.g. point* B_1). This wave that propagates along the surface is known as *creeping wave*. The creeping wave can be described by a launching coefficient at the point of capture, by a diffraction coefficient at the point of radiation, by an attenuation factor to account for the rate of radiation, and by a description of the path on the scatterer traversed by the creeping wave.

Physically, the diffracted rays originating from the aperture edges are due to the sudden interruption of the flow of the current at the edges of the horn walls. Since infinitely long horn walls are physically impossible, attaching smooth convex

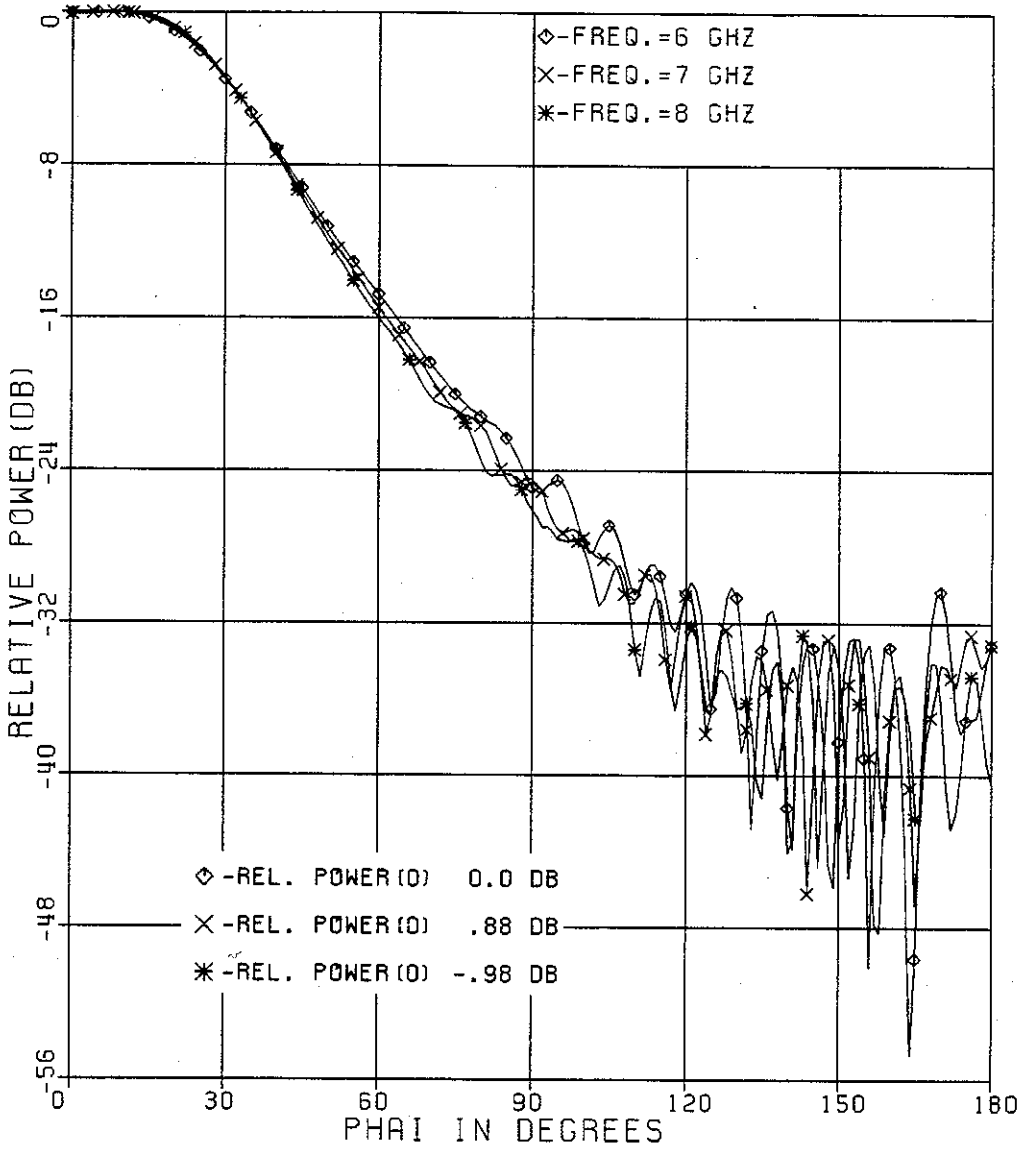

Fig.-3.28 E-plane radiation patterns of spiral matched waveguides at different frequencies, for $A'=7.42\lambda$, $B'=A'/2$ at F=8 GHZ, and $\gamma = 30^0$, using 450 degs. of the spiral.

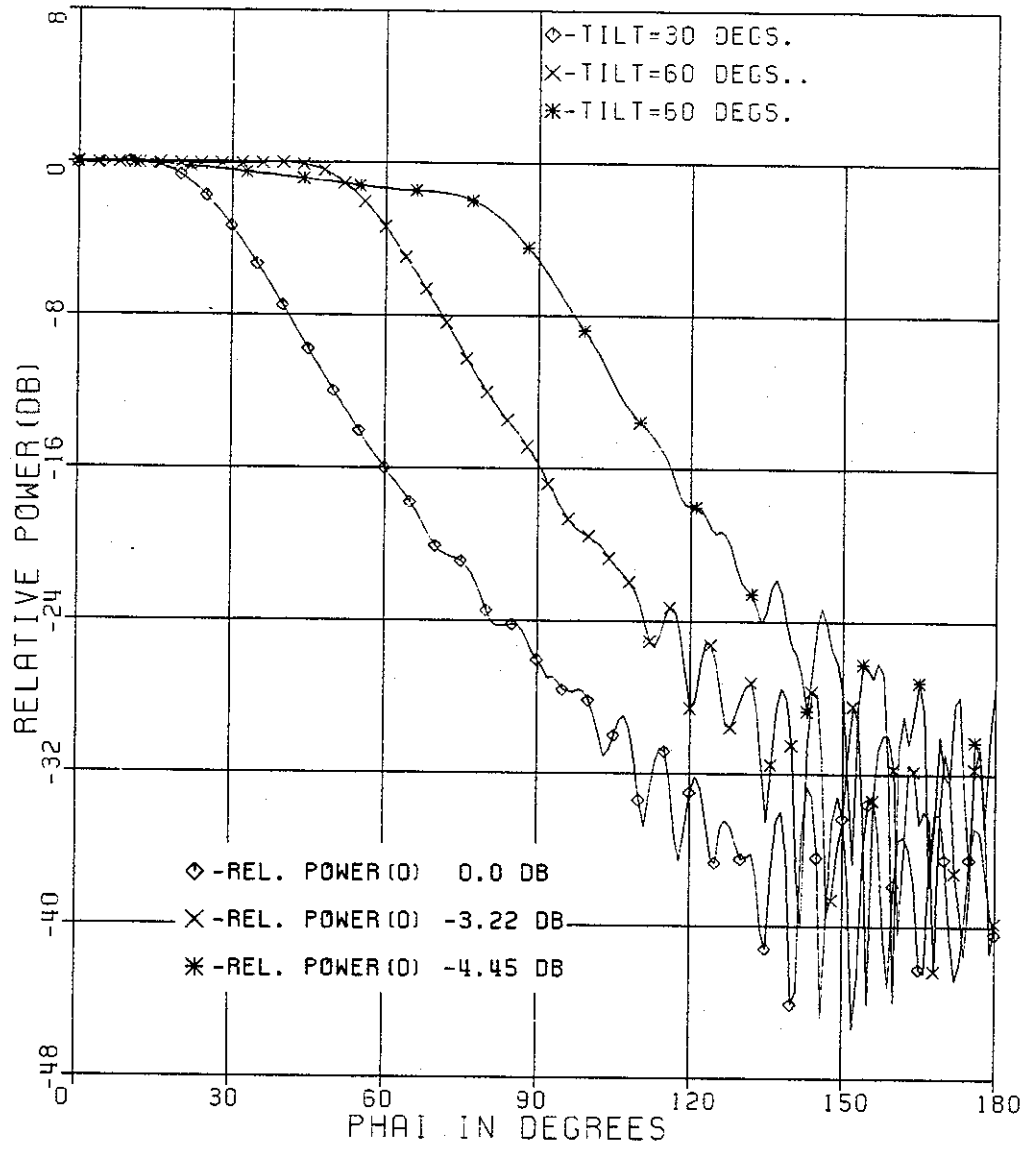

Fig.-3.29 *E*-plane radiation patterns of spiral matched waveguides for different tilt angles, and for $A'=7.42\lambda$, $B'=A'/2$.

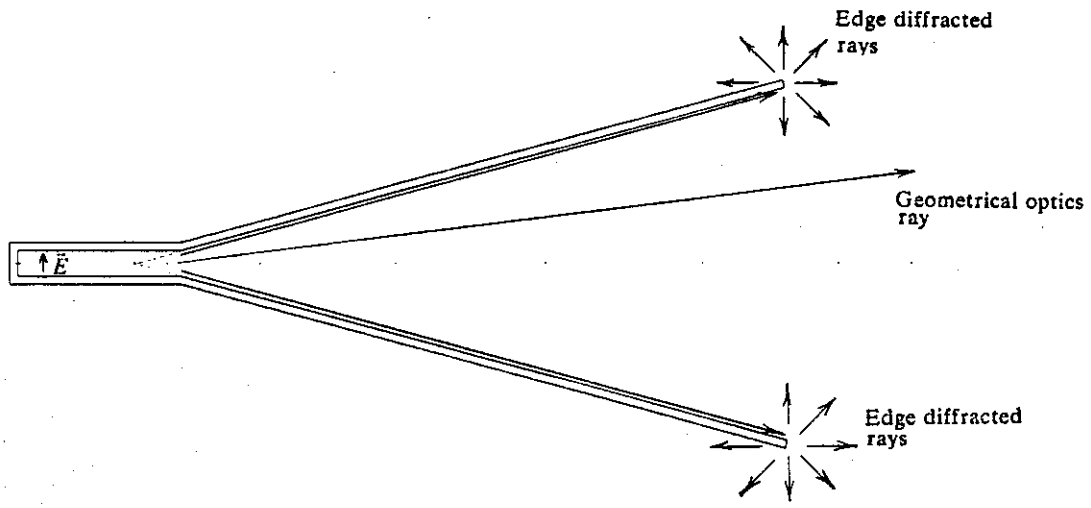

Fig.-3.30 GTD terms for pyramidal horn E-plane pattern.

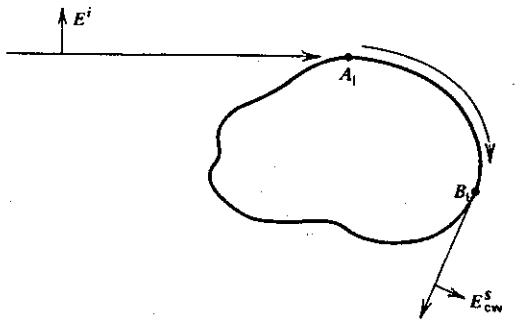

Fig.-3.31 Creeping wave concept of diffraction by a curved surface.

structures to the horn edges provides an easy way to remove the discontinuity of the edge and shifts it to a position where the current has a relatively low magnitude due to radiation, resulting in a lower magnitude diffracted field radiating away from the aperture area of the horn as done in the aperture-matched horns. The aperture matching of the horns and waveguides analyzed in this chapter used flat, and convex (elliptic and spiral) shaped flanges to provide a continuous path for the current (creeping current). Fig.-3.32 shows the GTD pattern analysis model of an ellipse aperture-matched horn, and shows in this case the diffracted field along the ellipse surface radiating away from the aperture to the outside back region of the horn.

A significant reduction of sidelobe and backlobe levels in the field patterns of horn and waveguide antennas is achieved when adding curved conducting flanges to the edges of these antennas. In this case the fields incident from the feed waveguide on these curved surfaces will diffract in a way that was described earlier radiating gradually in the sidelobe and backlobe regions of horn and waveguide antennas. Aperture matching with a flat plane flange reduced the side and backlobe levels slightly as compared with the conventional horn. The convex shaped flanges provided a smoother discontinuity for the antennas, which decreased still further side and backlobe levels. More reduction in side and backlobe levels is observed for electrically larger curved flanges because of the smooth transition between the horn walls and free space. A broader beam width for convex flange aperture matching is also observed. This is due to the tapering of the aperture field of the waveguide since now the aperture field is terminating along a wide curved surface while before the termination was along a thin edge. Also better performance at higher frequencies is observed for such aperture matching, which is attributed to the convex flanges being electrically larger. Comparing ellipse and spiral flange aperture matching, it is observed in the case of horns that both geometries have similar effects on the sidelobe level reduction. In the case of waveguide aperture matching, the spiral provided a slightly better performance than ellipse aperture matching especially in the case of flared aperture-matched waveguide.

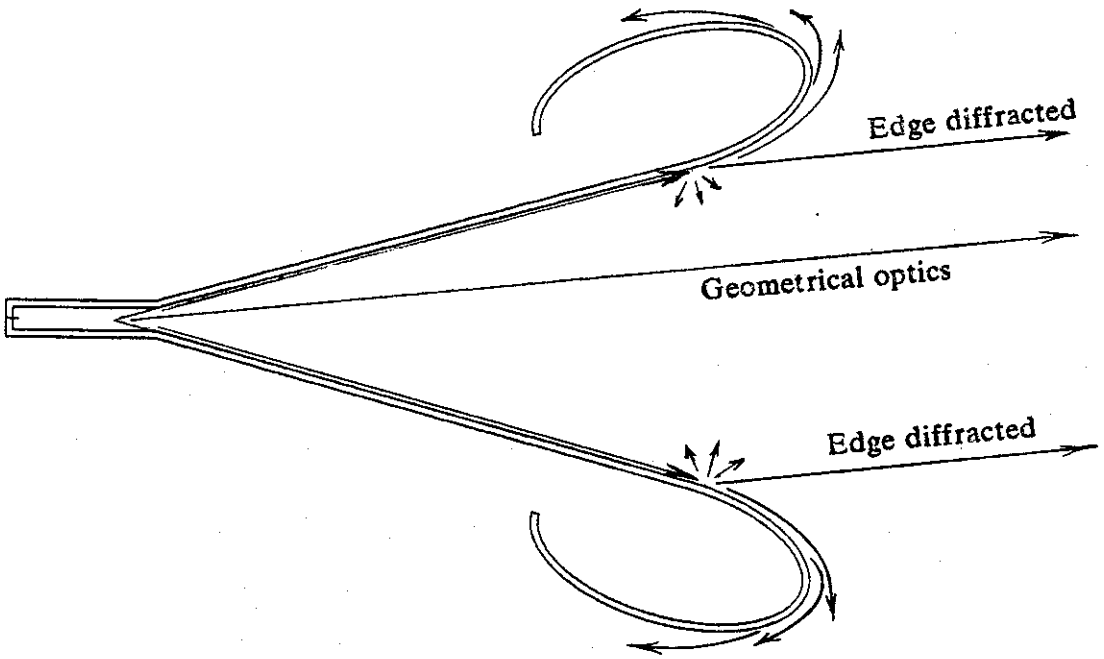

Fig.-3.32 GTD *E* -plane pattern analysis for a convex flange aperture-matched horn.

CHAPTER IV

Aperture-Matched Cylindrical Reflectors.

4.1 Introduction

In this chapter the concept of attaching of curved (elliptical and spiral) flanges to the edges of an aperture antenna is applied to cylindrical parabolic and offset cylindrical parabolic reflectors. Although aperture matching has a practical use in compact ranges which only involves the near field pattern of the range reflector, aperture matching causes a significant reduction in the far lobe levels of reflectors.

4.2 Aperture-Matched Parabolic Cylindrical Reflectors.

The simulation of the problem for a numerical solution, involves a cylindrical parabolic reflector having size $D = 10\lambda$, $f/D = .433$, and the edges of the reflector are subtended in a 120^o angle when viewed from the focus. This reflector is illuminated by 11dB tapered field supplied from an actual feed horn excited by a magnetic line source. The dimensions of the reflector and its feed are shown in Fig.-4.1. It should be noted that such simulation of the antenna includes the diffraction by all the edges, the coupling elements, and also the feed blockage of the secondary pattern of the antenna. Thus all diffraction effects are included in the numerical solution except for the effect of the struts that hold the feed. The horn feed used to illuminate the reflector, whose field pattern is shown in Fig.-4.2, provides 11dB taper and has a relatively high back lobes (−18dB). Other feeds with lower side and back lobes could have been used, but this would have required extensive computations and computer capacity, and hence would have limited the flexibility of using rolled flanges at the reflector edges. For a maximum gain reflector the phase center of the feed must coincide with the focus of the reflector. This was taken care of by running several computations for different positions of the horn, and the feed position

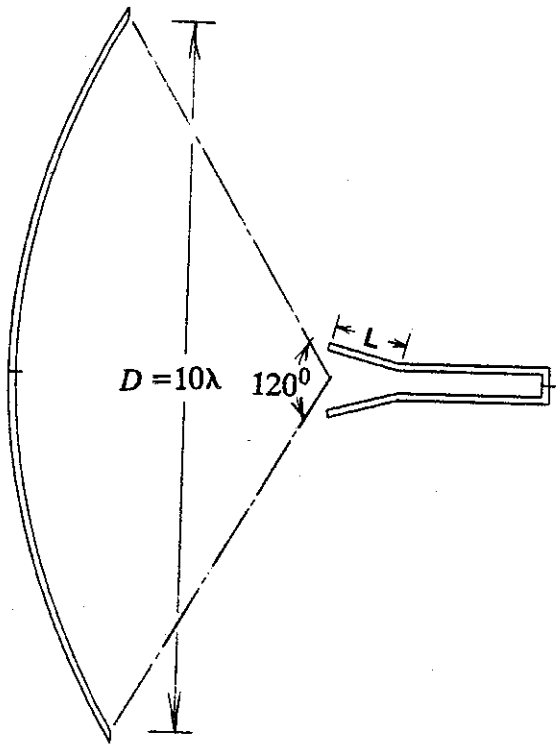

Fig.-4.1 Schematic diagram of the simulated cylindrical parabolic reflector with $D = 10\lambda$, $f/D = .433$, and wall thickness of 0.1λ.

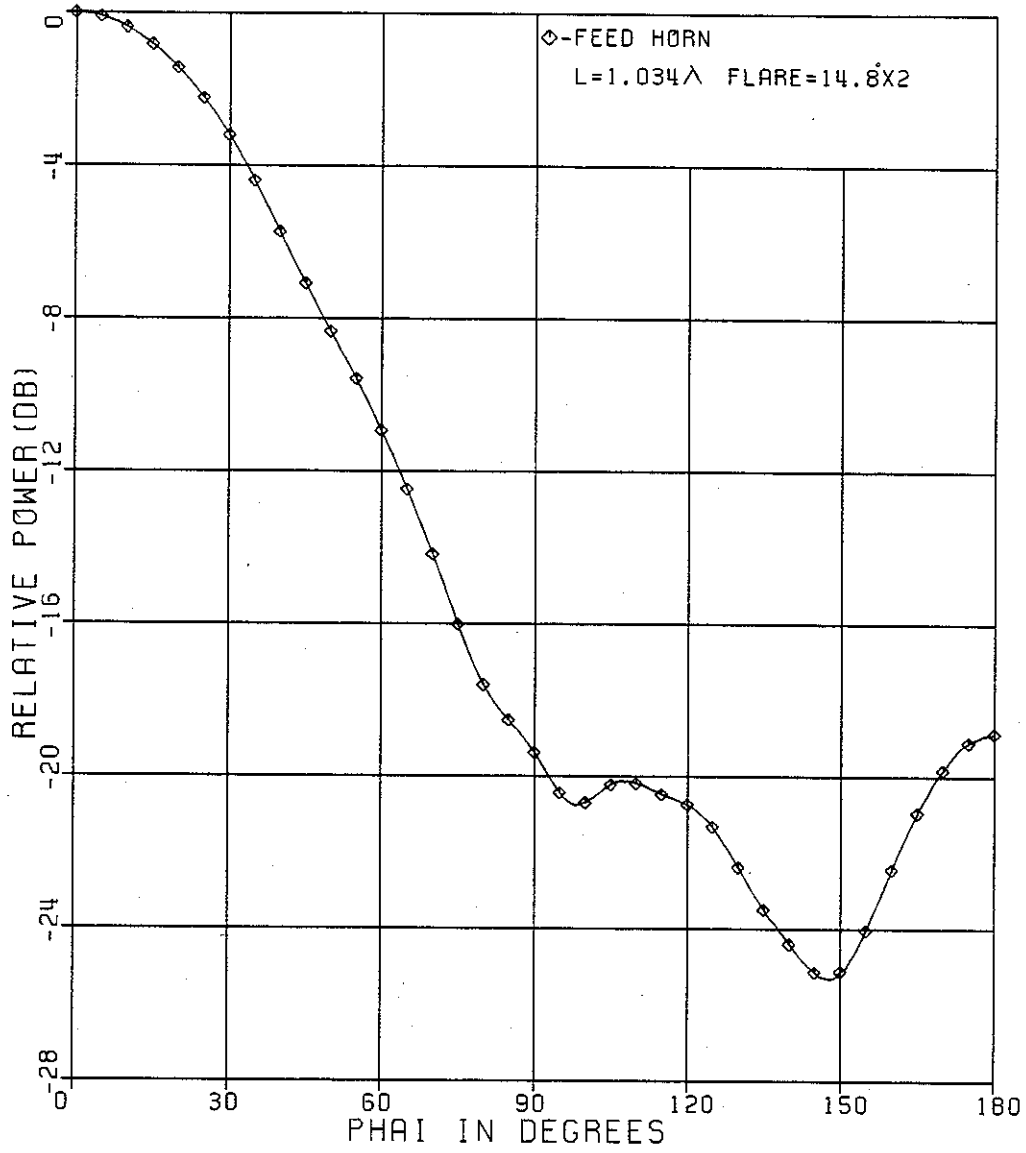

Fig.-4.2 E-plane radiation pattern of the horn used to feed the cylindrical parabolic reflector with $11dB$ tapered field.

for the maximum gain pattern is chosen.

4.2.1 Ellipse Aperture-Matched Parabolic Cylindrical Reflectors.

In this section investigation of the elliptical flanges attached to the reflector edges is investigated. An elliptic cylinder, as before, will have a semimajor axis A and a semiminor axis B as shown in Fig.-4.3. Fig.-4.4 shows the field patterns of the unmatched and elliptic matched reflectors with $A=4\lambda$ and $B=2\lambda$. The plots show a decrease in side lobes in the $\phi=100^o$ to 120^o region and a considerable decrease in the back lobe levels achieved by the matched reflector. Investigating the effect of using different electrical lengths of the ellipse is done for $A=4\lambda$ and $B=A/2$, and the field patterns are computed and shown in Fig.-4.5, where a 180^o ellipse is the half ellipse shown. Field patterns are also computed for different electrical sizes of the elliptical flanges and are shown in Fig.-4.6. This figure shows that more side and back lobe reduction is achieved with electrically larger flanges. Frequency dependence is also investigated and Fig.-4.7 shows patterns of a matched reflector computed at different operating frequencies.

4.2.2 Spiral Aperture-Matched Parabolic Cylindrical Reflectors.

Here a hyperbolic spiral is used for aperture matching of the reflector. The dimensions A' and B' of the spiral follow the same definitions given in section 3.2.3. Fig.-4.8 shows radiation patterns of the unmatched cylindrical reflector of Fig.-4.1 and a spiral matched reflector of Fig.-4.9 corresponding to $A'=4\lambda$, and $B'=2\lambda$. These plots show significant far and back lobe level reduction achieved by the spiral matched reflector. Fig.-4.10 is a plot of field patterns for different electrical lengths of the spiral whereas Fig.-4.9 shows a 420^o spiral for illustration purposes. Fig.-4.11 shows field patterns of matched reflectors for various electrical sizes of the spiral. Lower side and back lobes are also observed for electrically large spiral matching. Frequency dependence is also checked for spiral matched reflector and corresponding plots computed for different frequencies are shown in Fig.-4.12.

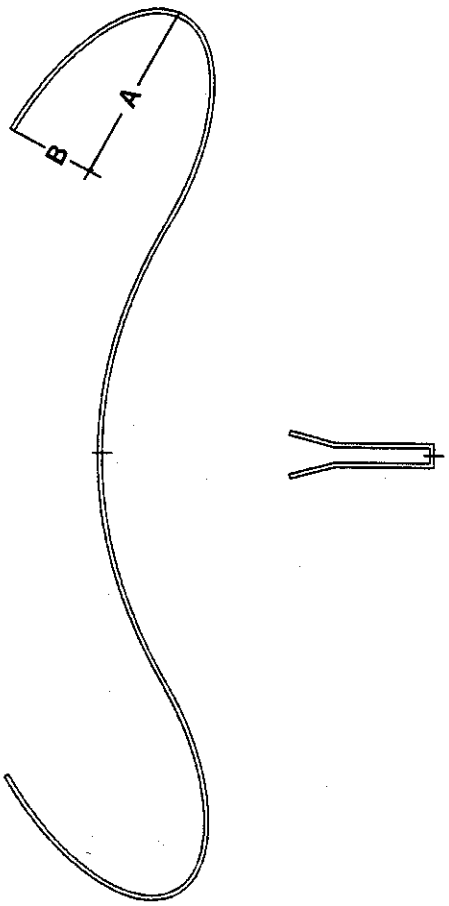

Fig.-4.3 Elliptic aperture-matched cylindrical parabolic reflector with the ellipse flange having semimajor axis A, and a semiminor axis B.

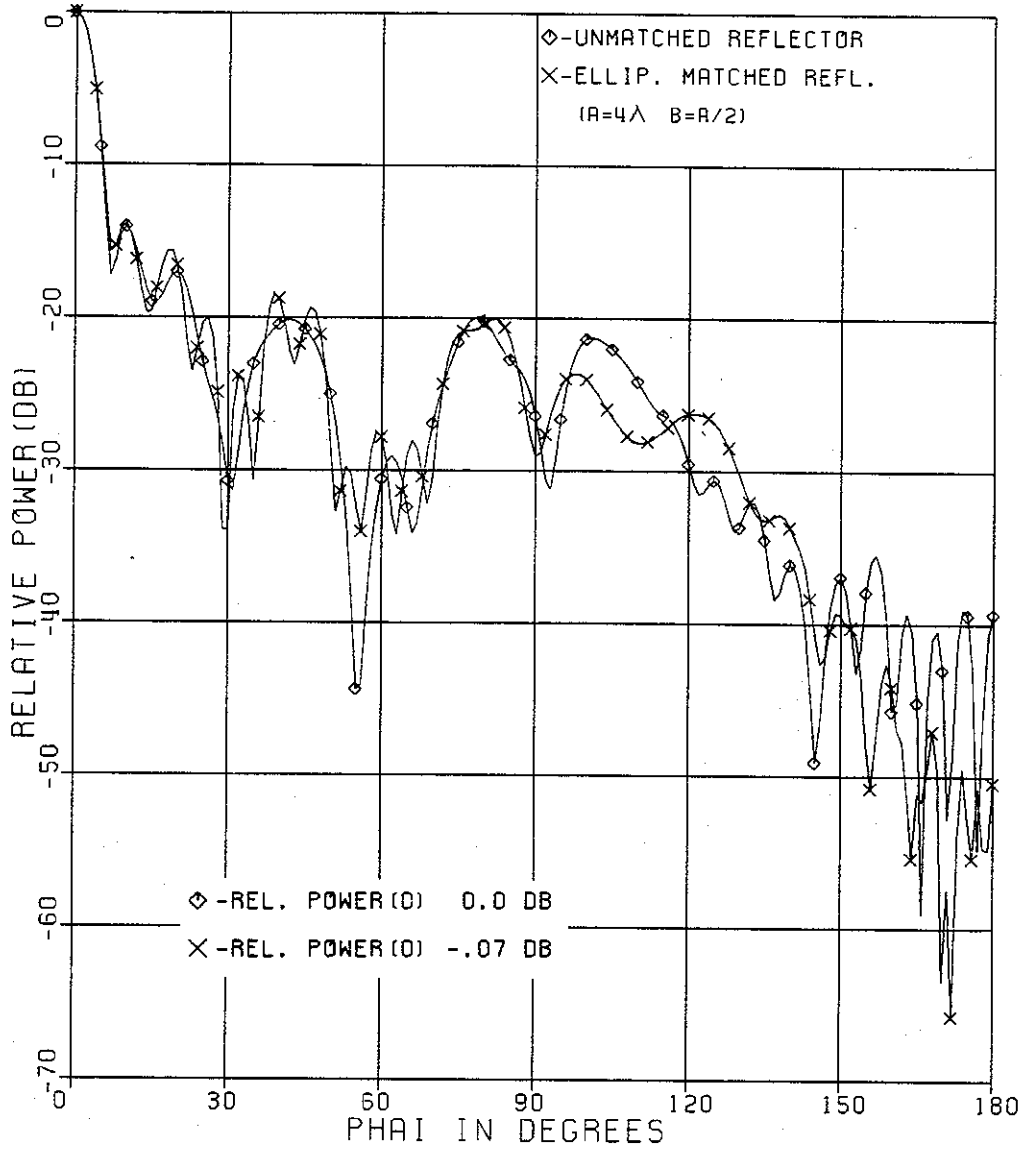

Fig.-4.4 *E*-plane radiation patterns of unmatched and elliptic matched cylindrical parabolic reflectors for $D = 10\lambda$, and $f/D = .433$.

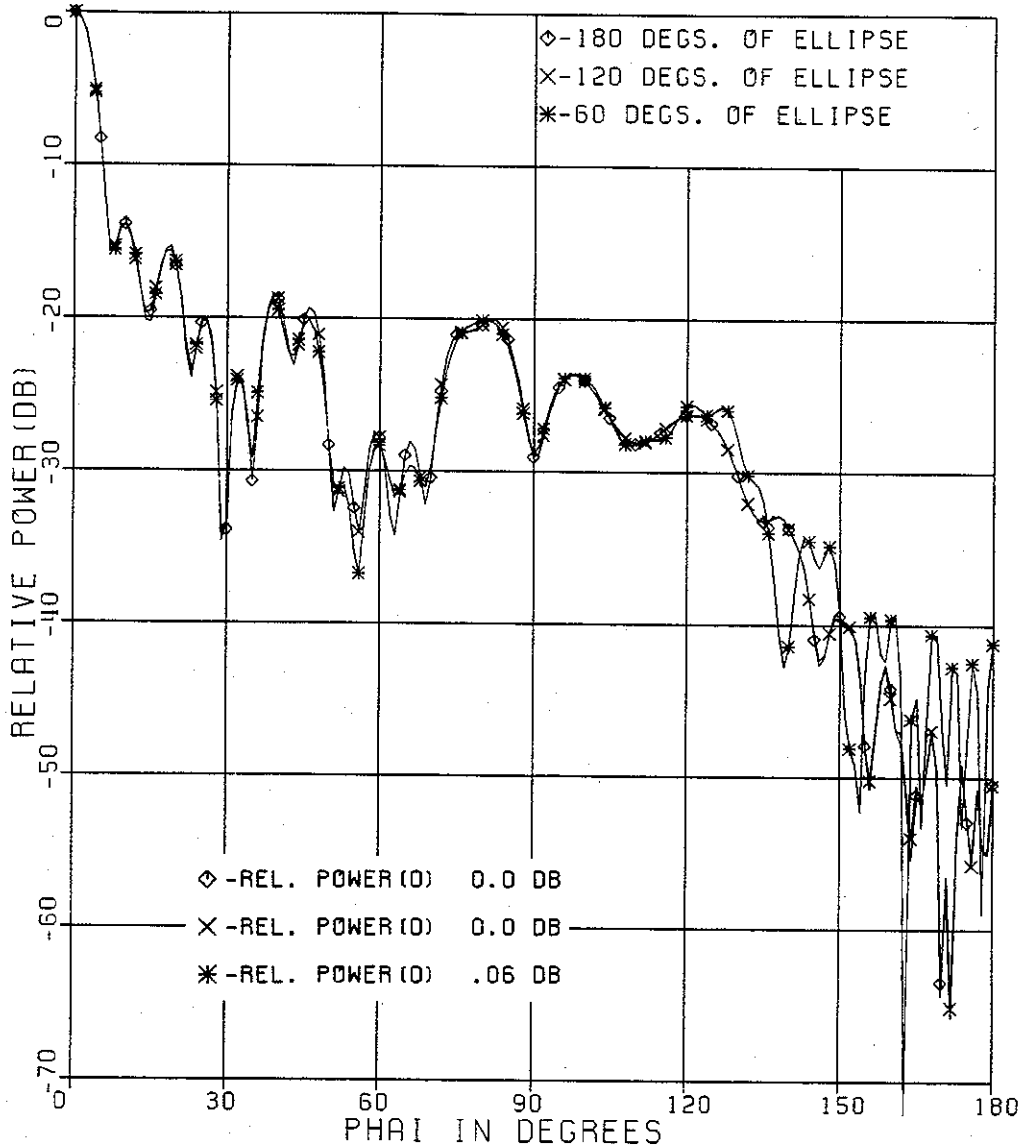

Fig.-4.5 *E*-plane radiation patterns of elliptic matched cylindrical parabolic reflectors with different elliptic flange lengths, for $D = 10\lambda$, $f/D = .433$, and $A = 4\lambda$ $B = A/2$.

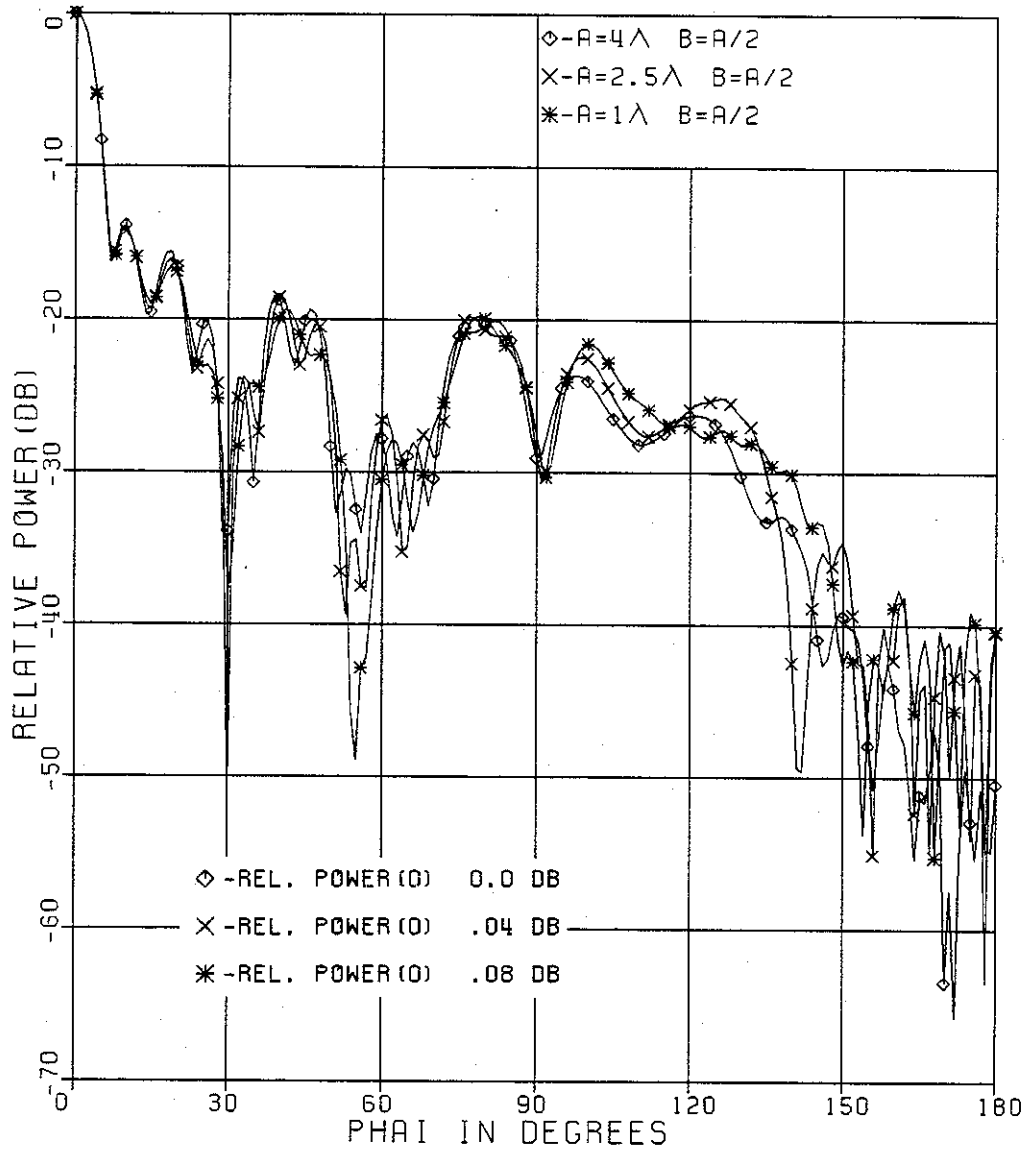

Fig.-4.6 E-plane radiation patterns of elliptic matched cylindrical parabolic reflectors with different elliptic flange sizes, for $D = 10\lambda$, and $f/D = .433$.

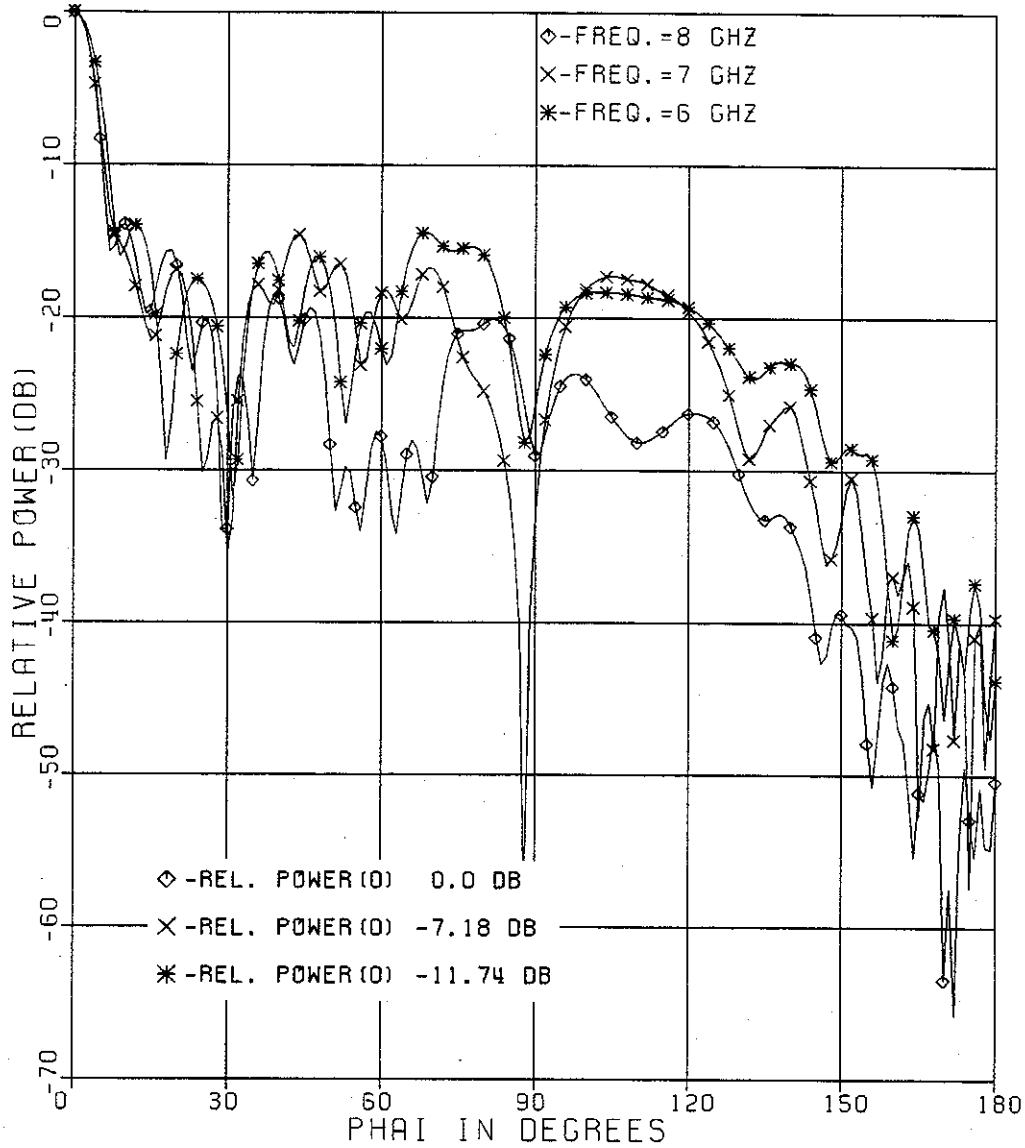

Fig.-4.7 E-plane radiation patterns of elliptic matched cylindrical parabolic reflectors at different frequencies, with $D = 10\lambda$, $f/D = .433$, and $A = 4\lambda$ $B = A/2$ at F=8 GHZ.

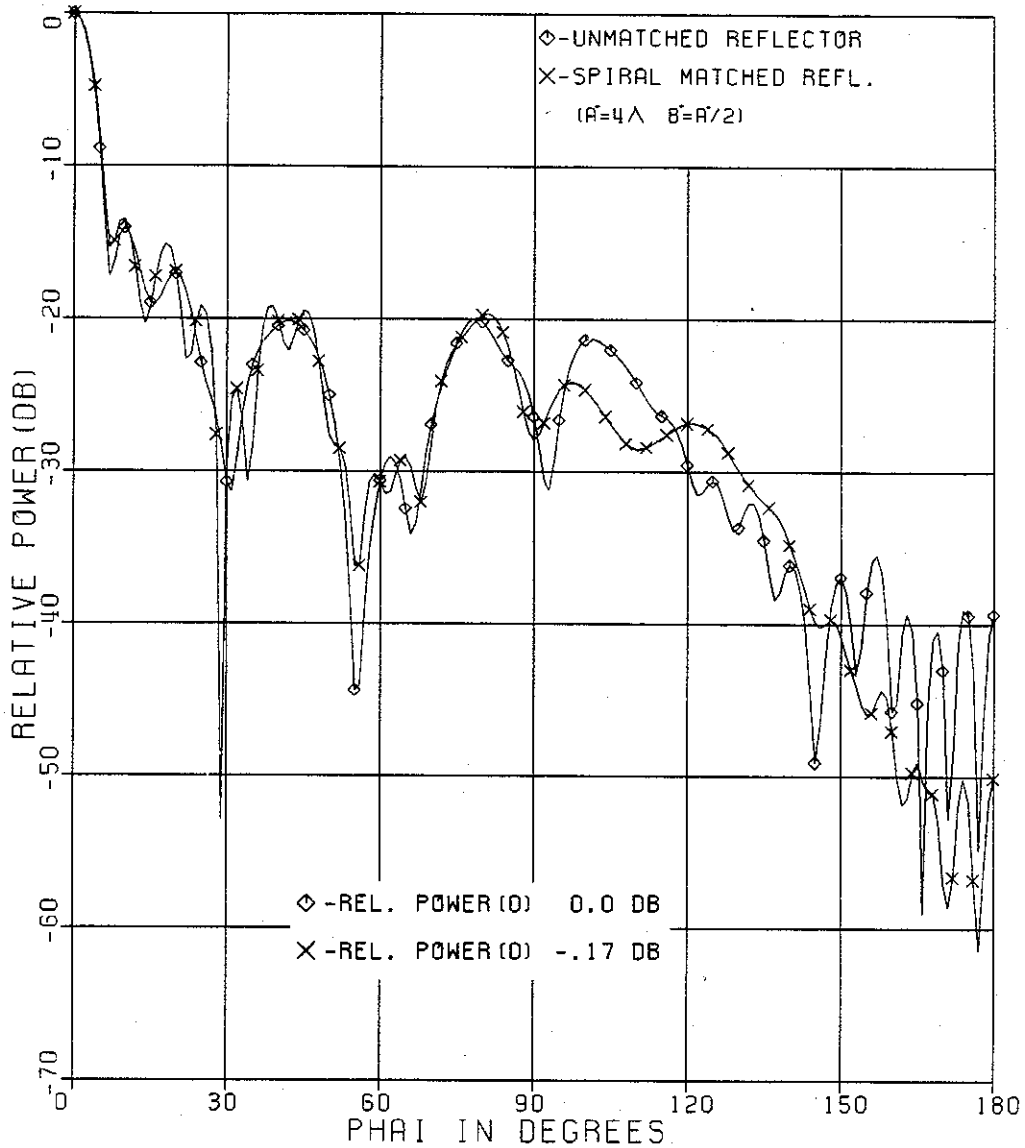

Fig.-4.8 E-plane radiation patterns of unmatched and spiral matched cylindrical parabolic reflectors, with $D = 10\lambda$, and $f/D = .433$.

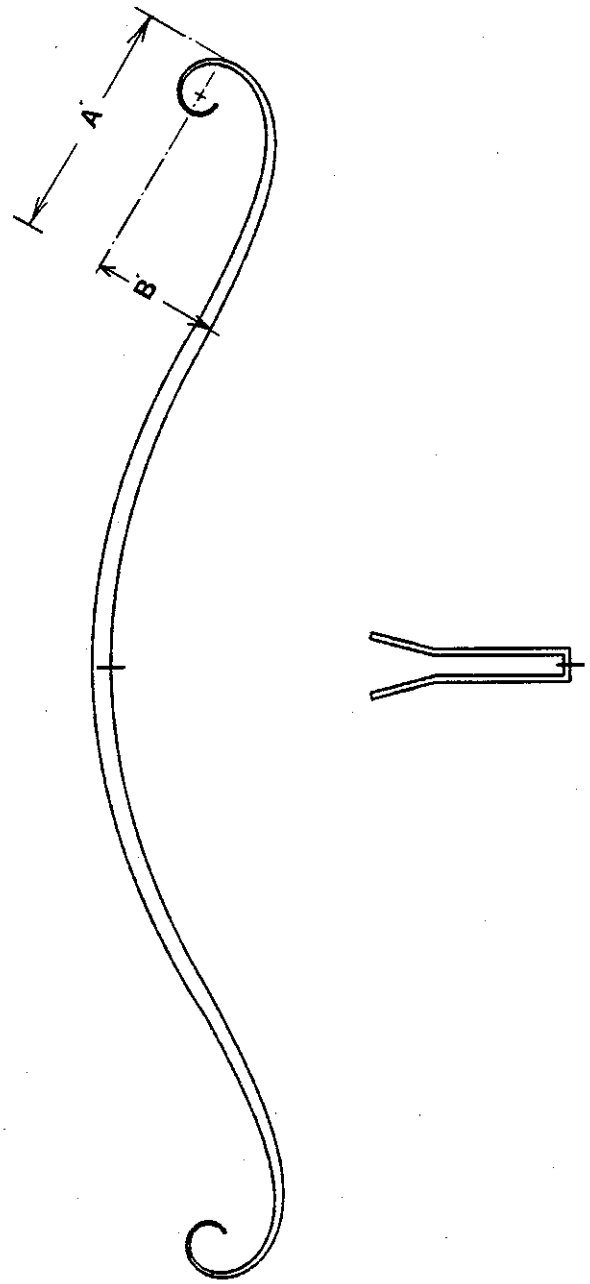

Fig.-4.9 Spiral aperture-matched cylindrical parabolic reflector with the spiral having dimensions A', and B'.

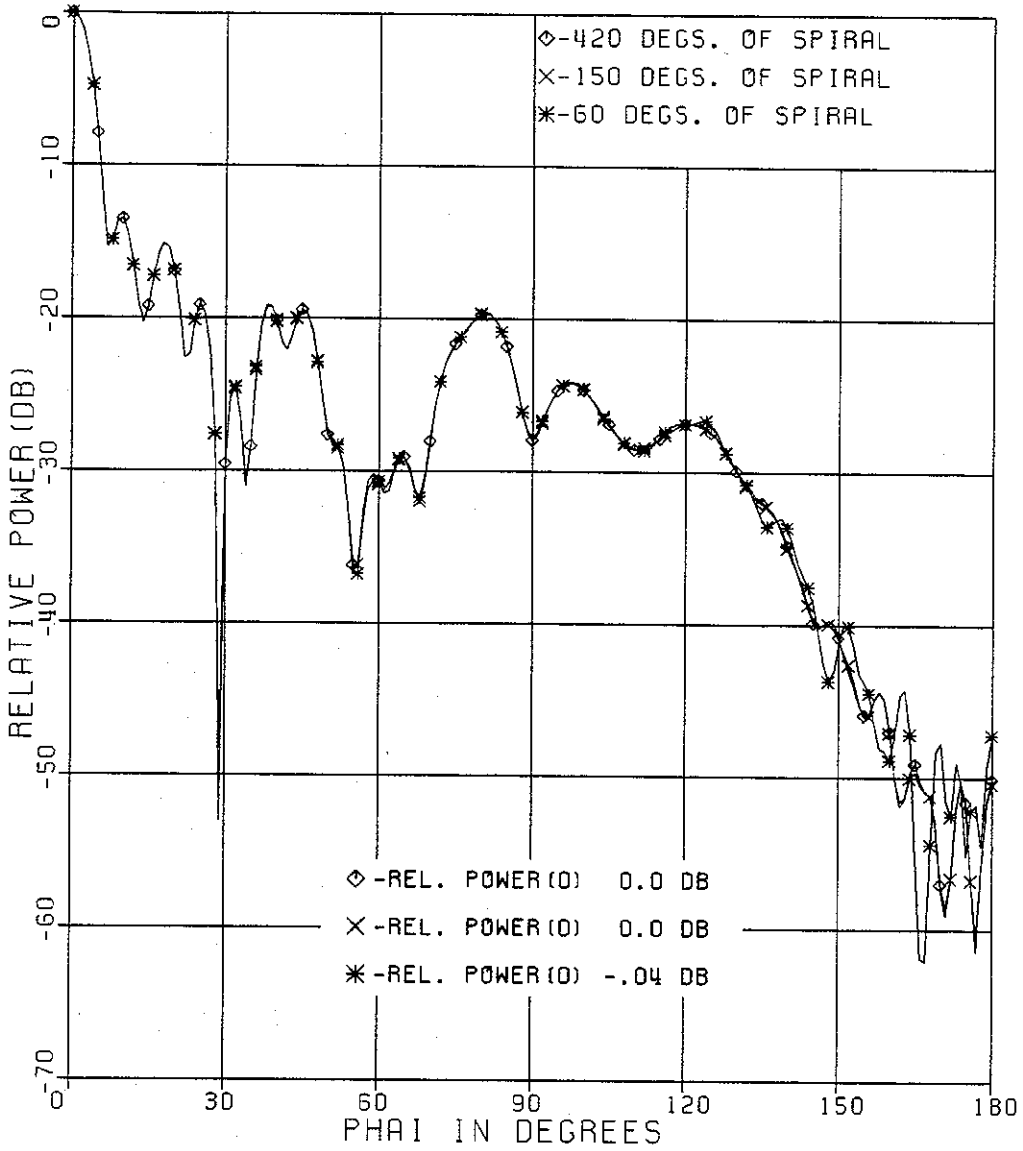

Fig.-4.10 E-plane radiation patterns of spiral matched cylindrical parabolic reflectors with different spiral flange lengths, for $D = 10\lambda$, $f/D = .433$, and $A' = 4\lambda$ $B' = A'/2$.

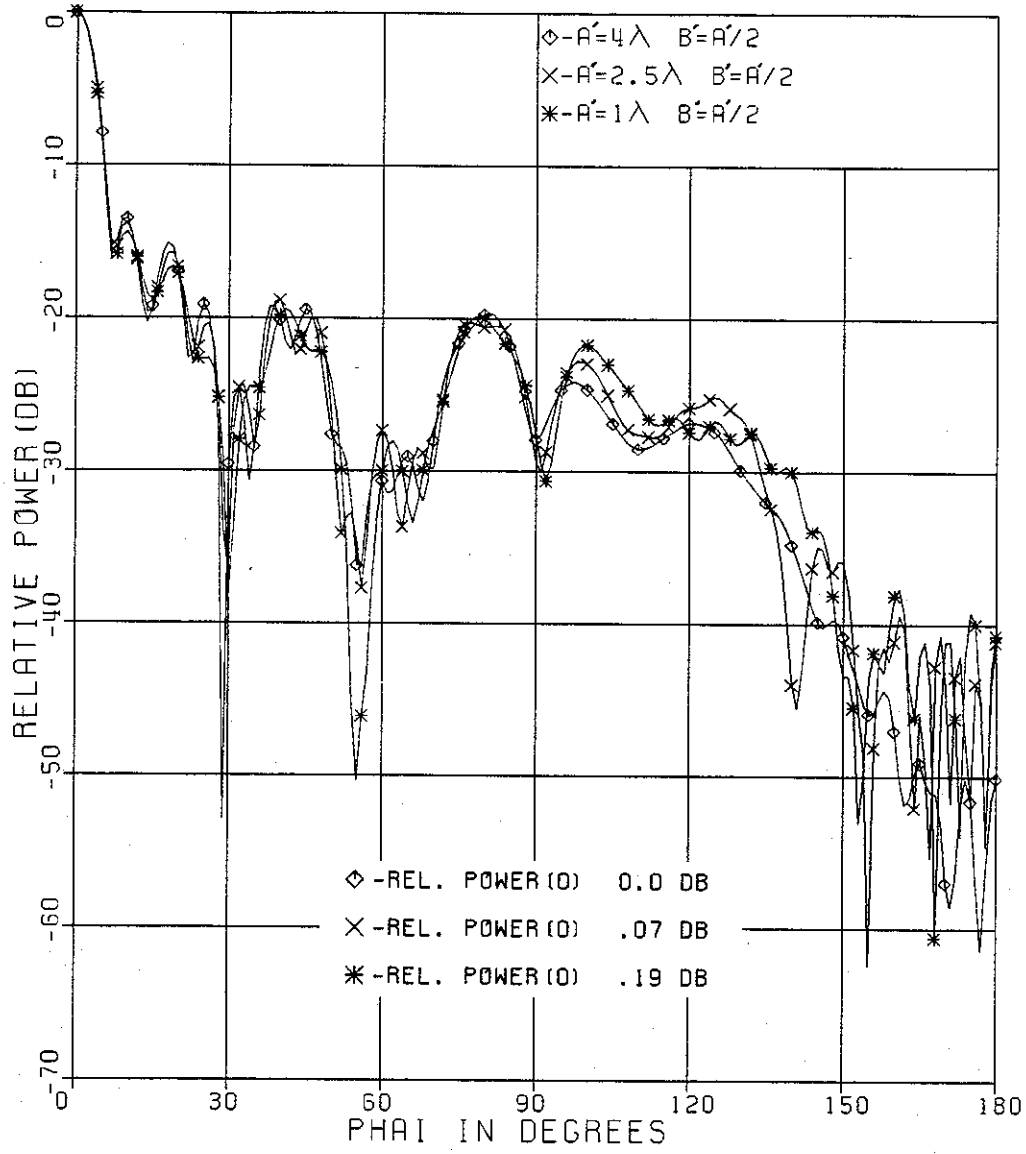

Fig.-4.11 E-plane radiation patterns of spiral matched cylindrical parabolic reflectors with different spiral flange sizes, for $D = 10\lambda$, $f/D = .433$.

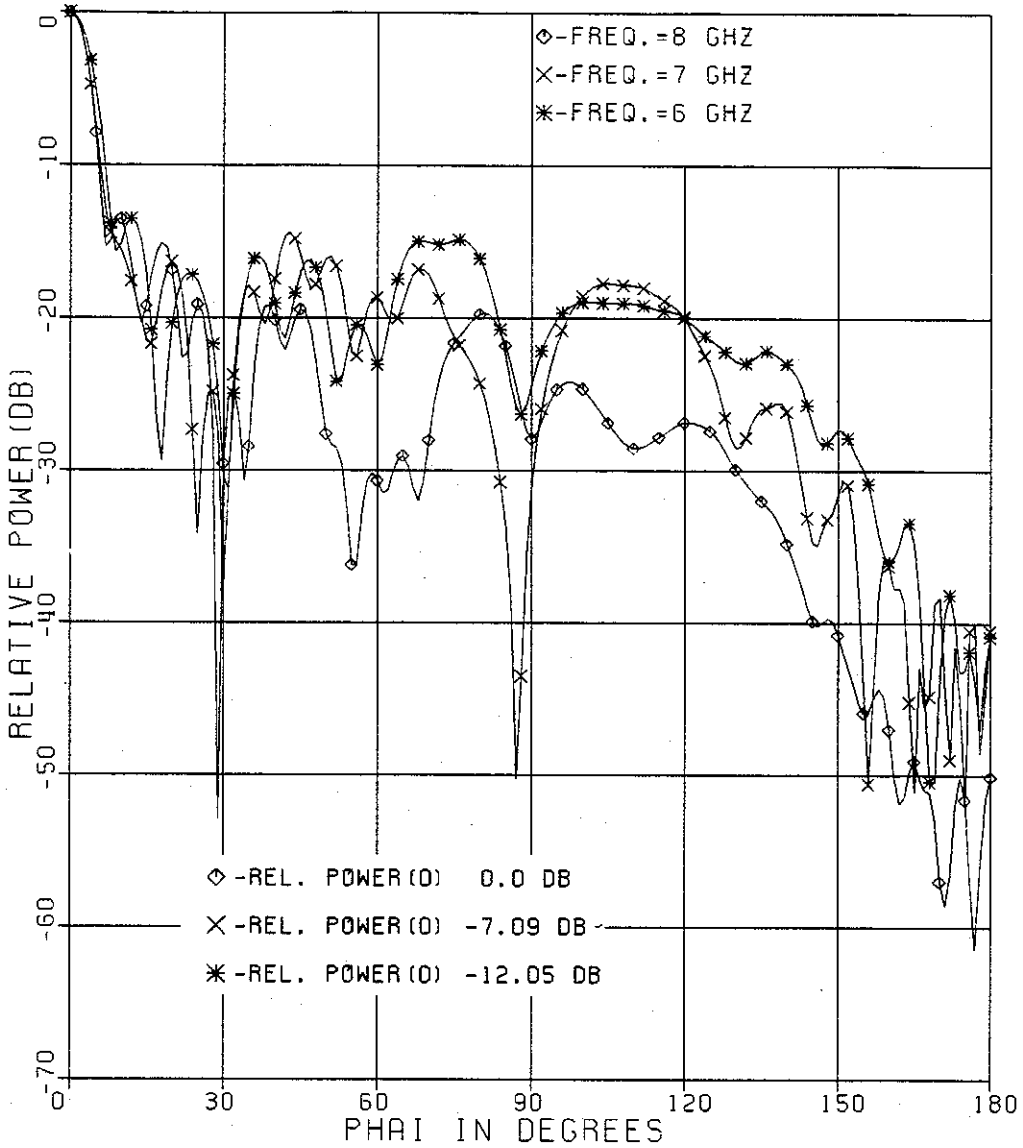

Fig.-4.12 E-plane radiation patterns of spiral matched cylindrical parabolic reflectors at different frequencies, with $D=10\lambda$, $f/D=.433$, and $A'=4\lambda$ $B'=A'/2$ at F=8 GHZ.

Fig.-4.13 shows field patterns of a spiral and ellipse matched reflector, with their matching flanges having almost similar electrical sizes. It is observed in these plots that there is no major change in the $\phi=0^o$ to 90^o field pattern levels, which is attributed to the blockage of the feed horn on the secondary pattern of the antenna.

4.3 Aperture-Matched Offset Parabolic Cylindrical Reflectors.

In this section both ellipse and spiral aperture matching of reflectors are implemented. The blockage of the feed horn is avoided by using an offset parabolic cylindrical reflector. The reflector is chosen to have a diameter D of 20λ and f/D ratio of .433 and subtended by an angle of 120^o when viewed from the focus. The reflector section chosen for the offset part is that whose edges are subtended by an angle of 40^o (20^o to 60^o) when viewed from the focus, with the aperture size L' equal to 7λ as shown in Fig.-4.14.

The feed horn, whose phase center is located as close as possible to the focus of the reflector, is tilted by an angle of 40^o so that the peak of the feed horn pattern is located at the center of the reflector surface. The feed horn whose pattern is shown in Fig.-4.15 illuminates the reflector with a 7dB taper.

Fig.-4.16 shows computed field patterns of an unmatched reflector and an ellipse matched offset reflector shown in Fig.-4.14a, for cases $A=2.8\lambda$, $B=1.4\lambda$ and $A=1.4\lambda$, $B=0.7\lambda$, respectively. As before, a significant decrease in the back lobe and far side lobe levels is achieved for ellipse matching.

To reduce the blockage of the horn caused by the addition of the elliptic flange, a smaller size flange is added to the lower edge of the reflector as shown in Fig.-4.14b. The corresponding pattern is computed and is shown in Fig.-4.17 together with the previous ellipse matched cases.

A spiral aperture-matched offset parabolic cylindrical reflector with a feed horn are shown in Fig.-4.18. The spiral flange has $A'=2.8\lambda$ and $B'=1.4\lambda$, where A' and B' have the same definitions as before. The corresponding far field pattern is computed and plotted together with the case of an unmatched reflector in Fig.-4.19. A

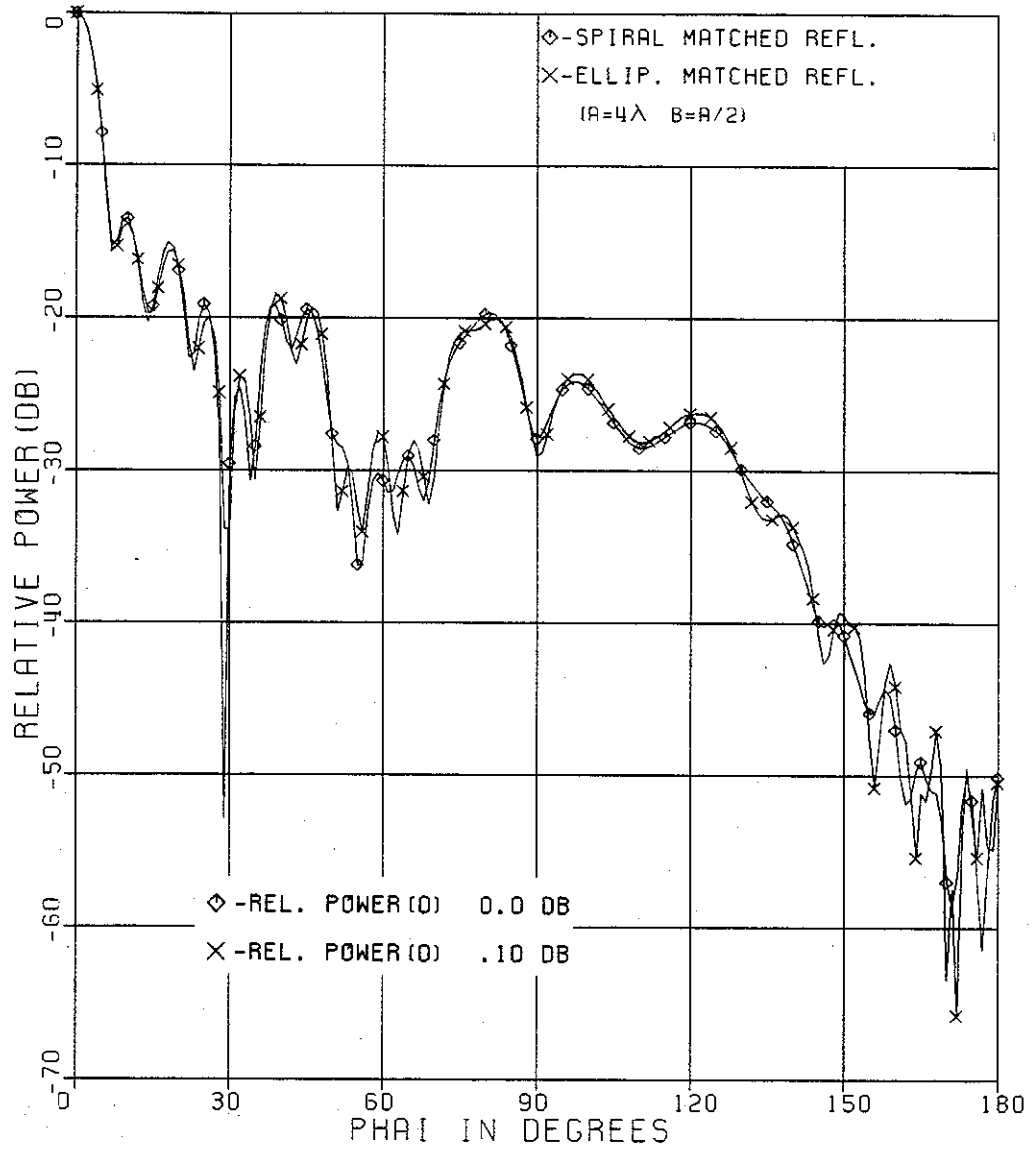

Fig.-4.13 E-plane radiation patterns of spiral and elliptic matched cylindrical parabolic reflectors, for $D = 10\lambda$, $f/D = .433$, and $A = A' = 4\lambda$ $B = B' = 2\lambda$.

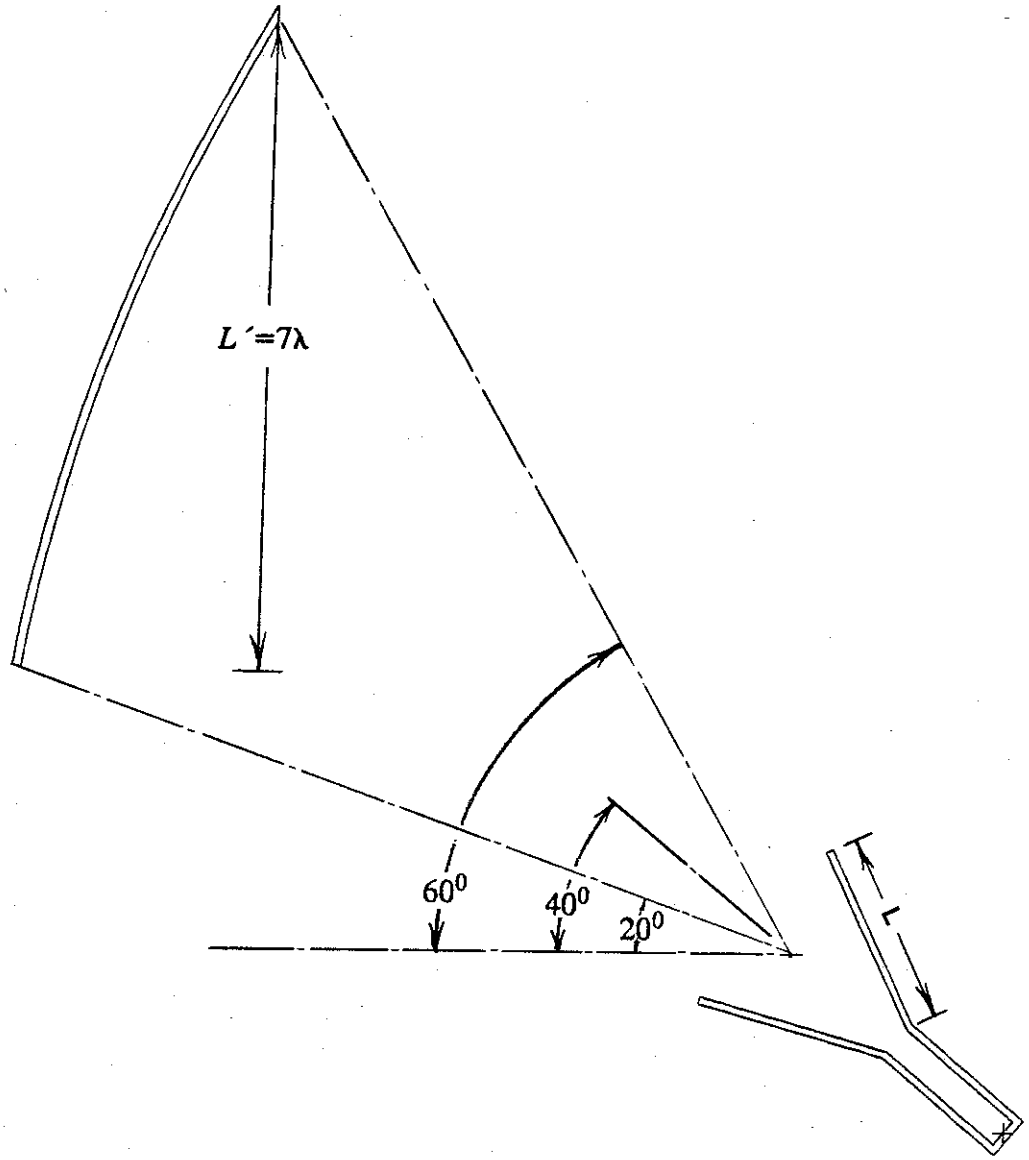

Fig.-4.14 Schematic diagram of the simulated offset cylindrical parabolic reflector with $D = 20\lambda$, $F = .433$, and $L' = 7\lambda$.

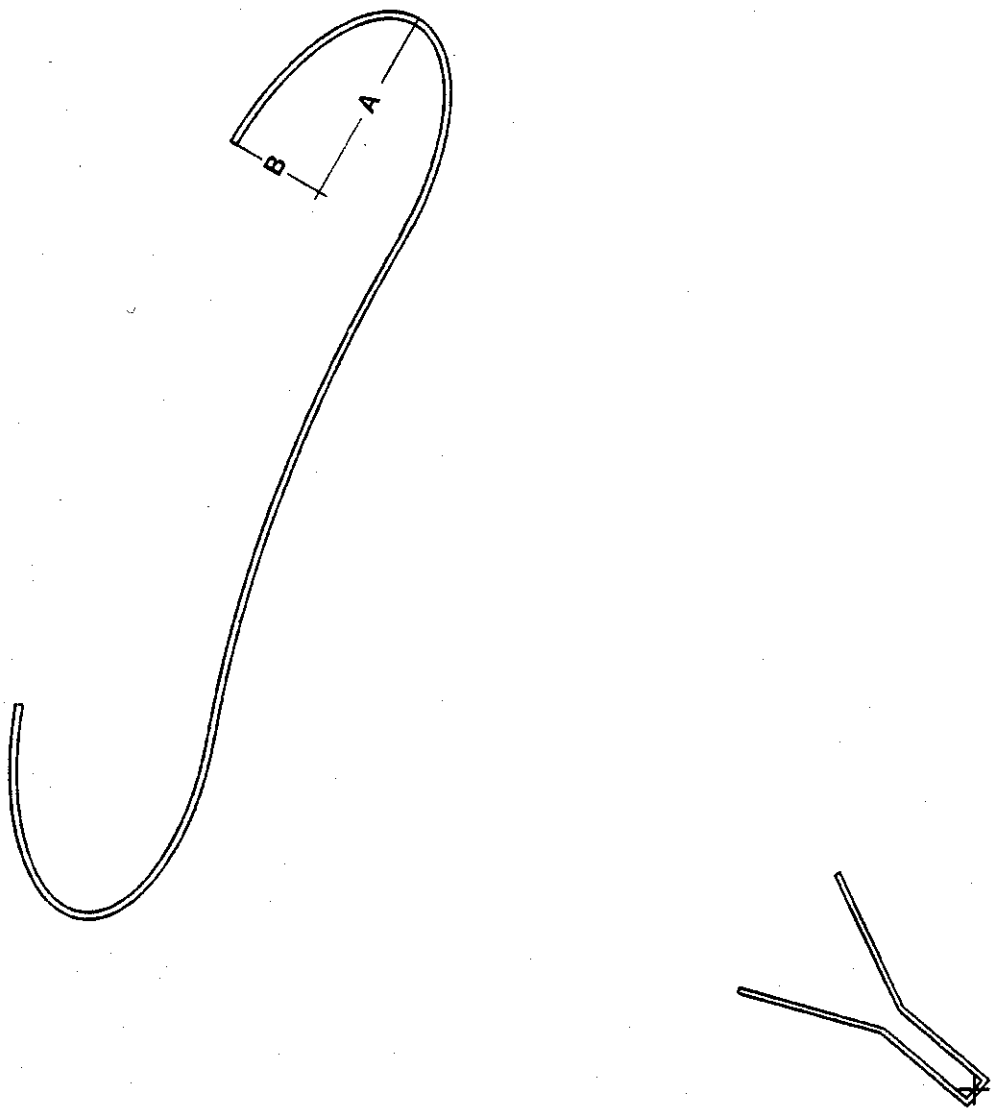

Fig.-4.14a Elliptic aperture-matched offset cylindrical parabolic reflector with the ellipse flange having semimajor axis A, and a semiminor axis B.

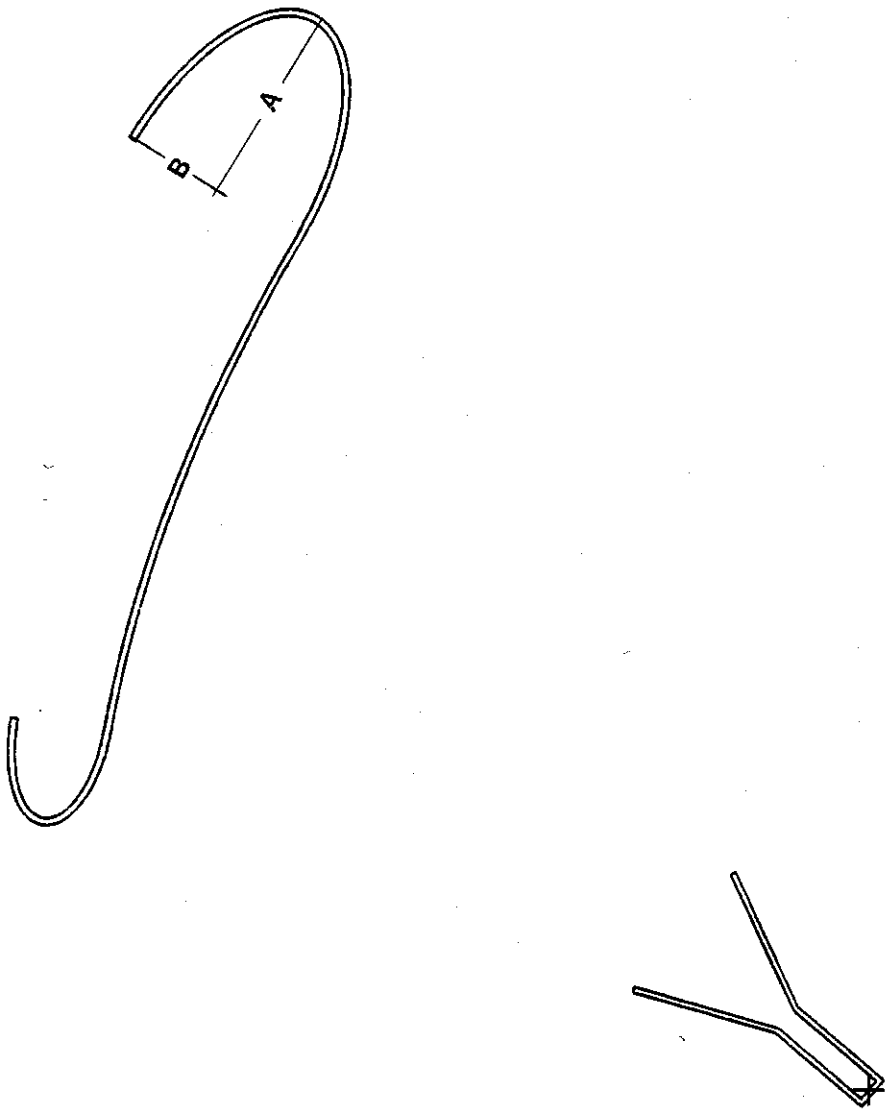

Fig.-4.14b Elliptic aperture-matched offset cylindrical parabolic reflector with different ellipse flanges at each edge.

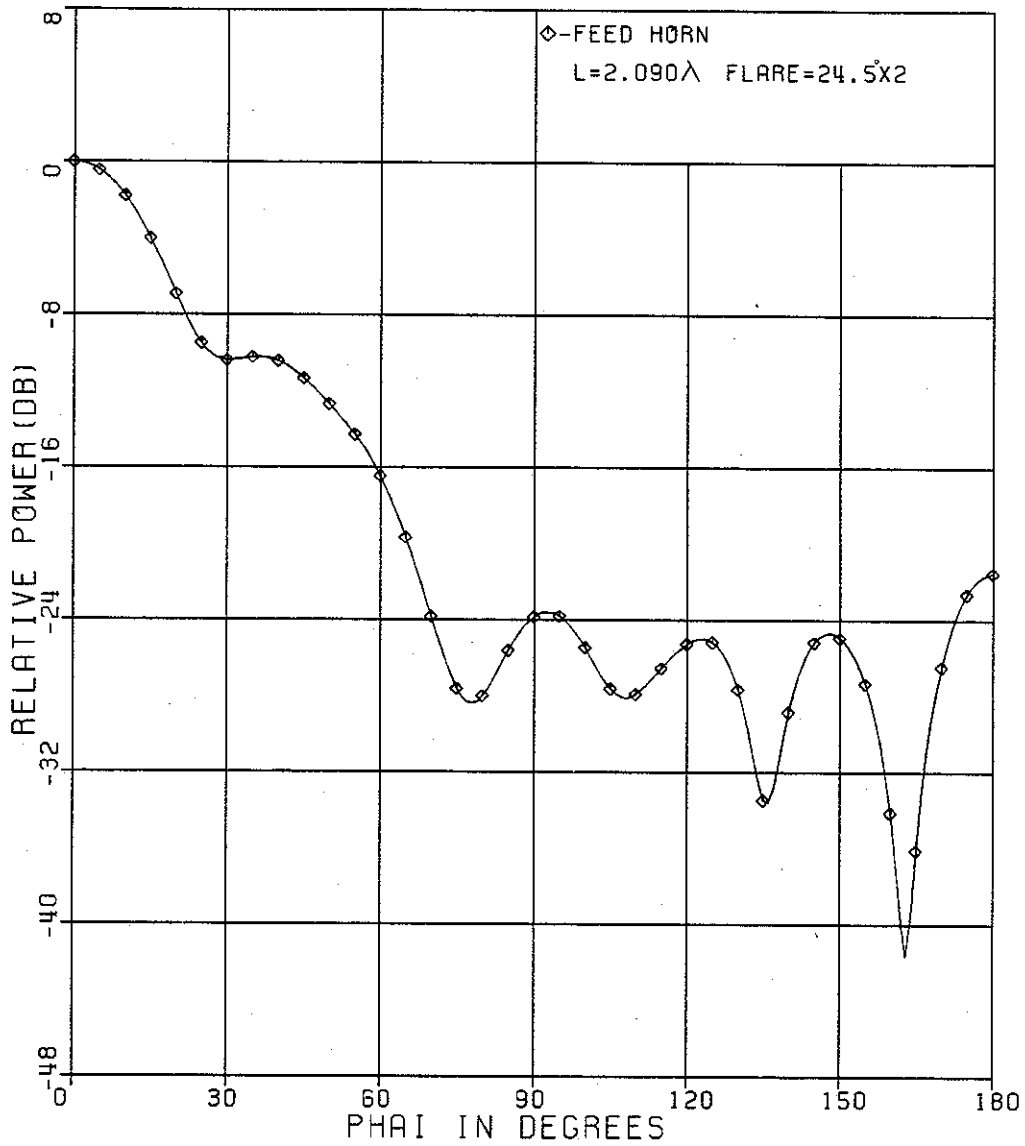

Fig.-4.15 E-plane radiation pattern of the horn used to feed the offset cylindrical parabolic reflector with $7dB$ tapered field.

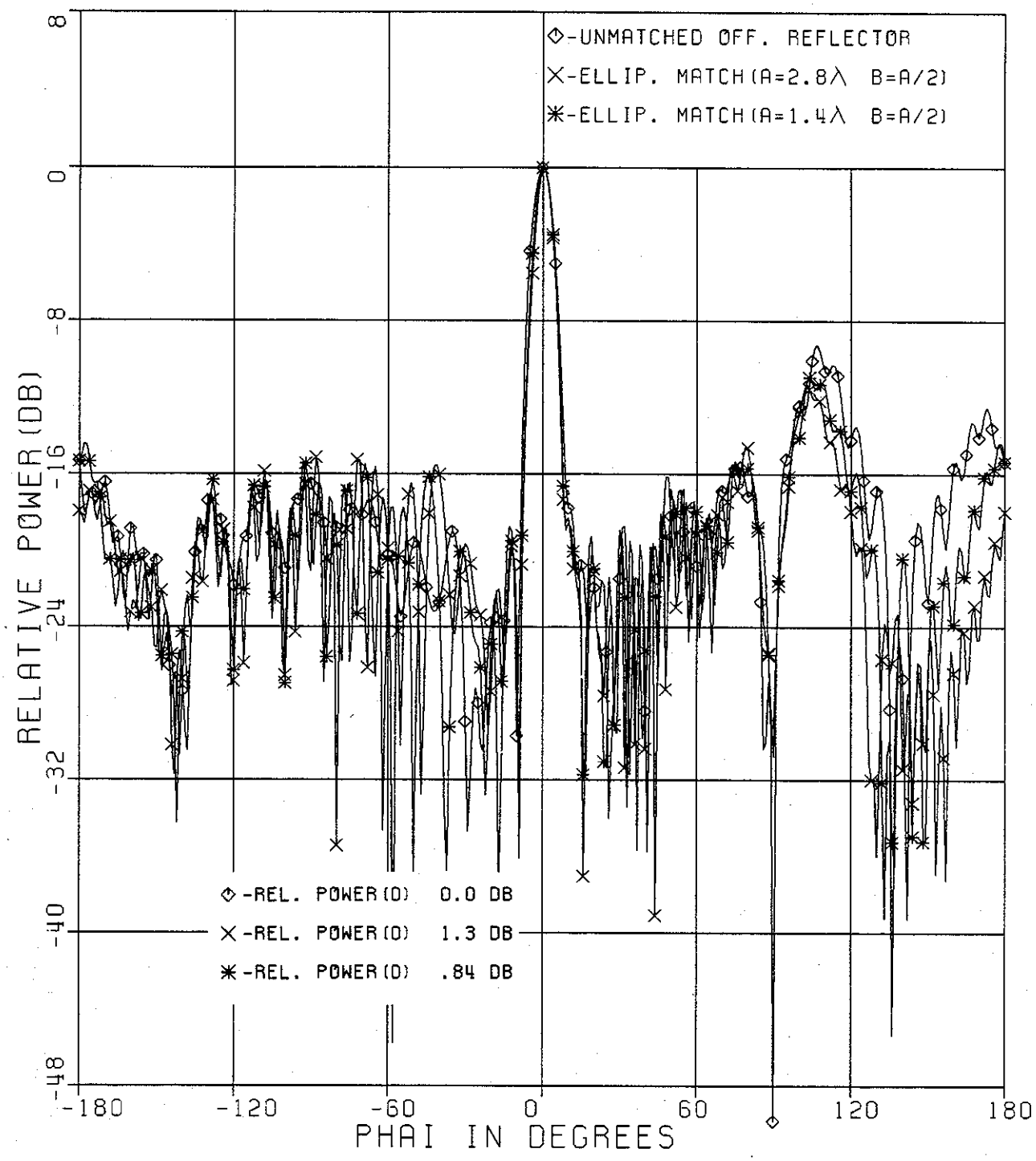

Fig.-4.16 *E*-plane radiation patterns of unmatched and elliptic offset cylindrical parabolic reflectors with different elliptic flange sizes.

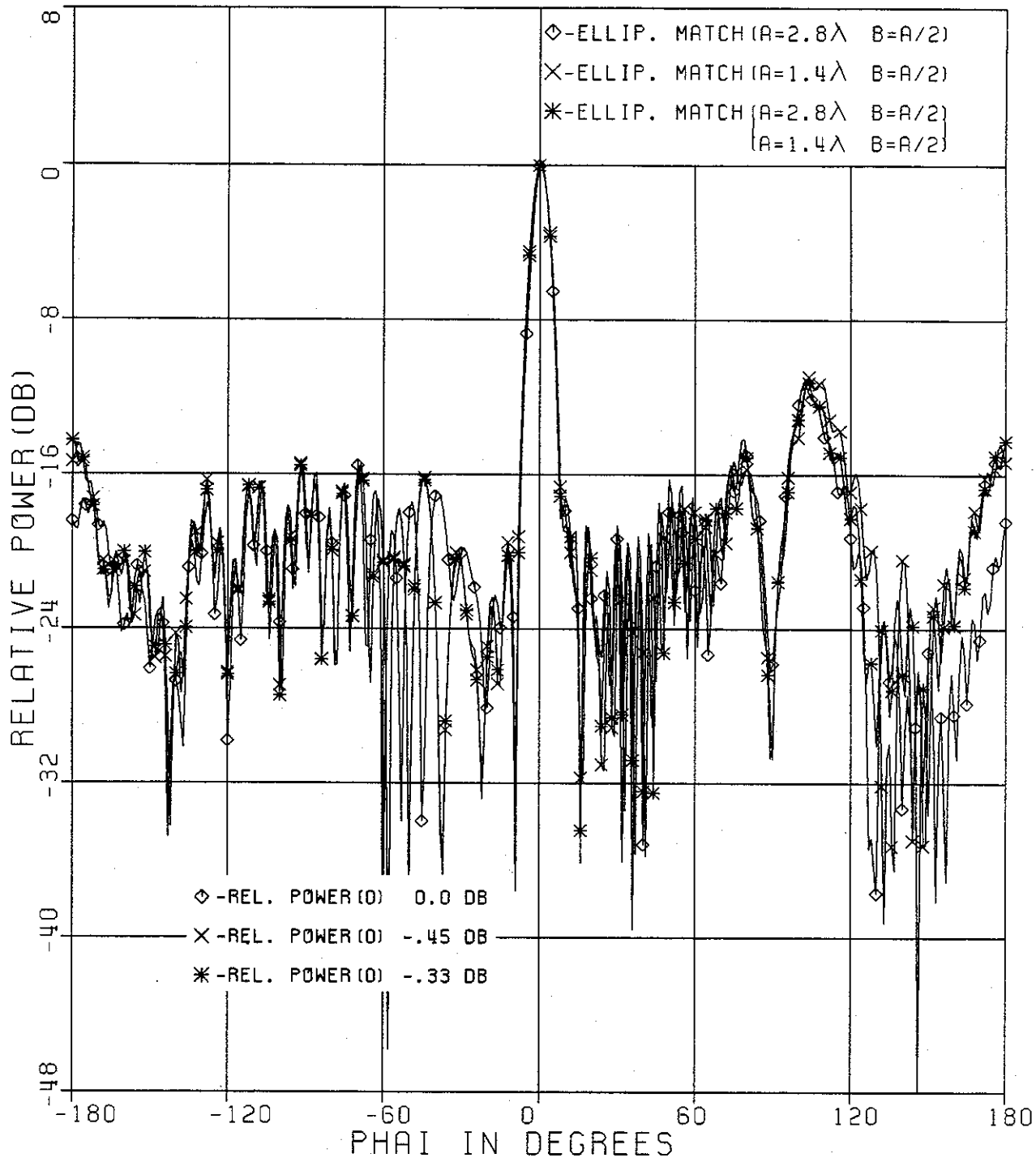

Fig.-4.17 *E*-plane radiation patterns of elliptic matched offset cylindrical parabolic reflectors for different sizes and combinations of the elliptic flanges.

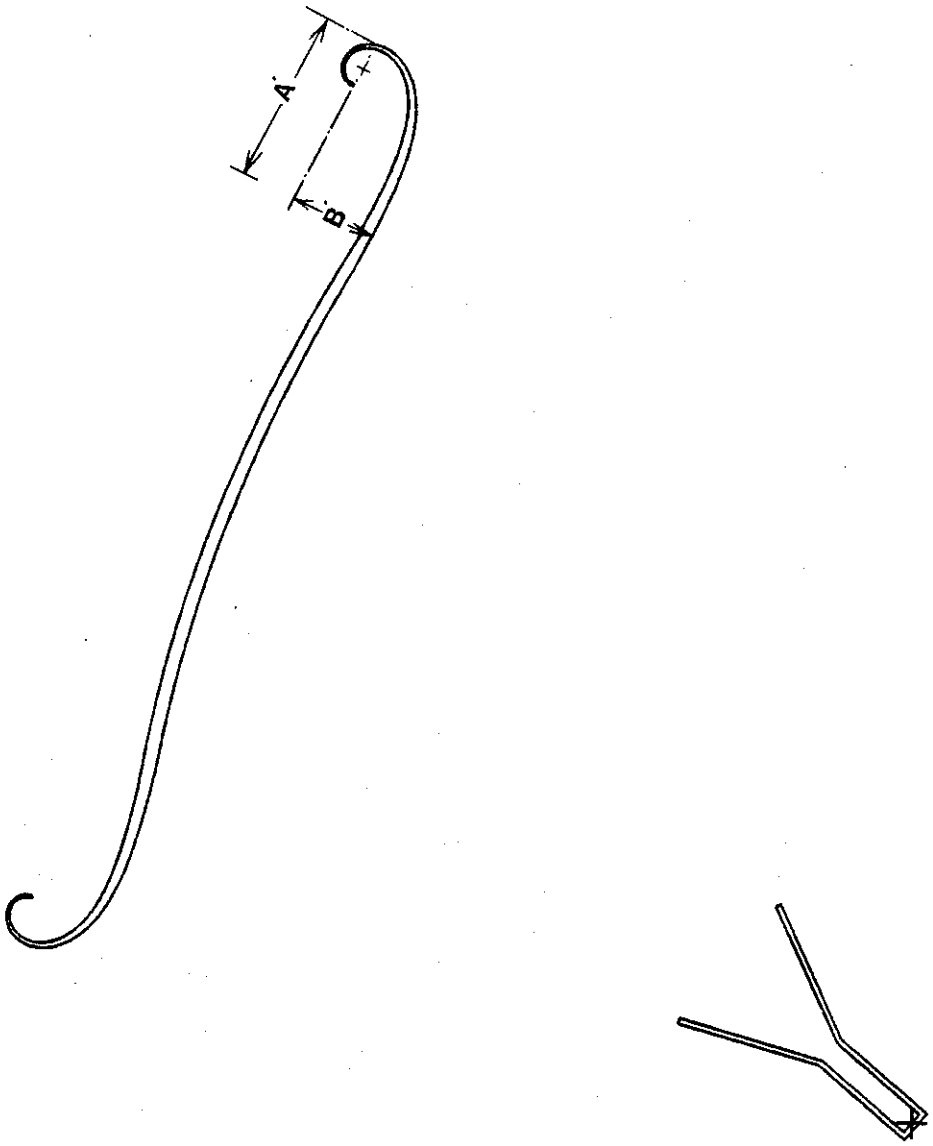

Fig.-4.18 Spiral aperture-matched offset cylindrical parabolic reflector with the spiral flange having dimensions A', and B'.

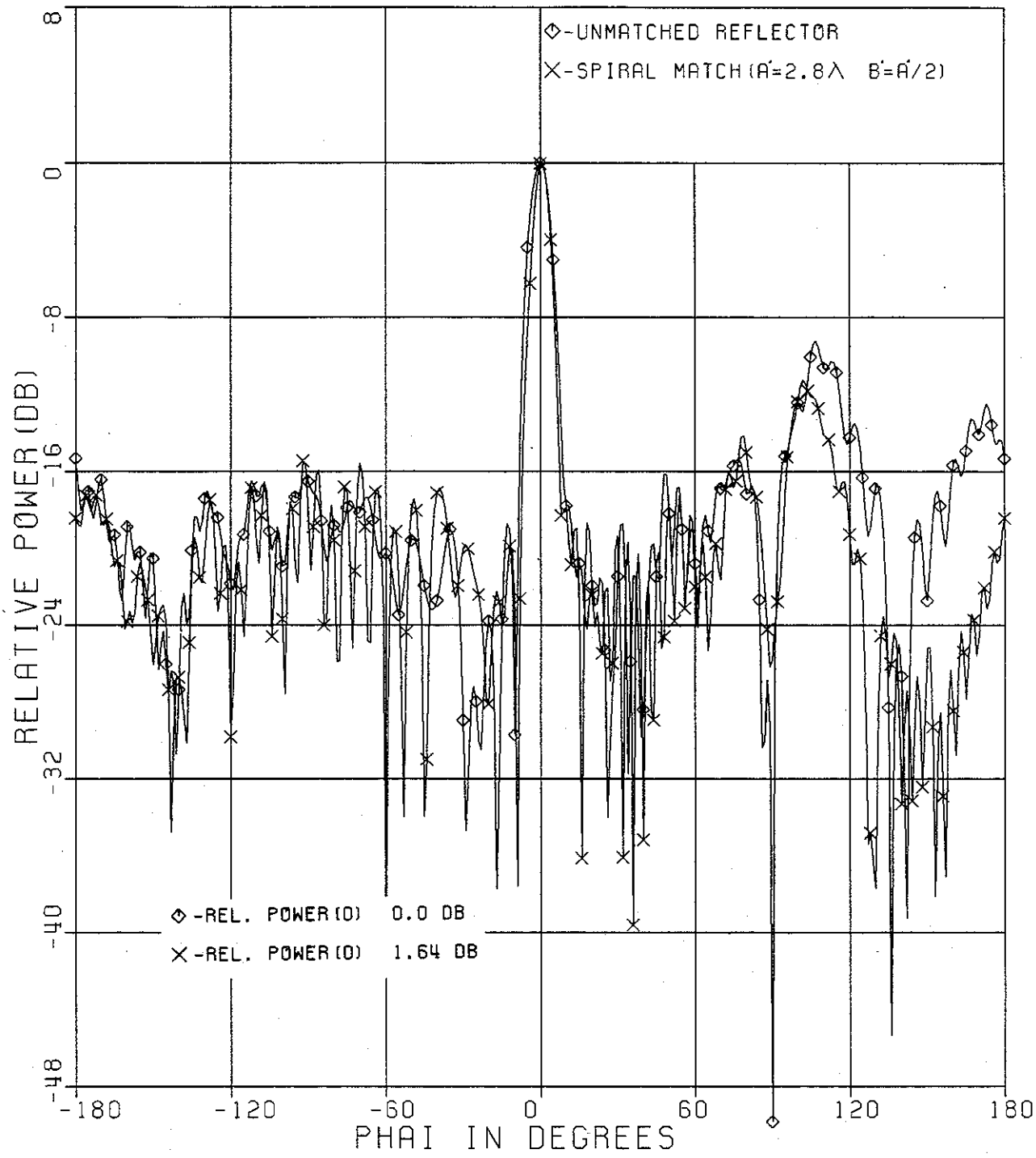

Fig.-4.19 *E*-plane radiation patterns of unmatched and spiral matched offset cylindrical parabolic reflectors.

significant decrease in the back lobes is observed for such aperture matching.

In this section the field patterns of the offset parabolic cylindrical reflector are computed for different types of aperture matching. Elliptical and spiral flanges of different electrical sizes were used, and it was observed that there is a significant back lobe reduction of up to 10dB for an ellipse with $A=2.8\lambda$ and $B=1.4\lambda$. A slightly narrower main lobe pattern is also observed, and this can be attributed to a more uniform field distribution in the aperture of the matched antenna.

4.4 Discussion

Cylindrical reflector radiation patterns are subject to interference by edge diffracted fields in a way similar to horn antennas. Fig.-4.20 illustrates the contribution of the diffracted rays from the reflector edges in addition to the reflected ray at the field point. The way in which the reflector surface is terminated affects significantly the radiation properties of the reflector. The reflected field from the reflector surface abruptly stops at the surface termination and, since electromagnetic fields must be smooth and continuous, a very strong diffracted field will emanate from the terminating edge. Using a single straight edge, the diffracted signals about the edges will be strong because of the direct edge illumination of the edges as shown in Fig.-4.20. As in the horn case, this diffracted signal will interfere constructively and destructively with the signals reflected from the reflector antenna surface. As illustrated before in section 3.4, attaching smooth convex shaped flanges at the edges will provide a continuous path for the currents flowing on the reflector surface, and hence the radiation from the matched edge will be directed away from the aperture region of the antenna as shown in Fig.-4.21 [21]. The field pattern plots reported in this chapter show minor changes in the level of the near lobe levels for the matched reflector cases when compared with the unmatched reflector. This is attributed to the fixed feed blockage of the reflector antenna. As in the horn case lower back lobe levels are observed when matching the reflector with electrically large convex shaped flanges.

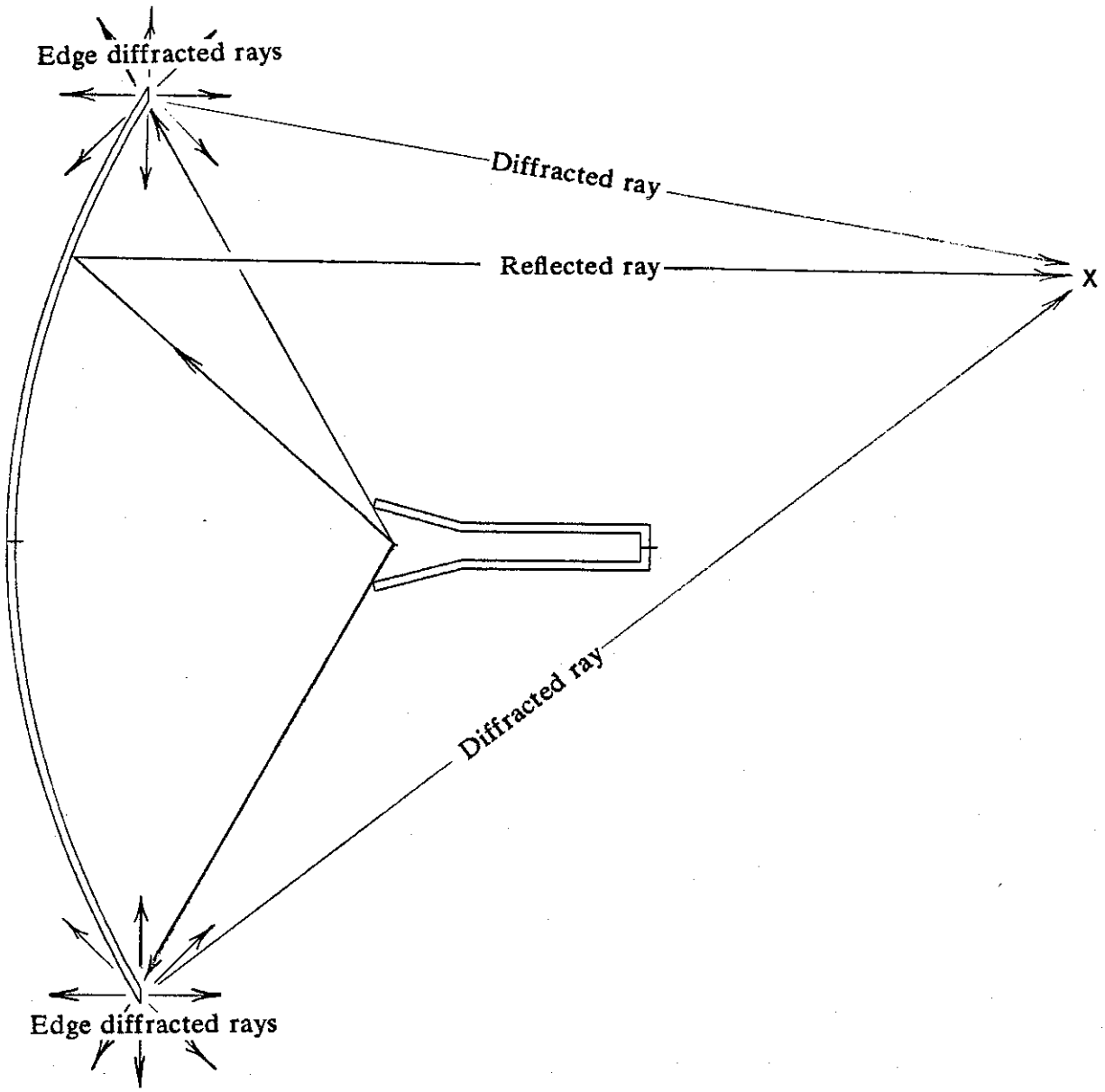

Fig.-4.20 GTD terms for cylindrical parabolic reflector *E* -piane pattern.

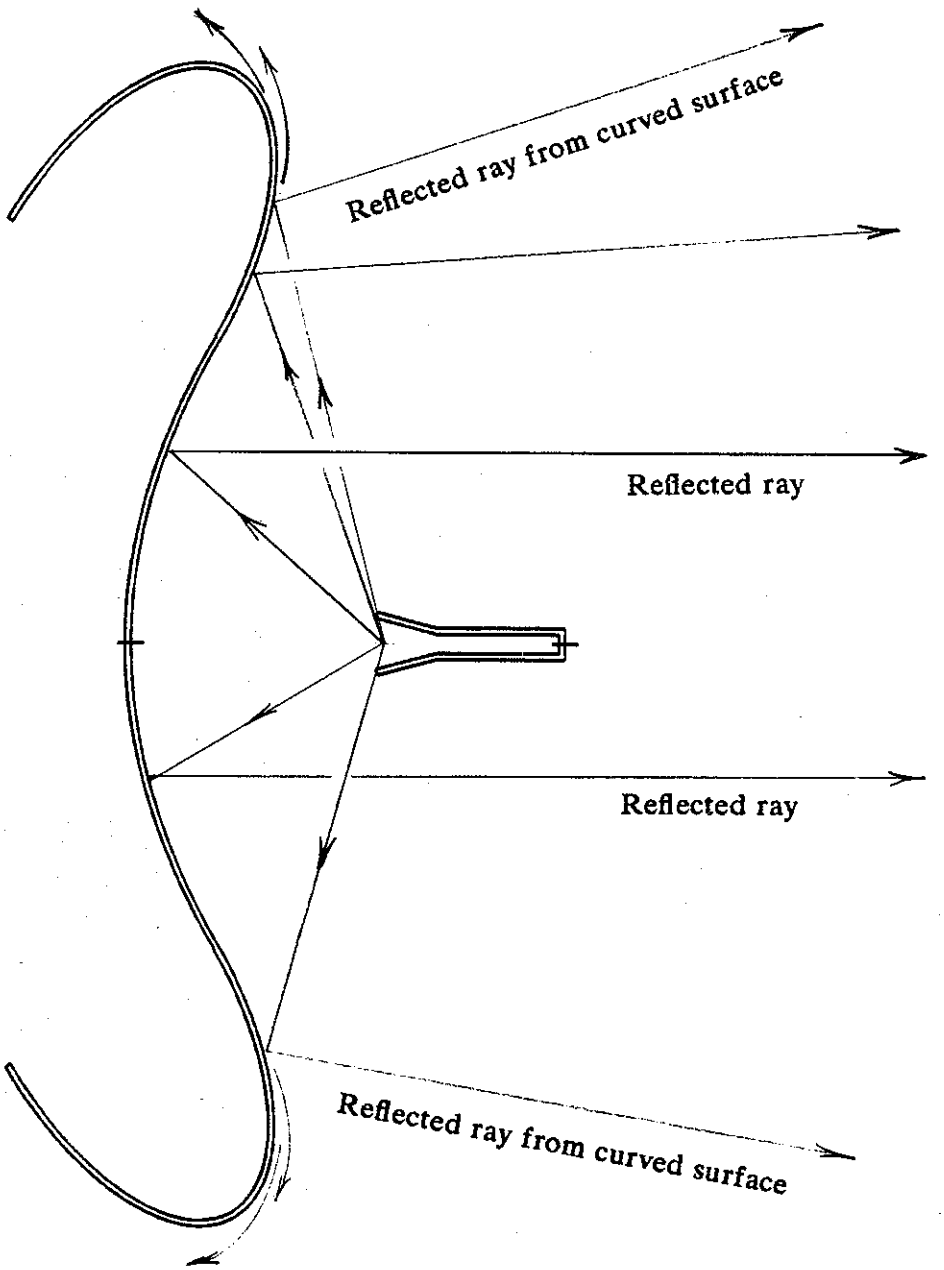

Fig.-4.21 GTD terms for aperture-matched cylindrical parabolic reflector E-plane pattern.

CHAPTER V

Capped-Edge Horn Antennas

5.1 Introduction

In the previous chapters two different approaches of reducing side lobe levels of horn antennas were presented. The first approach which is implemented by the dual and hybrid-mode horns, is based on reducing the magnitude of the incident field to the horn edges, hence reducing the diffracted fields. The second approach is in reducing of the magnitude of the diffraction coefficient at the edges of the horn and is done in the aperture-matched horns. In this chapter an alternative approach is followed for reducing the side lobe levels of a horn. This approach involves capping the edges of the horn by an appropriate metallic structure, hence shielding the radiation sources that interfere destructively with the fields emitted from the horn aperture. The choice of these structures is such that a proper redirection of the diffracted radiations from the edges is achieved. These structures should also introduce a minimum aperture blockage of the horn antenna. Two types of edge-capped horns are shown in Fig.-5.1 and Fig.-5.2.

5.2 Ellipse Capped-Edges Horn Antennas

In this section a preliminary investigation of the capped-edge horn antenna is reported. Such edge capping involves an elliptic cylinder to shield the edges of the same conventional horn used in the previous analysis.

Firstly, a whole elliptic cylinder having its major axis parallel to the walls of the horn is used for shielding of the horn edges and is separated from the horn walls as shown in Fig.-5.1. The clearance between the elliptic cylinder and the horn walls is introduced to insure that there is no flow of conduction currents in the ellipse structure. Fig.-5.3 shows field patterns of the ellipse capped-edge horn of Fig.-5.1 and the

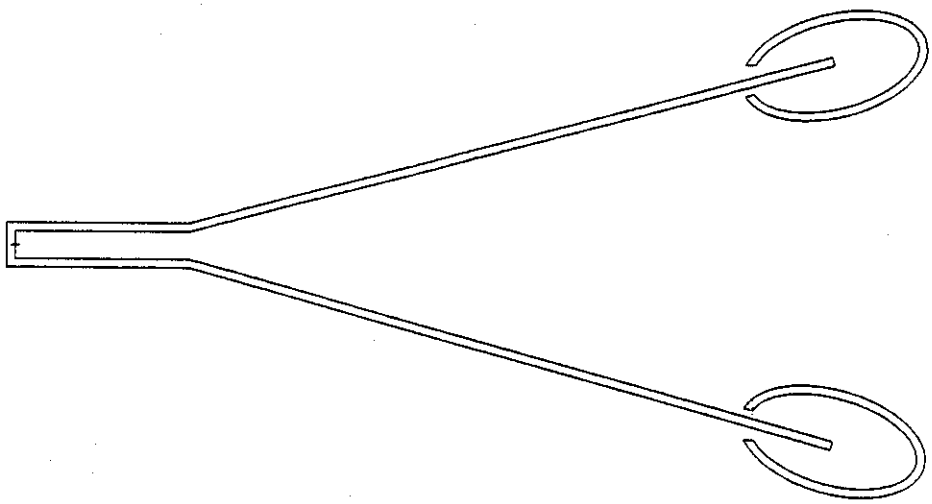

Fig.-5.1 Schematic diagram of the simulated ellipse(whole ellipse) capped-edge horn with the ellipse flange having semimajor axis $A = 1\lambda$, and a semiminor axis $B = 0.5\lambda$.

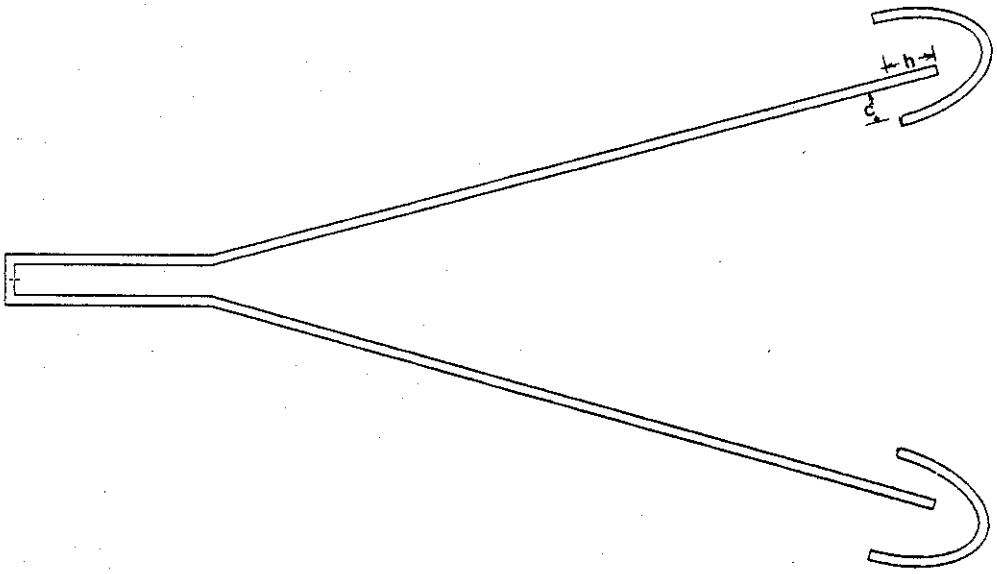

Fig.-5.2 Schematic diagram of the simulated ellipse(half ellipse) capped-edge horn with the ellipse flange having a semimajor axis $A = 1\lambda$, and a semiminor axis $B = 0.5\lambda$ with a clearance c' from the walls of the horn.

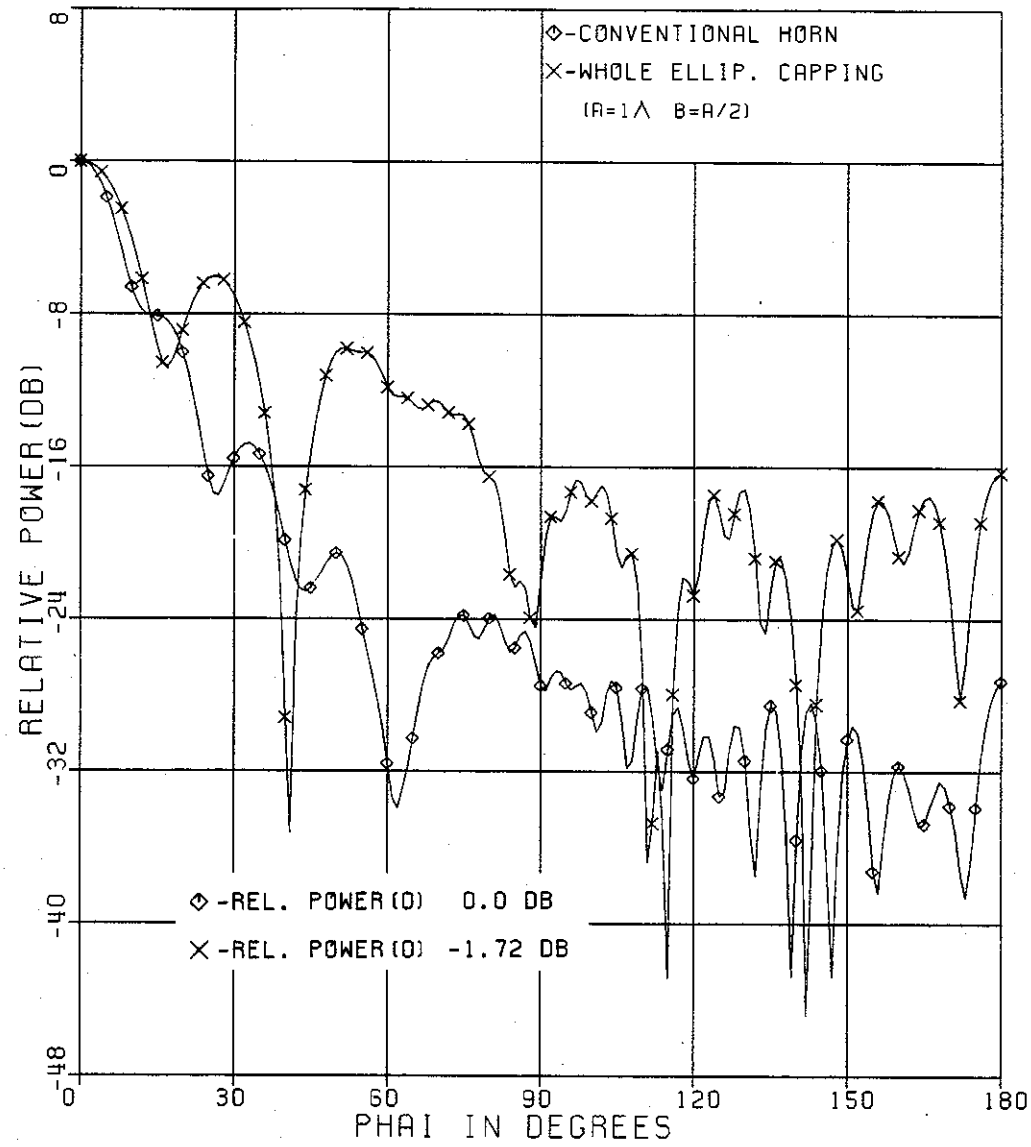

Fig.-5.3 *E*-plane radiation patterns of conventional and ellipse(whole ellipse) capped-edge horns.

conventional horn, with the ellipse having a semimajor axis $A=1\lambda$ and a semiminor axis $B=A/2$. These plots show an increase in the field pattern level of the capped-edge horn compared with the conventional horn which can be attributed to the fact that the problem now is similar to scattering by two elliptic cylinders.

Fig.-5.4 shows field patterns of a capped-edge horn and a conventional horn. The edge capping used in this case is that of Fig.-5.2 where half an elliptic cylinder is used in shielding the horn edges. The ellipse has the same dimensions as before and the major axis is parallel to the walls of the horn. A clearance c' of $.32\lambda$ between the horn walls and the inner surface of the ellipse, and with the center of the ellipse located at a distance $h=\lambda/2$ from the line matching with the edge of the horn is used and shown in Fig.-5.2. These field patterns show a little decrease in the near lobe levels of the capped-edge horn compared with the conventional horn, and show also a large increase in the far lobe levels since now the shielding part of the ellipse inside the horn acts as a waveguide for the fields incident from the throat of the horn where they are redirected to the far lobe region. Fig.-5.5 shows the field patterns of a capped-edge horn of Fig.-5.2 with clearance $c'=0.05\lambda$ and the conventional horn, where a significant decrease in the side lobe level is observed for the capped-edge horn in the $\phi=65^o$ to $\phi=130^o$ and a minor increase in the back lobe region. This is because the clearance c' is small enough to prevent the propagation of the fields incident from the throat region of the horn inside the ellipse structure. Fig.-5.6 shows field patterns of the capped-edge horn of Fig.-5.2 with $c=0.1\lambda$ and $h=0.25\lambda$ together with the conventional horn. Fig.-5.7 shows far field radiation patterns of the same edge-capped horn for a clearance c' of 0.1λ and different values of h equal to $1/2\lambda$, $1/4\lambda$, and 0λ, respectively.

The increase in the RPE level in the far lobe region of the half ellipse capped-edge horns of the cases shown in figures 5.5 and 5.6, can be attributed to the strong diffracted fields at the ellipse edges inside the horn being redirected in the form of surface currents on the outer surface of the elliptic cylinder, hence radiating in the far lobe region of the horn. To avoid such radiations, the concept of shielding is applied now in a different form as shown in Fig.-5.8. A slightly electrically larger

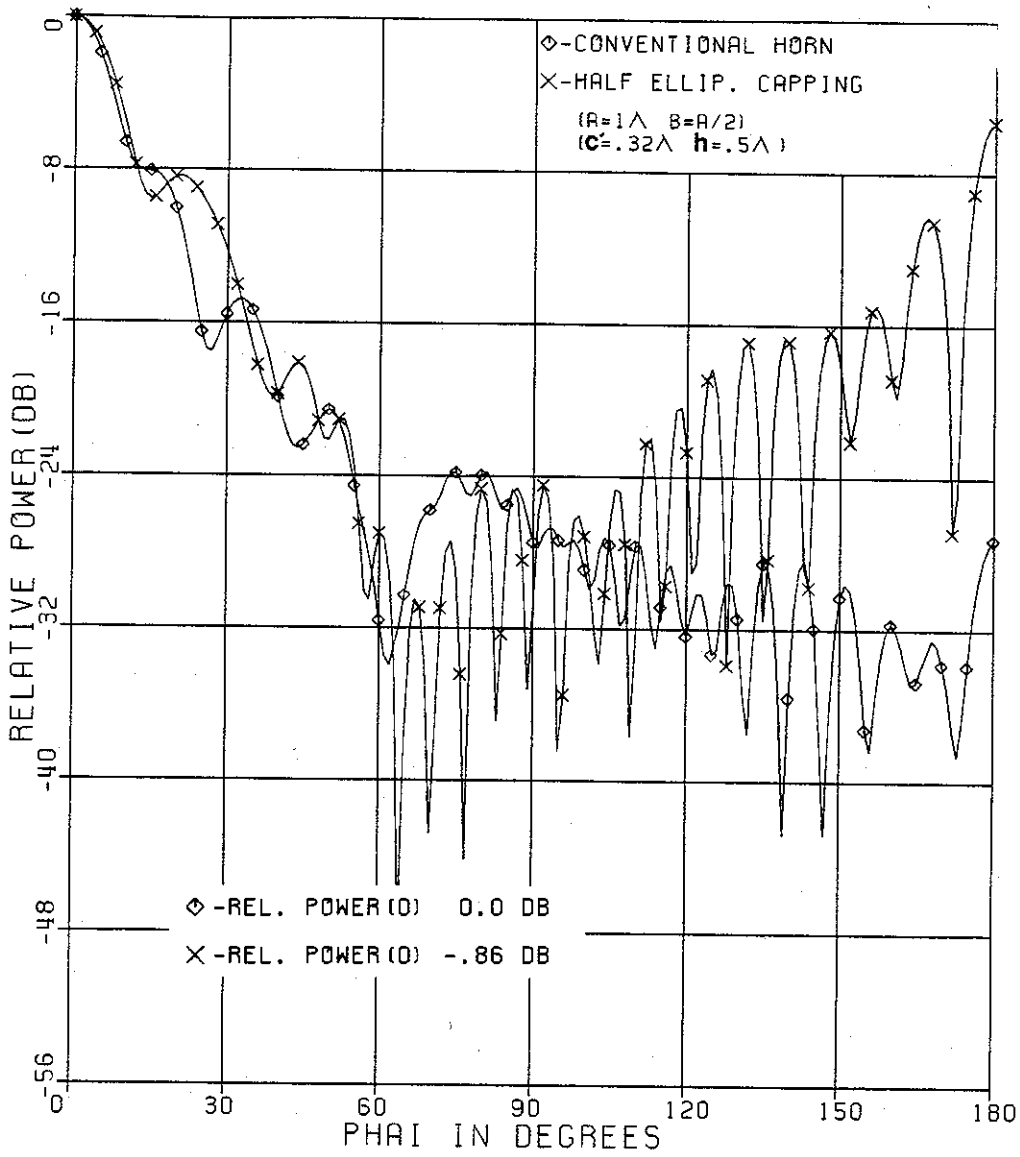

Fig.-5.4 E-plane radiation patterns of conventional and ellipse(half ellipse) capped-edge horns, for $A = 1\lambda$, $B = A/2$, $c' = 0.32\lambda$, and $h = 0.5\lambda$.

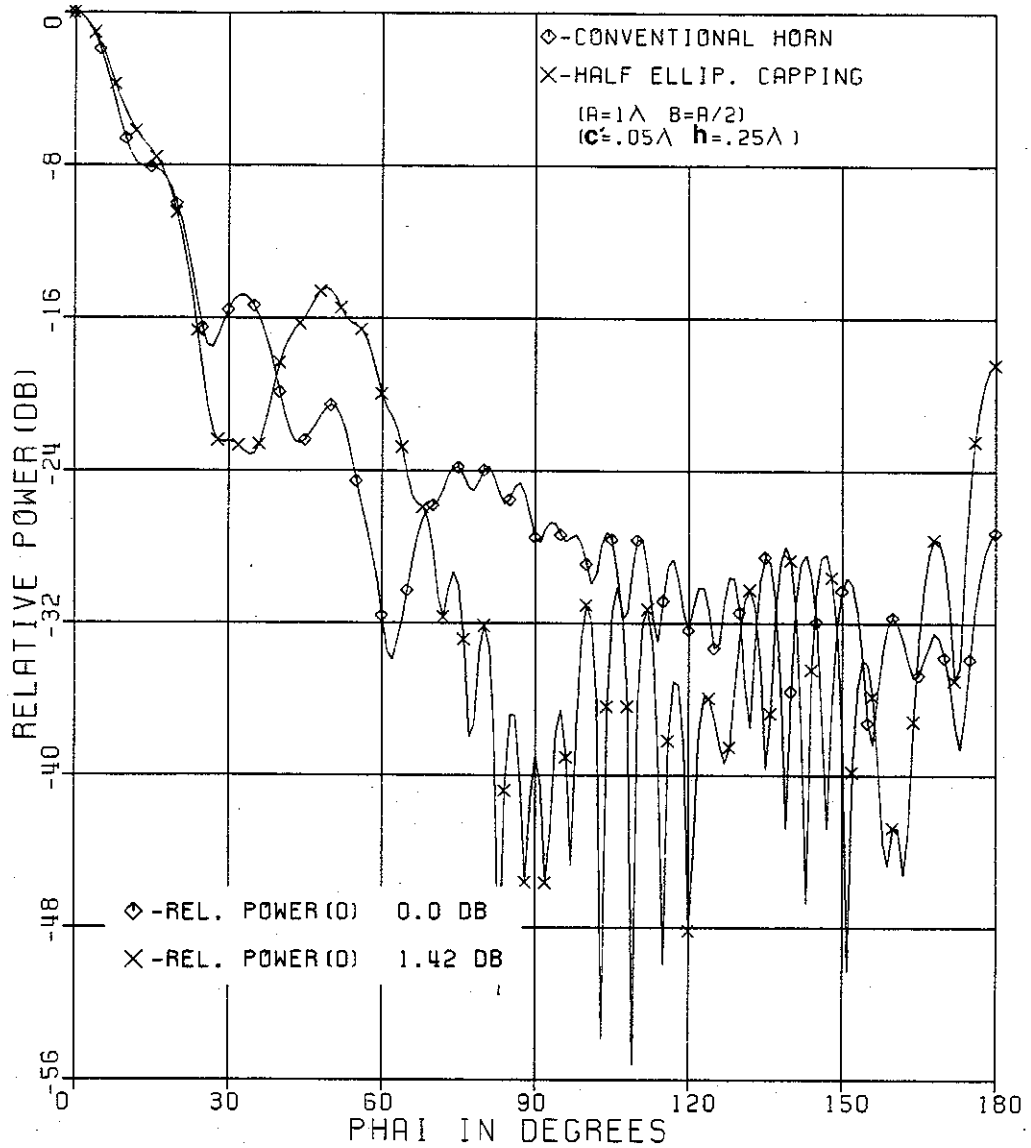

Fig.-5.5 E-plane radiation patterns of conventional and ellipse(half ellipse) capped-edge horns, for $A = 1\lambda$, $B = A/2$, $c' = 0.05\lambda$, and $h = 0.25\lambda$.

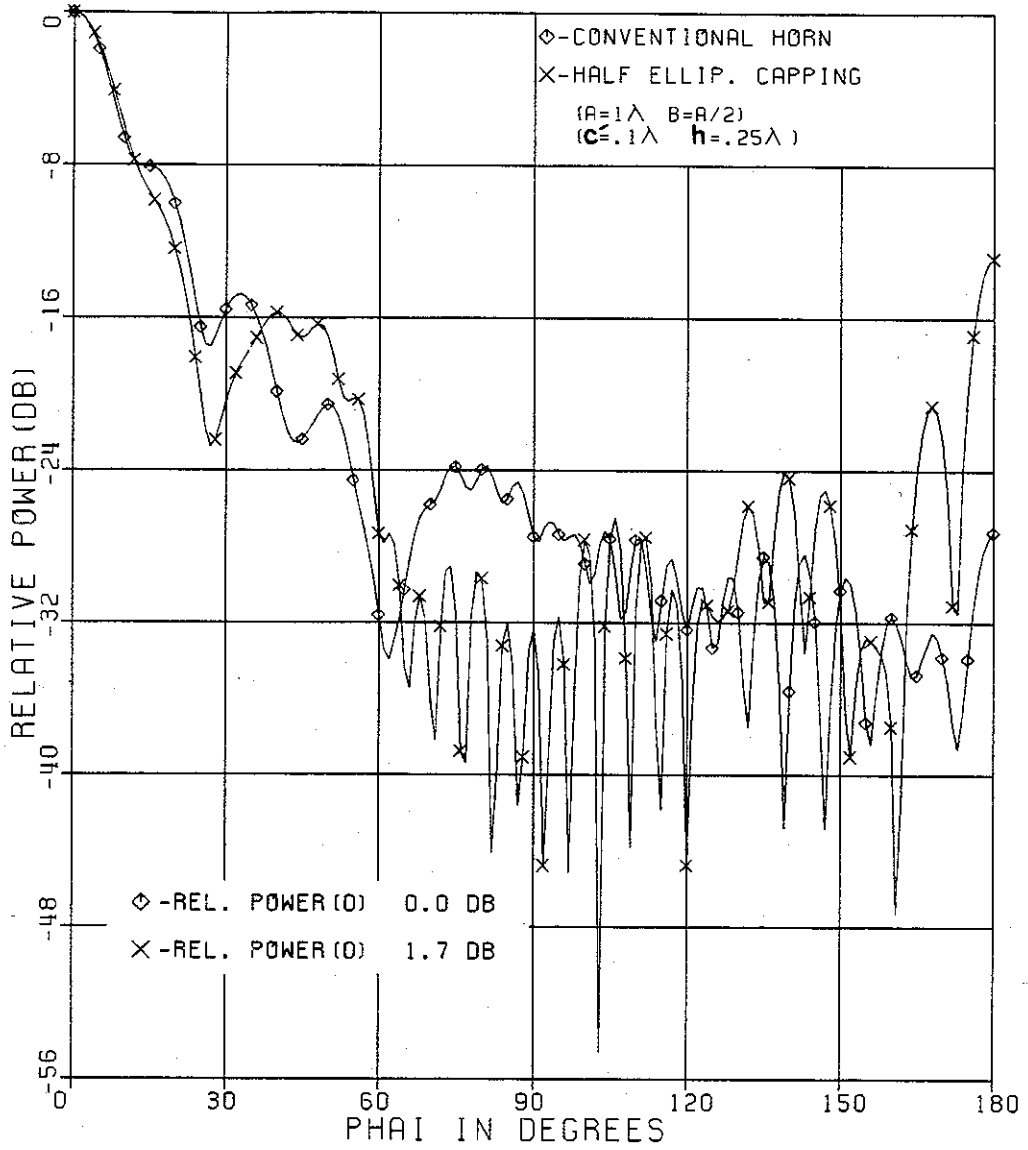

Fig.-5.6 *E*-plane radiation patterns of conventional and ellipse(half ellipse) capped-edge horns, for $A = 1\lambda$, $B = A/2$, $c' = 0.1\lambda$, and $h = 0.25\lambda$.

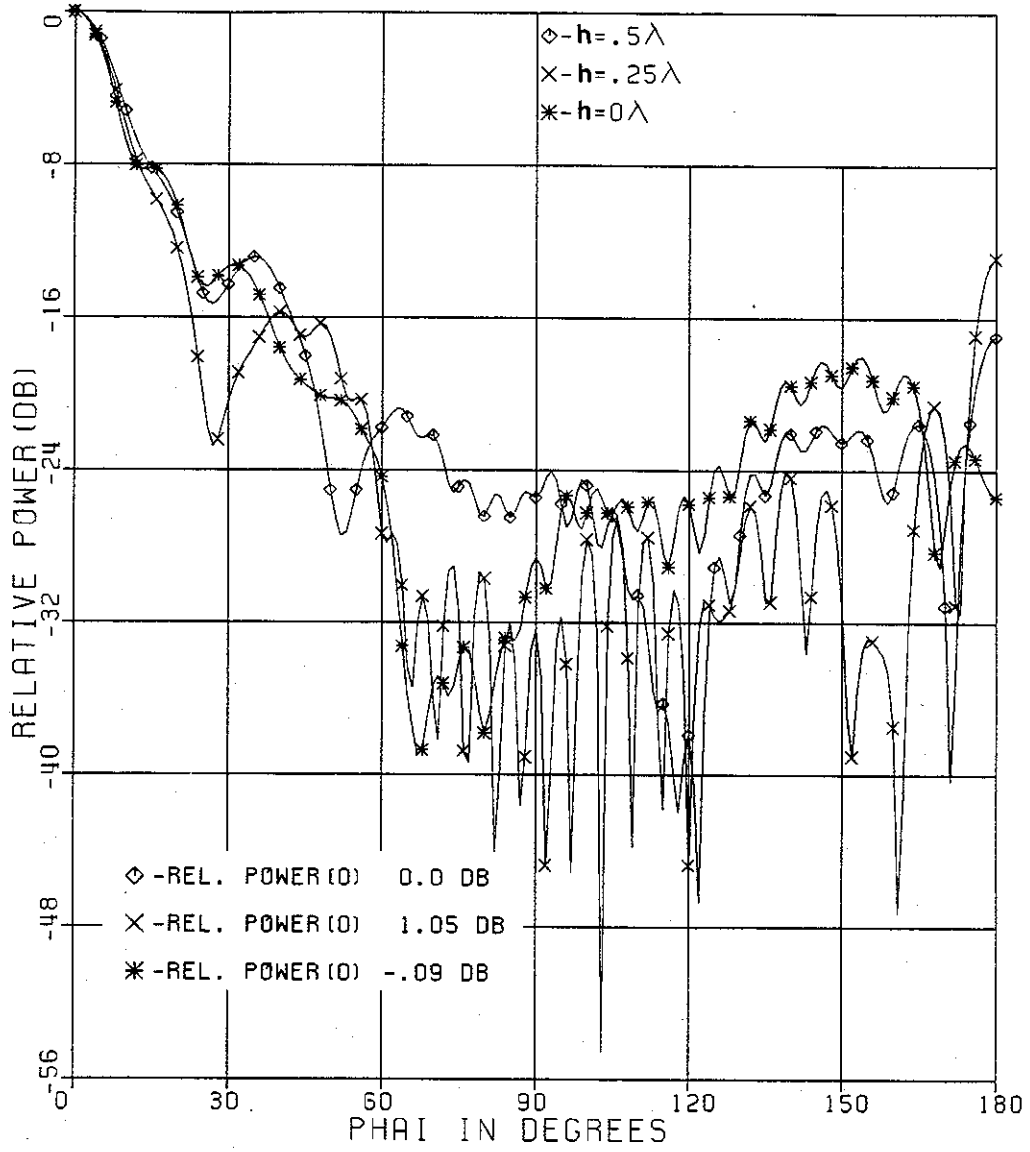

Fig.-5.7 *E*-plane radiation patterns of ellipse(half ellipse) capped-edge horns, for $A = 1\lambda$, $B = A/2$, $c' = 0.1\lambda$.

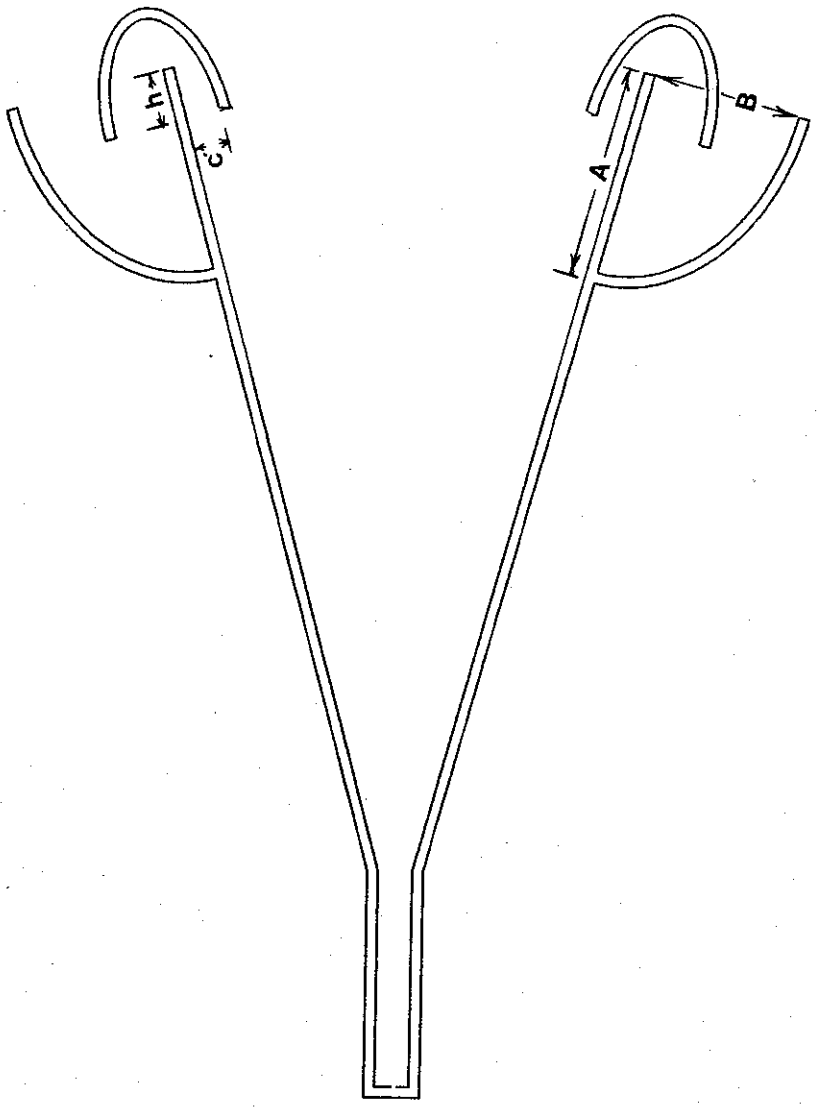

Fig.-5.8 Schematic diagram of a double ellipse capped-edge horn with clearance c', distance h, and the outer capping ellipse having double the dimensions of the inner capping ellipse.

half elliptic flange is used to shield the outer part of the elliptic flange used in capping the horn edges. This elliptic cylinder has its center located at the edge of the horn with its semimajor axis A lying on the flared walls of the horn and its semiminor axis B perpendicular to the flared walls of the horn as shown in Fig.-5.8. The radiation pattern of such double ellipse capped-edge horn is computed for $c' = .1\lambda$, and $h = .25\lambda$ and is shown in Fig.-5.9 together with the field pattern of our conventional horn. Fig.-5.10 shows field radiation patterns of the double ellipse capped-edge horn with $c' = .05\lambda$ $h = .25\lambda$, compared with that of the conventional horn. A significant decrease in the RPE level of up to 20dB is achieved by the double ellipse capped-edge horn compared with the conventional horn. The increase in the field level in the region of $\phi = 40^o$ to $\phi = 75^o$ is attributed to the diffracted fields at the edges of the capping structure inside the horn. The radiation patterns of the double capped-edge horn are computed at different operating frequencies and are shown in Fig.-5.11.

In this chapter an alternative way of side lobe level reduction is investigated where an elliptic cylinder is used to shield the edges of a conventional horn. Using half a cylinder in capping of the edges is found to cause better performance of the horn than when using a whole cylinder. It is observed that the side lobe levels are reduced in some regions of the field pattern when half a cylinder capping of the edges is used as compared with the field pattern of the conventional horn. The increase in these levels in the back lobe region is caused by the ellipse outer surface acting in this case as guide for the surface currents excited at the ellipse inner edge.This increase is avoided by using another metallic structure to shield the ellipse cylinder capping the edges of the horn. This was done in the double ellipse capped-edge horn of Fig.-5.8.

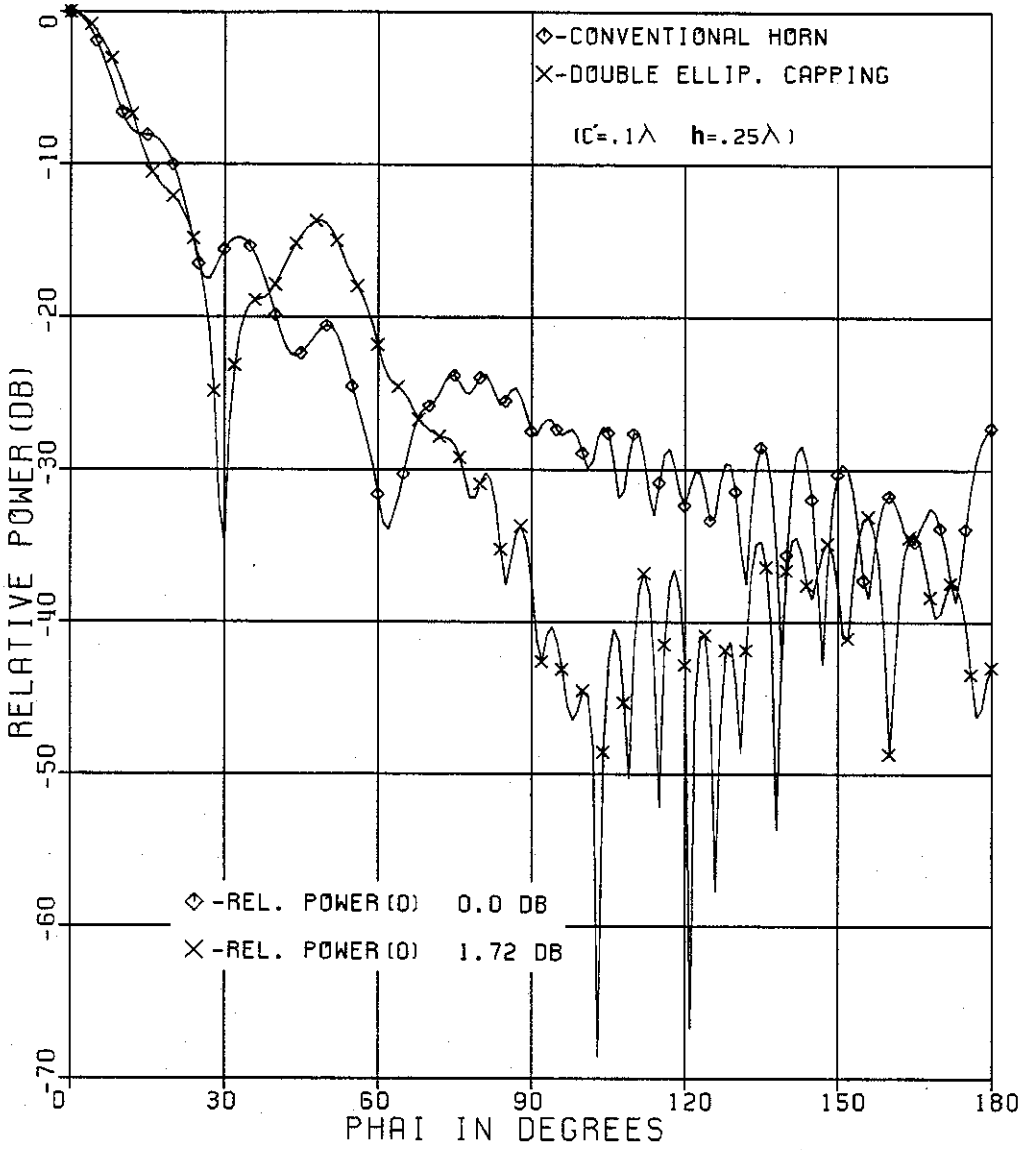

Fig.-5.9 *E*-plane radiation patterns of conventional and double ellipse capped-edge horns for $c' = .1\lambda$, and $h = .25\lambda$.

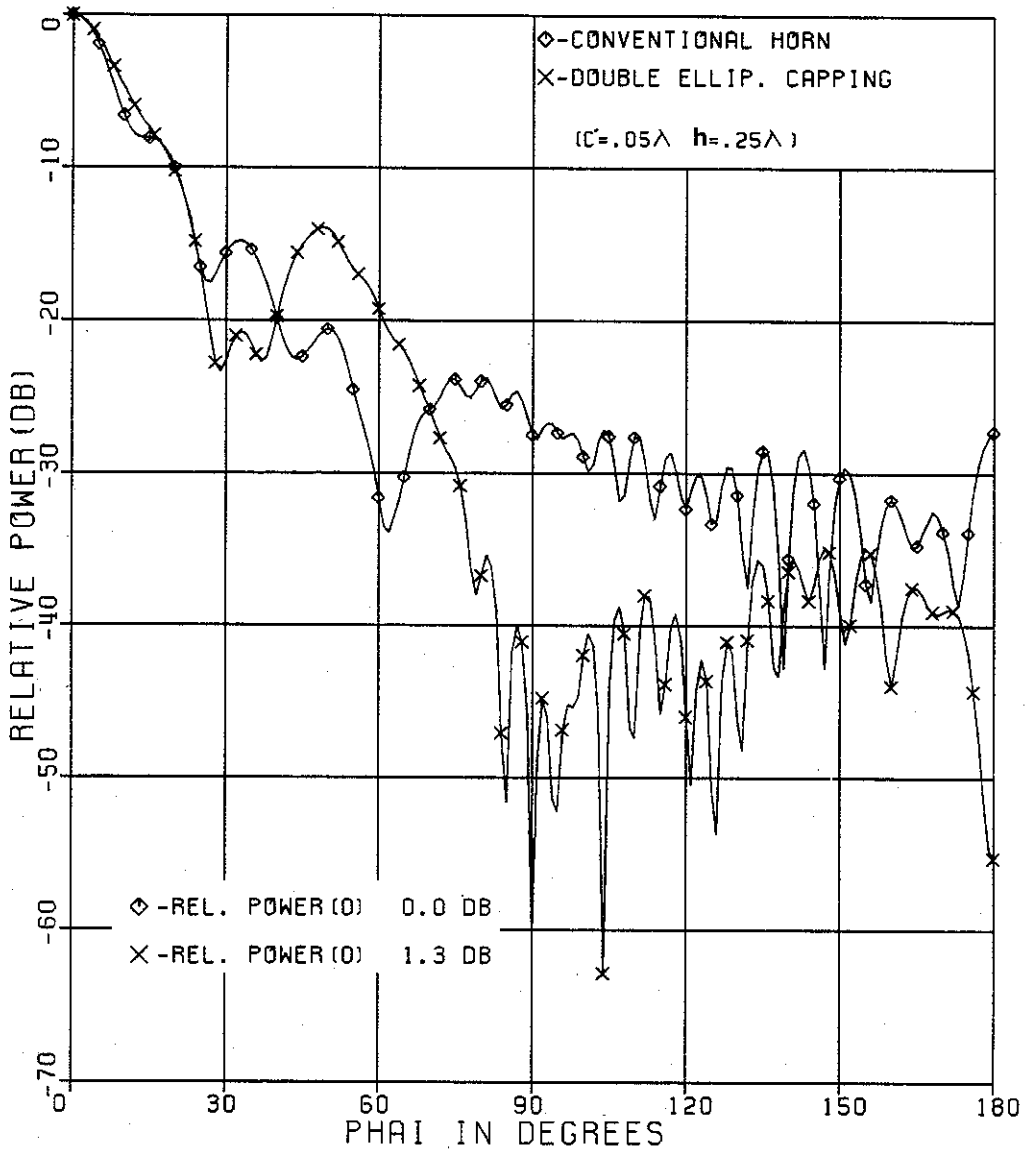

Fig.-5.10 E-plane radiation patterns of conventional and double ellipse capped-edge horns for $c' = 0.05\lambda$, and $h = .25\lambda$.

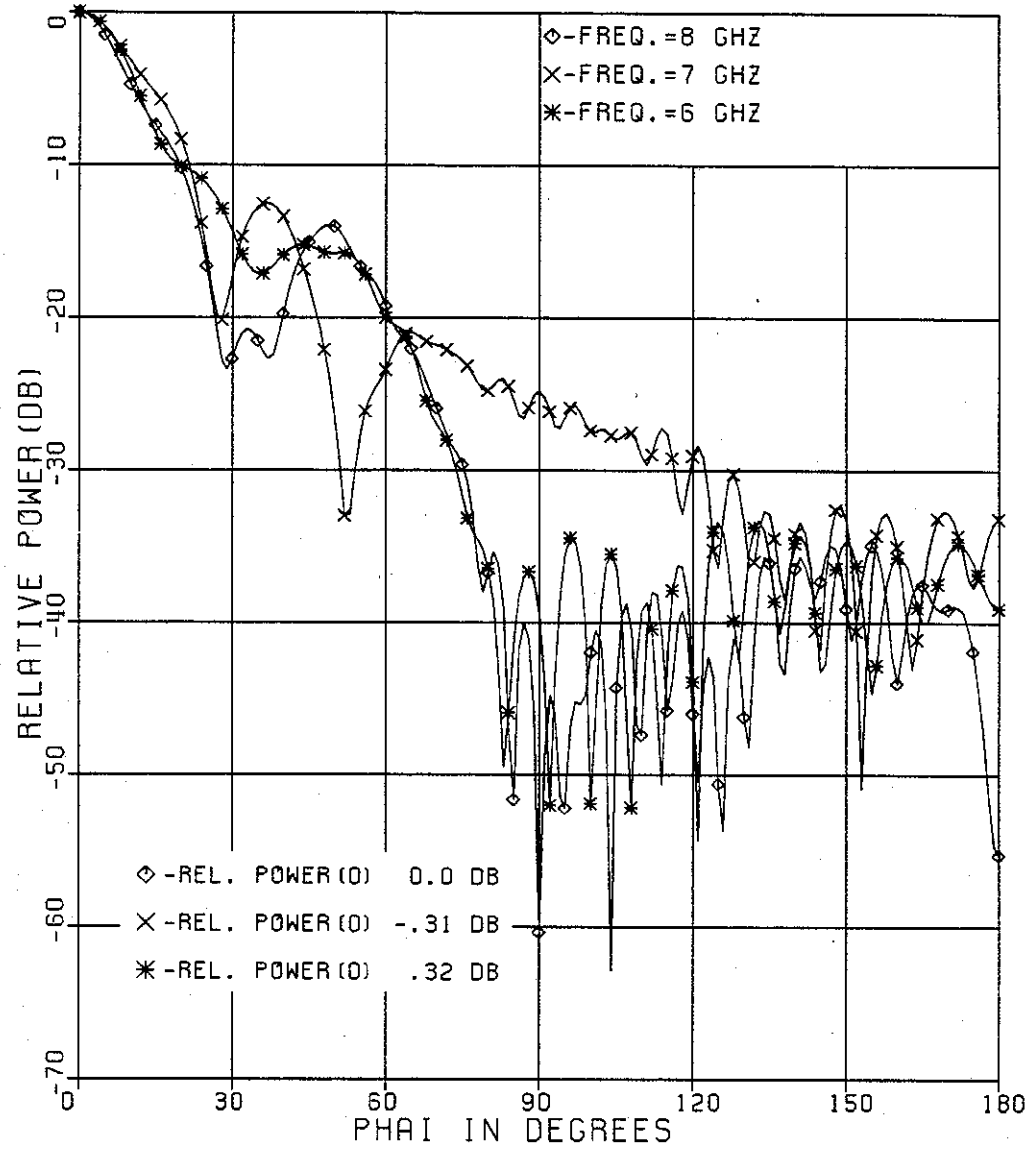

Fig.-5.11 E-plane radiation patterns of a double ellipse capped-edge horn at different operating frequencies, with $c' = 0.05\lambda$, and $h = .25\lambda$ at F=8 GHZ.

CHAPTER VI

Active Loaded Horn Antennas

6.1 Introduction

In earlier chapters different concepts for sidelobe and backlobe level reduction were applied to aperture antennas. One of these concepts is that of multi-mode horns discussed in chapter I. In these horns the sidelobe power level is decreased by reducing the magnitude of the fields incident on the horn edges. This was done by generating fields of a desired mode using a physical passive discontinuity(conductor or dielectric) whose position inside the horn is such that these fields will add with the basic incident field at the horn aperture to reduce the magnitude of the fields at the horn edges to a minimum. Fig.-6.1 shows the addition of TM_{11} and TE_{11} modes at the aperture of a conical horn and the corresponding individual radiation patterns [1].

In this chapter the use of an active discontinuity will be investigated. This is done by using magnetic line sources inside a sectoral horn. The position and phase excitation of these magnetic line sources is optimized to lower the sidelobe and back-lobe power levels. Investigation for the field patterns of such active loaded horn antennas is done numerically using the same numerical formulation of chapter II with a slight modification that takes into account the added magnetic line sources.

6.2 Numerical Formulation.

As discussed in chapter II, the integral equation resulting from the solution of scattering by conducting cylinders can be reduced to a system of N linearly independent equations in the form

$$[A]\,[f] = [g] \tag{6.2.1}$$

where as before [A] is known as the coefficient matrix, [f] is the unknown quantity, and [g] is the known excitation matrix.

As before, an E-plane sectoral horn is simulated by a conducting polygonal cylinder with a finite thickness, as indicated schematically in Fig.-2.2 which shows also the procedure of numbering the segments in a clockwise direction in preparation for a moment method solution. The excitation in this case is a magnetic line source placed at a distance of 0.6λ from the shorted end of the feed waveguide. In addition there are two magnetic line sources placed inside the horn symmetrically about the horn axis at a distance R from the horn edges and at a distance VR from the flared walls of the horn as shown in Fig.-6.2.

Using pulse functions in the expansion of the unknown surface currents, and applying the point matching procedure for testing, the appropriate matrix equation for the present case will be in the form

$$[A_{mn}]\,[F_n] = [G_m] \tag{6.2.2}$$

where G is a vector of length $2S_1$ representing the field incident from the magnetic line sources. These line sources constitute the magnetic line source excitation which as before, has a unity intensity, zero phase and located at a distance ρ_s from the origin of coordinates. The other two line sources have a unity intensity, identical phase excitation, and are located at distances ρ_e and $\rho_{e'}$ from the origin o as shown in Fig.-6.3. In this case the m^{th} element of the excitation matrix [G] will be given by [35]

$$G_m = \frac{-k}{4\eta}\,[H_0^2(k|\rho_m - \rho_s|) + K_1 H_0^2(k|\rho_m - \rho_e|) \tag{6.2.3}$$

$$+ K_1 H_0^2(k|\rho_m - \rho_{e'}|)]$$

where ρ_m is the radial coordinate of the center of segment m, $K_1 = 1e^{j\phi_0}$, and ϕ_0 denotes the corresponding phase excitation. $[F_n]$ is the vector representing the unknown current coefficients, and $[A_{mn}]$ is a $(2S_1)\times(2S_1)$ coefficient matrix with

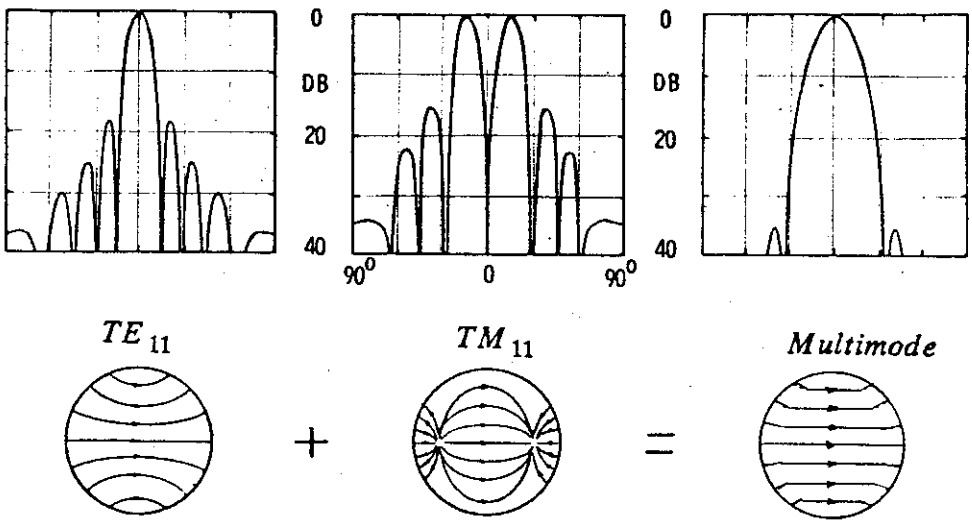

Fig.-6.1 TE_{11} and TM_{11} modes and their corresponding radiation patterns for a dual-mode conical horn.

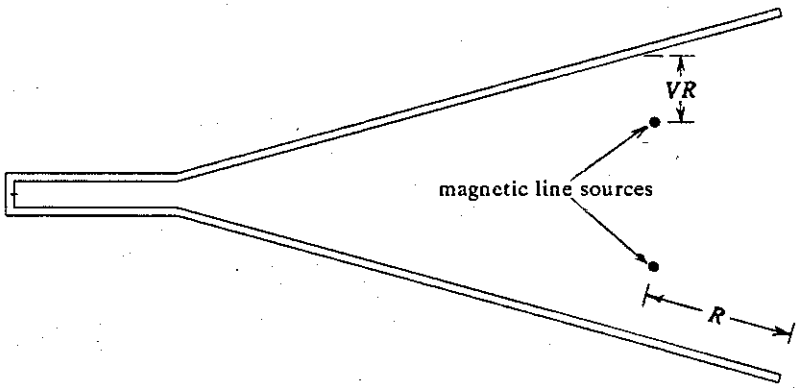

Fig.-6.2 E-plane active loaded sectoral horn antenna with active sources at distances R and VR.

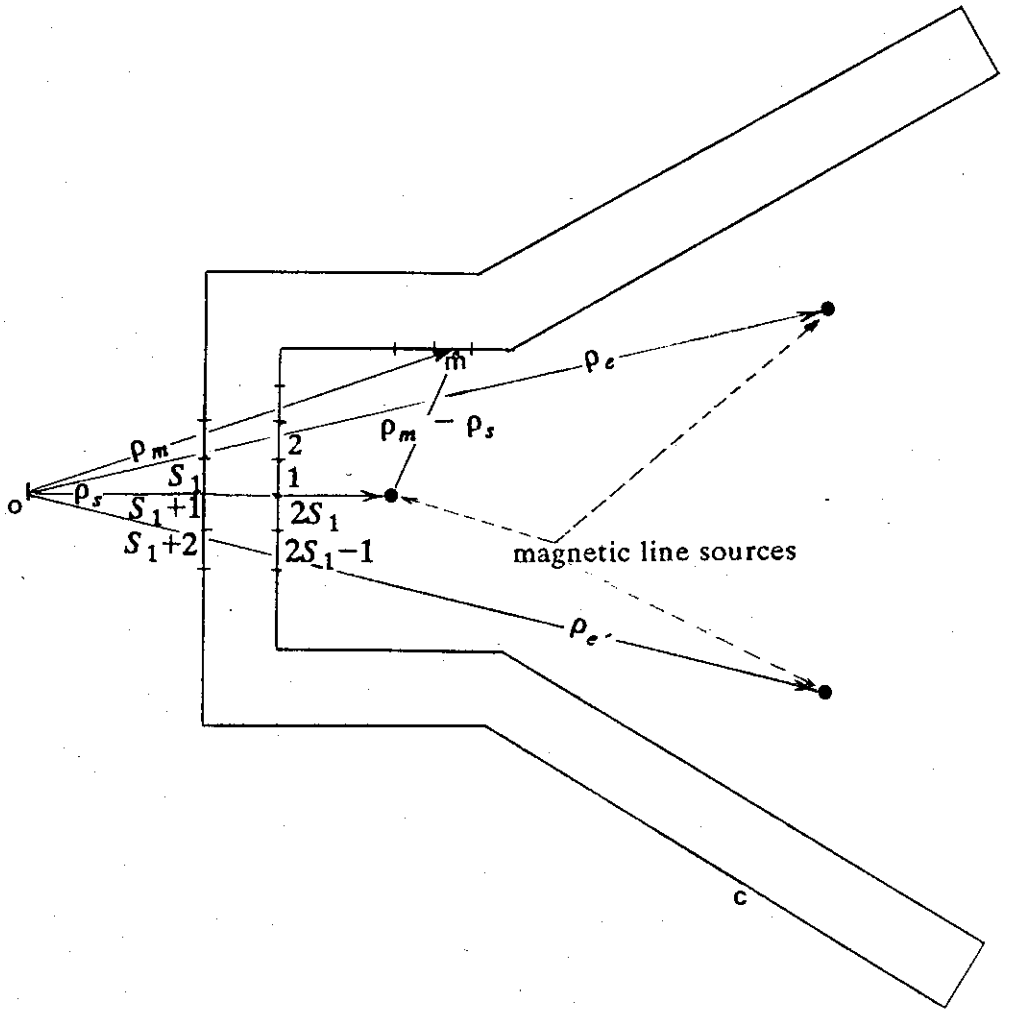

Fig.-6.3 Scattering structure of an E-plane active loaded sectoral horn.

elements defined as before in equation (2.4.4). The symmetry of the structure is also utilized and a procedure similar to that of chapter II is followed using equations (2.4.6)-(2.4.10) to solve for the surface current J_c. Equation (2.4.14) is also used to compute the scattered field of the active loaded horn antenna. The total radiated field at a point $(\rho\ ,\ \phi)$ is obtained as the sum of the incident field plus the scattered field using

$$\mathbf{H}^{tot} = \frac{-k}{4\eta}\ [H_0^2(k|\rho-\rho_s\ |) + K_1 H_0^2(k|\rho-\rho_e\ |) \qquad (6.2.4)$$

$$+ K_1 H_0^2(k|\rho-\rho_{e'}|)] + \mathbf{H}^{sc}(\rho\ ,\ \phi)$$

6.3 Results and Discussions.

The edges of an E-plane sectoral horn are illuminated by fields incident from the feed waveguide of the horn. Adding new sources of **E** field whose corresponding phase is adjusted so as to add destructively with the basic **E** field incident on the horn edges, will reduce the magnitude of the diffracted fields at these edges, and hence reducing the sidelobe and backlobe levels. The choice of magnetic line sources for this application is made since in this case the corresponding **E** field will be in the transverse direction and will lie in the same plane of the basic **E** field.

Two magnetic line sources are placed at distances R and VR inside the same conventional horn used in earlier investigation and shown in Fig.-6.2. Improper positioning of these line sources will increase the magnitude of the edge diffracted fields and hence increasing the sidelobe and backlobe levels. Phase adjustment of the fields at the horn edges is done either by spatial displacement of the line sources or by feeding the line sources with a predetermined phase excitation. Figs.-6.4 and 6.5 show the plots of the far field patterns of an active loaded horn antenna computed for different values of distance R from the horn edges, and for $VR = 0$, together with the field pattern of our conventional horn. These figures shows that placing the line sources at the edges $(R = 0)$ will increase the sidelobe level significantly since

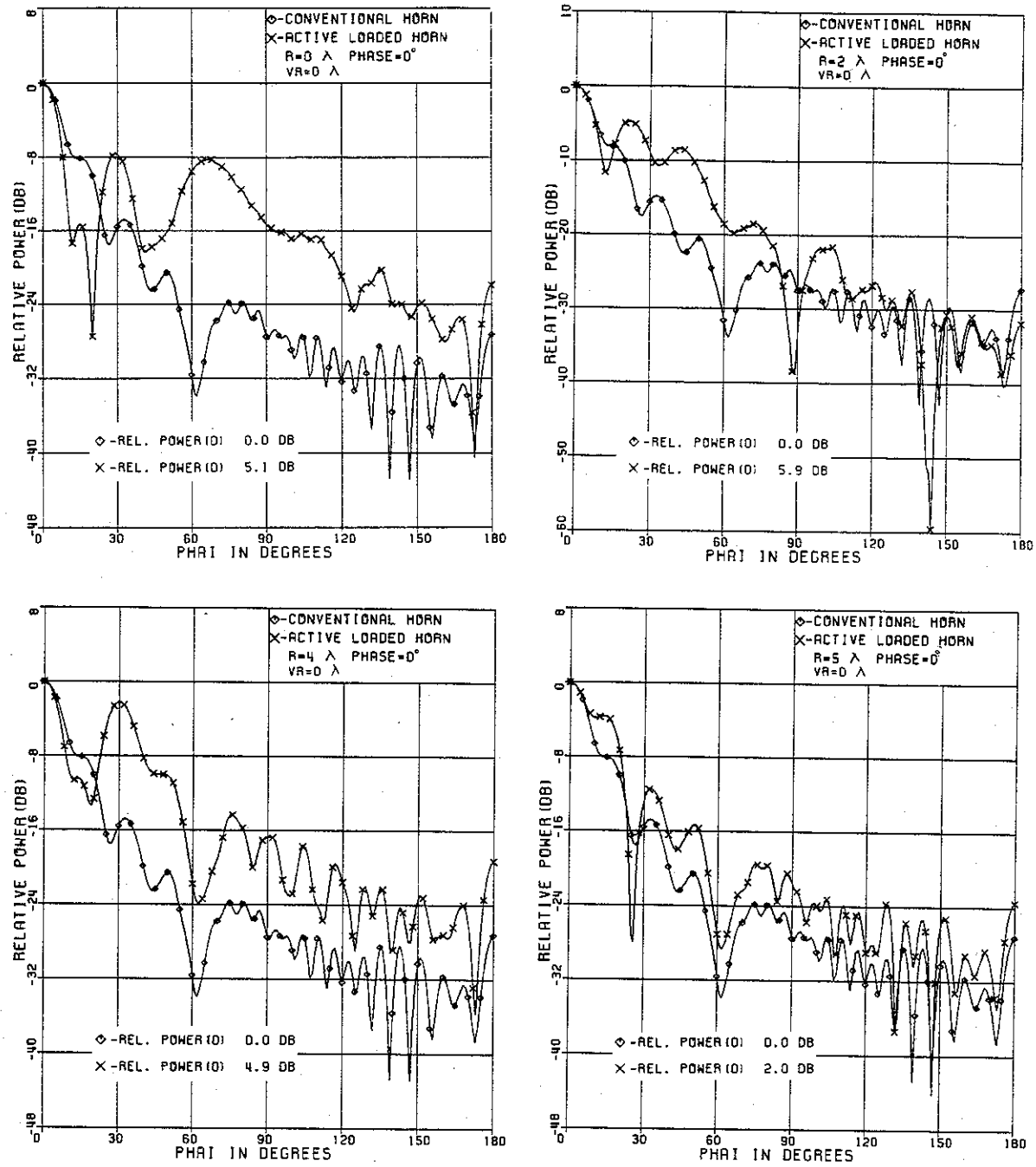

Fig.-6.4 E-plane radiation patterns of the conventional horn and the active loaded horn with $VR = 0$, and $\phi_0 = 0^0$ for different values of distance R.

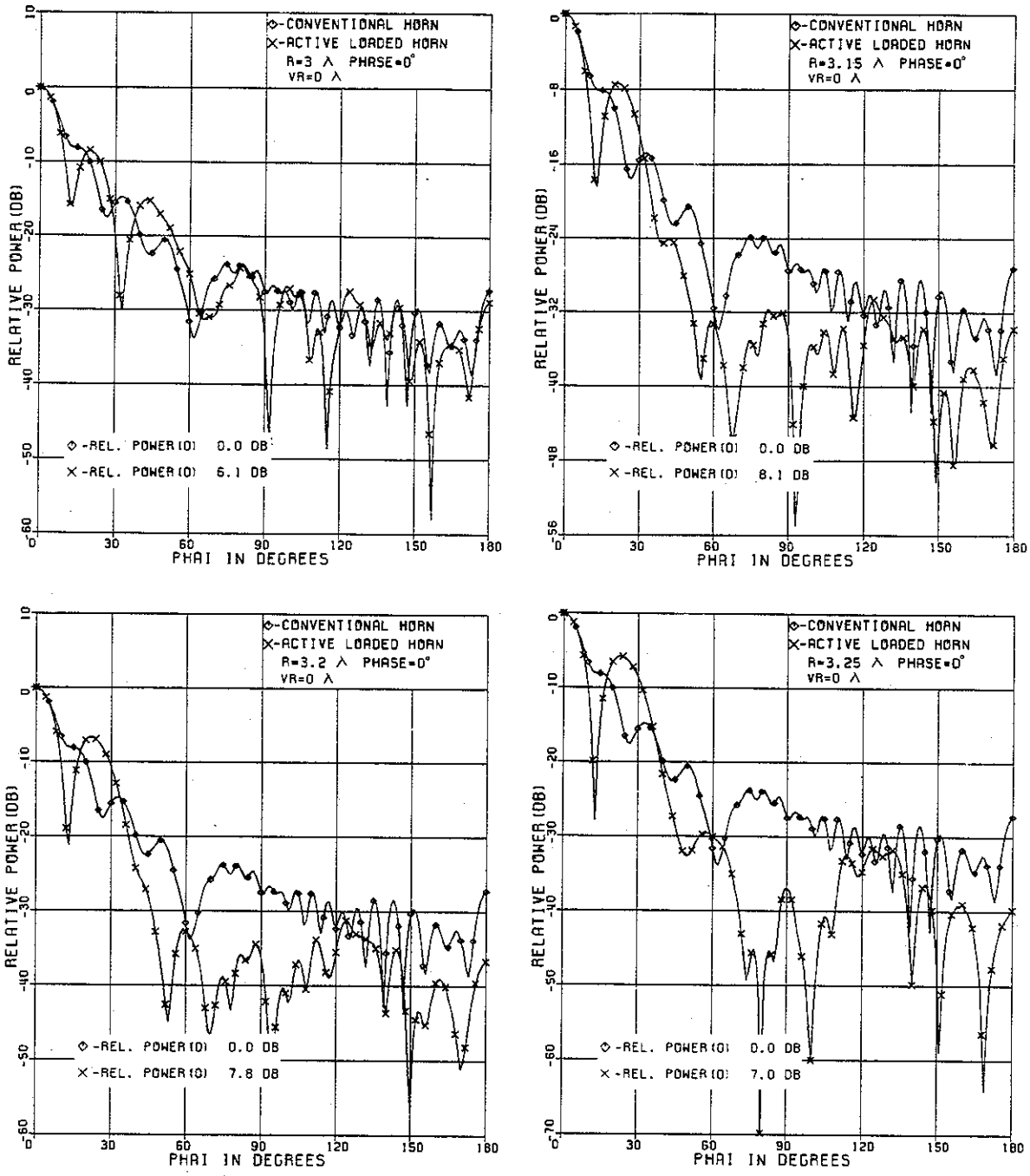

Fig.-6.5 E-plane radiation patterns of the conventional horn and the active loaded horn with $VR = 0$, and $\phi_0 = 0^0$ for different values of an optimized distance R.

these new sources are now radiating with no conducting structures directing their radiations. Fig.-6.5 shows radiation patterns of an active loaded horn compared with the conventional horn for several values of an optimized distance R, $VR = 0$ and zero phase. These plots show a reduction of more than 20dB in the sidelobe and backlobe levels. The increase in the level of the first sidelobe may be attributed to the reflections of the fields incident from the two line sources to the throat region of the horn. The increase of this sidelobe level can be also viewed as due to the magnetic line sources which are moved closer to the inside region of the horn. Changing the phase of the excitation of these line sources will affect also the RPE level of the active loaded horn.

Fig.-6.6 shows plots of the computed radiation patterns of an active loaded horn with the line sources placed at a distance $R = 3.2\lambda$, $VR = 0$ and for phase excitation values of 30^o , 60^o , 90^o, and 120^o, and compared with the conventional horn field pattern. Similar investigation is done also for a value of R equal 3.15λ and the corresponding computed results are shown in Fig.-6.7.

Another spatial freedom can be used to properly position the magnetic line source, and this is done by moving these line sources vertically away from the flared walls of the horn antenna by a distance VR as shown in Fig.-6.2. Field radiation patterns of an active loaded horn antenna for values of $R = 3.15\lambda$, phase excitation of 60^o and for several values of vertical displacement VR are computed, plots of these patterns compared with the conventional horn pattern are shown in Fig.-6.8.

The above computed results show that such active loading of horns is highly dependent on the spatial position and phase excitation of the corresponding line sources yielding a narrow bandwidth horn antenna. This can be seen from the radiation patterns shown in Fig.-6.9 for an active loaded horn with $R = 3.15\lambda$,$VR = .232\lambda$, and phase of 60^o computed at different operating frequencies.

To summarize, the concept of active loading in reducing the sidelobe and backlobe power levels of horn antennas is investigated. A reduction of more than 20dB in the sidelobe level is achieved by such an active loading when the corresponding

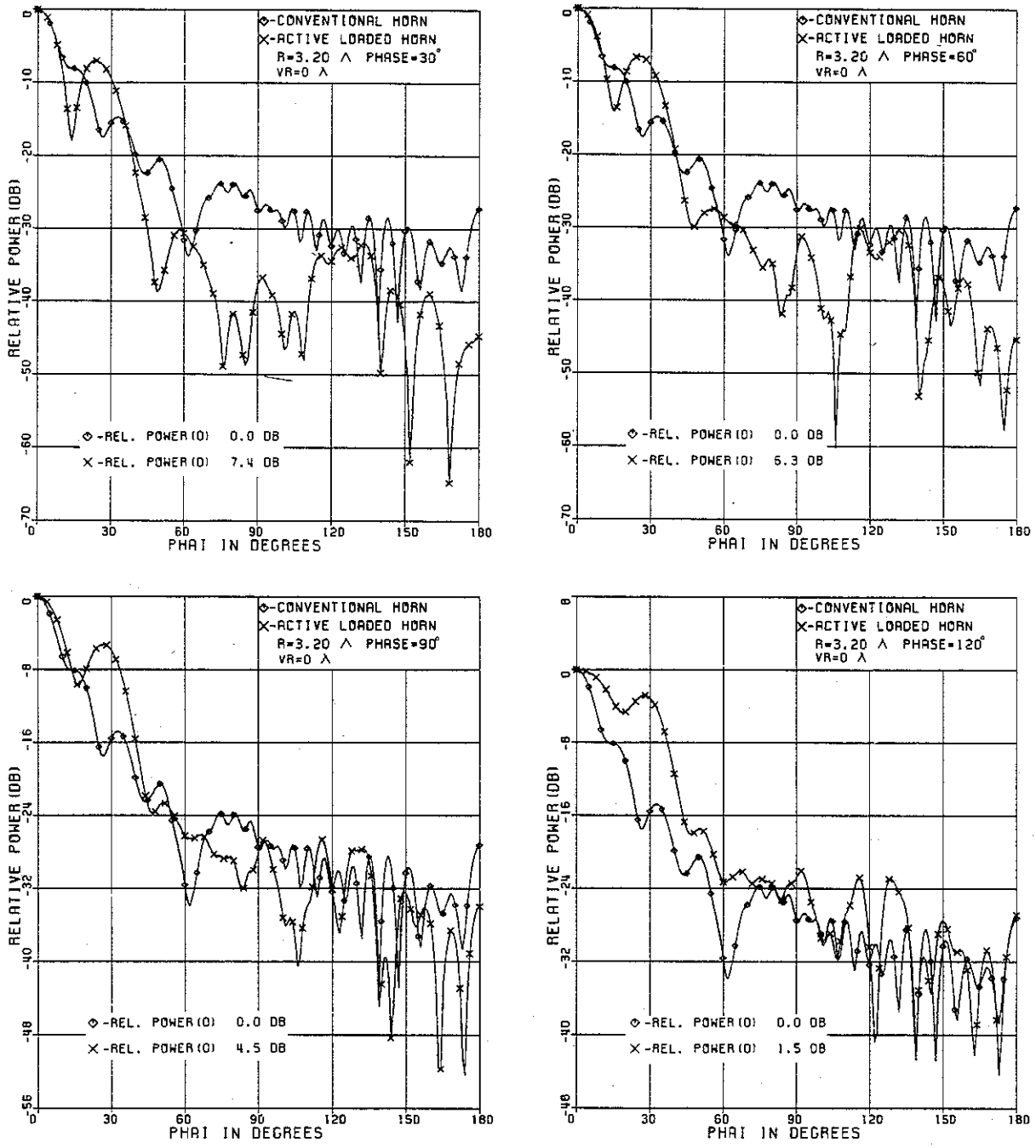

Fig.-6.6 E-plane radiation patterns of the conventional horn and the active loaded horn with $VR = 0$, and $R = 3.2\lambda$ for different values of phase excitation ϕ_0.

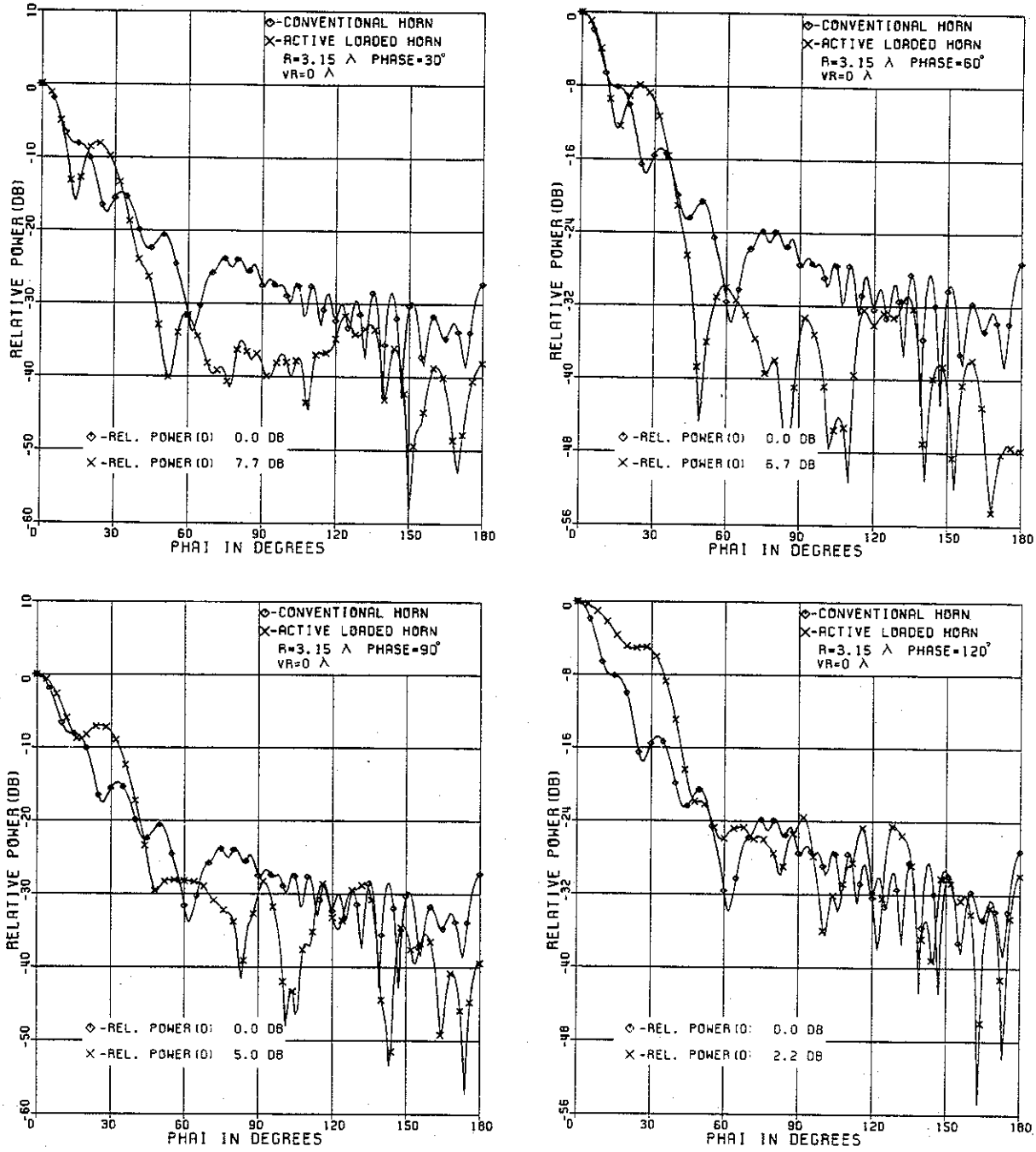

Fig.-6.7 E-plane radiation patterns of the conventional horn and the active loaded horn with $VR = 0$, and $R = 3.15\lambda$ for different values of phase excitation ϕ_0.

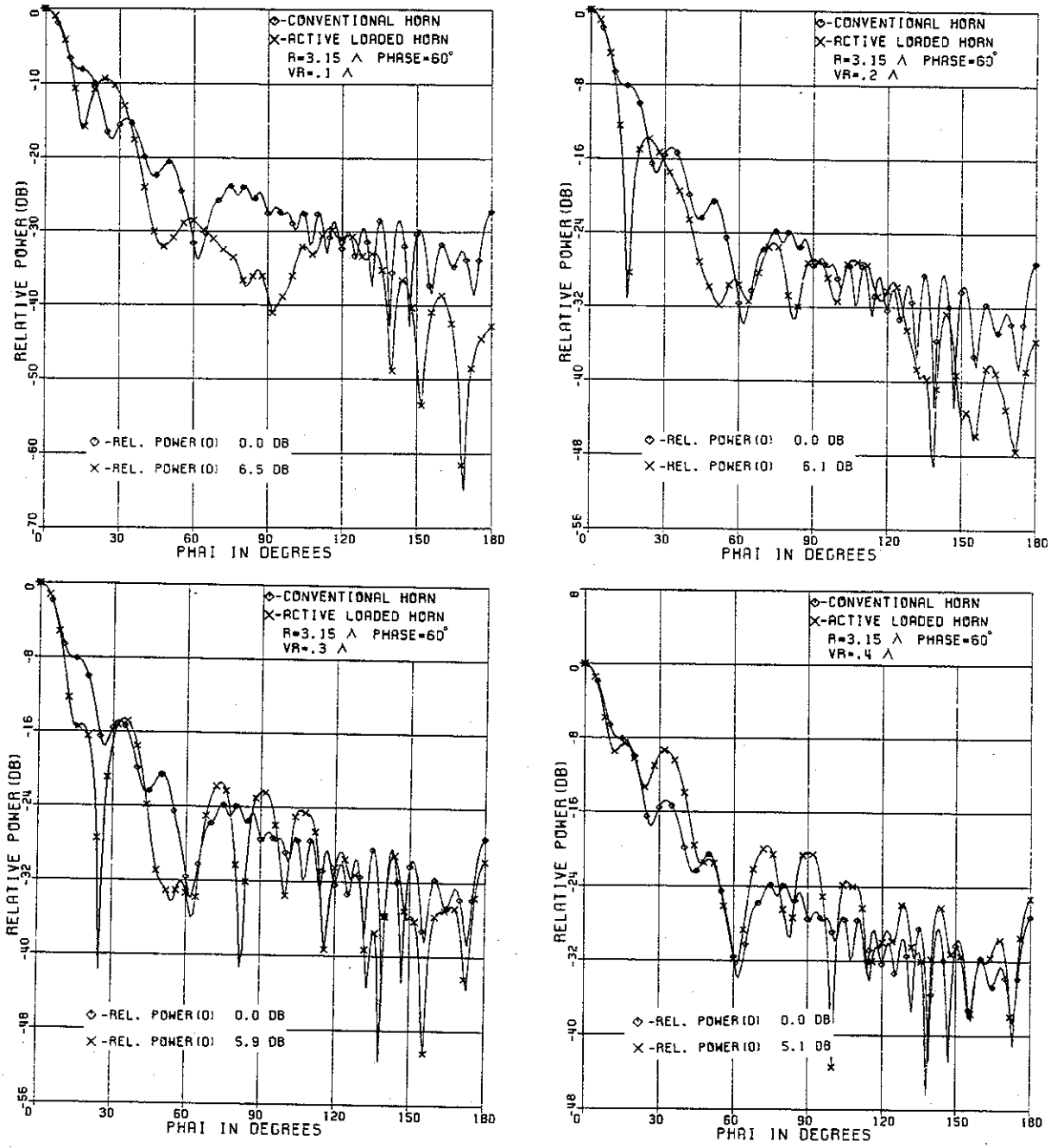

Fig.-6.8 *E*-plane radiation patterns of the conventional horn and the active loaded horn with $R = 3.15\lambda$, and $\phi_0 = 60^0$ for different values of distance VR.

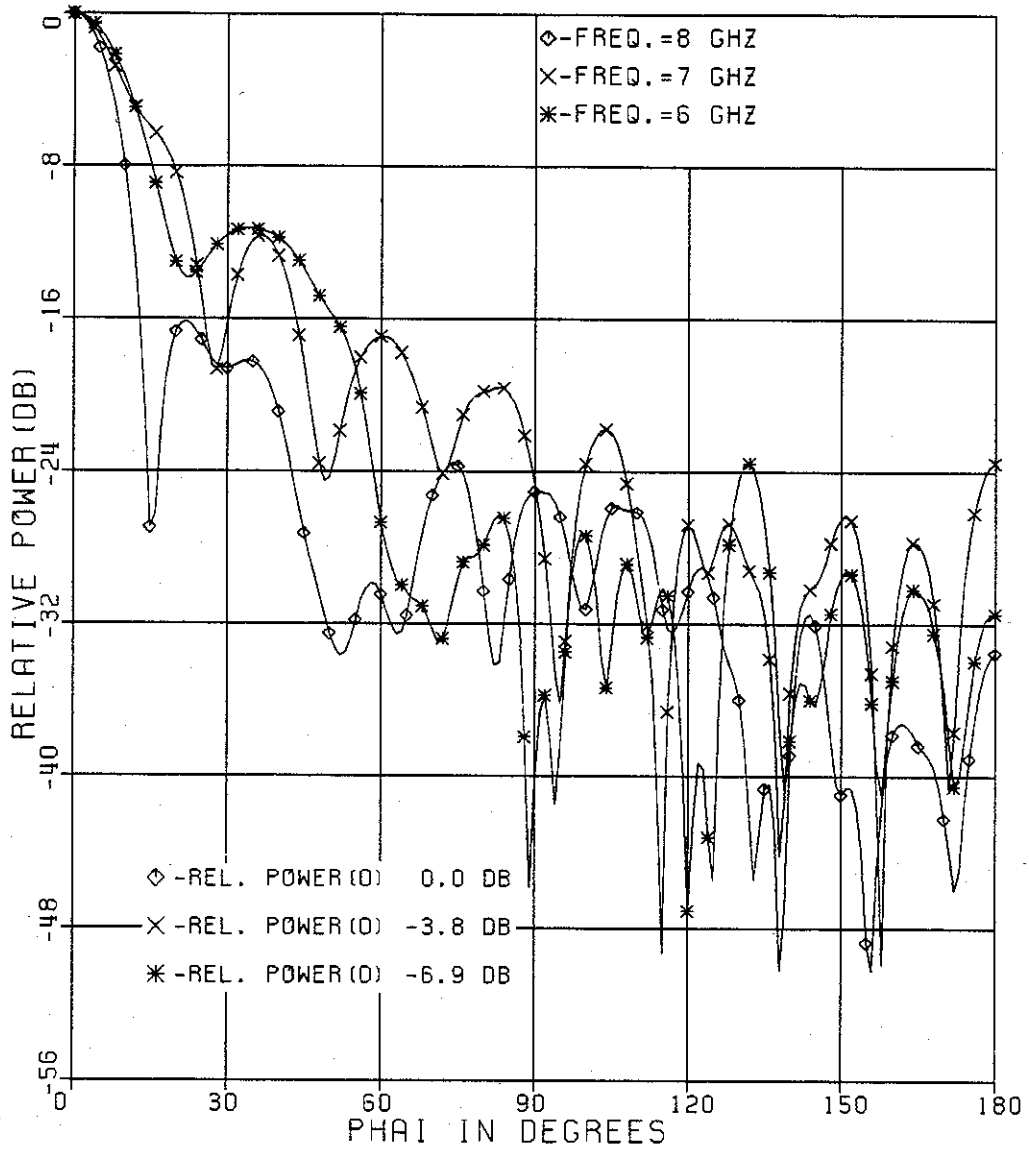

Fig.-6.9 *E*-plane radiation patterns of an active loaded horn with $R = 3.15\lambda$, $VR = .232\lambda$ at F=8GHZ and $\phi_0 = 60^0$ computed at different frequencies.

magnetic line sources are at an optimum position and phase excitation. An increase in relative power of up to 8dB is also observed which is partly due to the additional input power radiated by the active source. A backdraw in such type of antennas is the narrow bandwidth resulting from the requirement of proper phase addition of fields at the horn edges.

CHAPTER VII

Conclusions and Applications

In this thesis different concepts in the reduction of the power levels of sidelobes and backlobes of aperture antennas are investigated by using a moment method numerical approach which treats the antennas as two-dimensional conducting structures excited by a magnetic line source. This is applied for aperture-matched horns, waveguides, and cylindrical reflectors which involves the addition of flat, elliptic, and spiral conducting flanges to the edges of these antennas resulting in a smooth geometric discontinuity that reduces the edge diffracted fields at the aperture. A reduction of more than 10dB is achieved when adding curved flanges to the edges of a horn antenna. When adding relatively large curved conducting flanges at a waveguide edge, a very wide half power beamwidth of up to 160^o and relatively low far sidelobe of levels down to -30dB is achieved. This specific type of radiation pattern comprising a very wide main beam and low backlobes has an application in "compact range" antenna measurements that require illuminating the whole surface of the range reflector with a uniform field pattern(0dB taper) resulting in the uniform field illumination of the test antenna. The size of the test antenna is dependent on the size of the range reflector being uniformly illuminated. With such wide beamwidth achieved by aperture matching of waveguides, electrically large test antennas can be measured indoors. Also having such low backlobes will reduce the interference with the fields emitted from the aperture of the range reflector. Further reduction of these backlobes can be also achieved by adding absorber material on the outer surface of the curved flanges.

Adding curved conducting flanges to the edges of cylindrical reflectors reduces the farlobe power levels down by $10-12$dB using the specific feed illumination of chapter IV. Such a reduction in the farlobes of a satellite ground station antenna will reduce the noise temperature emitted by the ground, and hence improving the

reception quality of the ground station.

Another concept investigated involved capped-edge horn antennas which dealt with adding metallic structures to shield the edges of the horn. The various stages of investigation of such an antenna are reported and a final design achieved a polar shift for the first sidelobe and a sidelobe power level reduction of more than 20dB. In this capped-edge horn one way of holding the elliptic flange shielding the edge of the horn in its position is by filling the space in between by a styrofoam material or by an absorbing dielectric material that may further improve the performance of such an antenna.

A slightly modified numerical formulation is then used to investigate the new concept of active loading of horn antennas. In such antennas two magnetic line sources are held in an optimized position inside the horn and fed with an optimized phase excitation. These line sources radiate fields in a specific mode that add destructively with the TE_{01} mode incident from the feed waveguide at the edges of the horn. A reduction of more than 20dB in the sidelobe level is achieved, while the main beam shape is also improved resulting in a narrower beamwidth. It should be further noted that beam shaping of the radiation patterns of the horn antenna can be also achieved with proper positioning and phase excitation. The same concept can, of course, be extended to include an array of such line sources that will provide a high flexibility in beam shaping of the field patterns of horns. An advantage of such a method of generating new modes for multimode addition over the passive multimode horns is in the flexibility of changing the field pattern shape by adjusting the phase excitation of the line source without any change in their physical position. These magnetic line sources can be obtained by using a long wound coil whose axis is in the z-direction and which can be positioned inside the horn by some material such as styrofoam glued to the inner walls of the horn.

Although the analysis in this thesis is restricted to two-dimensional aperture antennas, the same concepts can be applied to antennas formed from bodies of revolution. These antennas suffer also from edge diffracted fields in a way similar to

two-dimensional antennas. This can be done by a proper numerical formulation specific for such bodies-of-revolution-antennas.

References

[1] Potter, P.D., " A new Antenna with Suppressed Sidelobes and equal Beam widths, " *Microwave J.*, June 1965.

[2] Potter, P.D., and Ludwing, A.C., " Beamshaping by use of Higher Order Modes in Conical Horns, " North west Electron. Res. and Eng. Meeting, pp. 92-93, Nov. 1963.

[3] Jensen, P.A., " A Low-Noise Cassegran Mono-Pulse Feed with Polarization Diversity, " North west Electron. Res. and Eng. Meeting, pp. 94-95, Nov. 1963.

[4] Turrin, R.H., "Dual Mode small Aperture Antennas, " *IEEE Trans. Ant. Prop.*, Vol. AP-15, pp. 307-308, March 1967.

[5] Collin, R.E., **Antennas and Radio Wave Propagation,** McGraw-Hill,U.S., 1985.

[6] Satoh, T., " Dielectric loaded horn antennas, " *IEEE Trans. Ant. Prop.*, Vol. AP-20, No. 3,March 1972, pp. 199-201.

[7] Wong, M.N. and Brandt, C.J., " Conical Horn Antenna Having a Mode Generator, " U.S. Patent no. 4,141,015., February 20, 1979.

[8] Clarricoates, P.J.B and Taylor, B.C., " Evanescent and Propagating Modes of Dielectric-Loaded Circular Waveguides, " *Proc. IEE*, Vol. III, 1964, pp. 1951-1956.

[9] Clarricoates, P.J.B. and Olver, A.D., **Corrugated Horns for Microwave Antennas.** Peter Peregrinus Ltd., IEE series, London 1984, pp. 24-26.

[10] Clarricoates, P.J.B. and Salema C.E.R.C., " Antennas employing Conical Dielectric Horns, Part 1- Propagation and radiation characteristics of dielectric cones. " *Proc. IEE* Vol. 120, No. 7, July 1973, pp. 741-749.

[11] Lier, E., " A Dielectric Hybrid Mode Antenna Feed: A Simple Alternative to the Corrugated Horn. " *IEEE Trans. Ant. Prop.*, Vol. AP-34, No. 1, January 1986, pp. 21-29.

[12] Stanier, J.D., Elsherbeni, A.Z. and Hamid, M., " Modes in a Dielectric Lined Conical Waveguides, " *IEEE* MONTECH'86 Conference on Antennas and Communications, sept. 29 - Oct. 1, 1986, pp. 128-130.

[13] Knop, C.M., Cheng, Y.B., and Ostertag, " On the Fileds in a Conical Horn having an Arbitrary Wall Impedance, " *IEEE Trans. Ant. Prop.*, Vol. AP-34, No. 9, September 1986, pp. 1092-1098.

[14] Rumsey, V.H., " Horn Antennas with Uniform Power Patterns around Their Axis, " *IEEE Trans.*, Vol., AP-14, 1966, pp. 656-658.

[15] Minnet, A.J., and Thomas, B.Mac, A., " A Method of Synthesizing Radiation Patterns with Symmetry, " *IEEE Trans. Ant. Prop.*, Vol. AP-14, pp.654-656, Sept. 1966.

[16] Lawire, R.E. and Peters, L.Jr., " Modification of Horn Antennas for Low Sidelobe Levels, " *IEEE Trans. Ant. Prop.*, Vol. AP-14, September 1966, pp. 605-610.

[17] Freeman, E., **Interference Suppression Techniques for Microwave Antennas and Transmitters,** Artech House Inc., Washington, 1982.

[18] Blacksmith, P.Jr., Method of Reducing Far Out Sidelobes, AFCRC TR57115, ASTIA Document AD 133707, Tech. Report.

[19] Burnside, W.D. and Chuang, C.W., " An Aperture-Matched Horn Design, " *IEEE Trans. Ant. Prop.*, Vol. AP-30, July 1982, pp. 790-796.

[20] Heedy, D.J. and Burnside, W.D., " An Aperture-Matched Compact Range Feed Horn Design, " *IEEE Trans. Ant. Prop.*, Vol. AP-33, November 1985, pp. 1249-1255.

[21] Burnside, W.D., Gilreath, M.C., Kent, B.M. and Clerici, G.L., " Curved Edge Modification of Compact Range Reflector, " *IEEE Trans. Ant. Prop.*, Vol. AP-35, February 1987, pp.176-182.

[22] Johonson, R.C., Ecker, H.A. and Moore, R.A., " Compact Range Techniques and Measurements, " *IEEE Trans. Ant. Prop.*, Vol. AP-17, September 1969, pp. 568-576.

[23] Poogio, A.J. and Miller, E.K., " Integral Equation Solutions of Three-Dimensional Scattering Problems, " Chap. 4 of **Computer Techniques for Electromagnetics,** Pergamon Press, 1973.

[24] Harrington, R.F., **Field Computation by Moment Methods,** The Macmillan Company, New York, 1986.

[25] Mittra, R., **Computer Techniques for Electromagnetics,** Pergamon Press, 1973.

[26] Andreasen, M.G., " Scattering from Parallel Metallic Cylinders with Arbitrary Cross Sections, " *IEEE Trans. Ant. Prop.*, Vol. AP-12, November 1964, pp. 746-754.

[27] Abromowitz, M., and Stegun, I.A., **Handbook of Mathematical Functions,** Apll. Math. ser., Washington, D.C., NBC, 1964.

[28] IMSL(International Mathematical and Statistical Libraries), Inc., 7500 Bellaire Boulevard, Sixth Floor, GNB Building, Huston, Texas 77036.

[29] Schelkunoff, S.A. and Friis, H.T., **Antennas Theory and Practice,** New York, John Wiely & Sons, Appendix VI, 1952.

[30] Kishk, A.A., and Shafai, L., " Effect of Wall Thickness and Aperture Size on the Radiation Characteristics of Circular Waveguides, " ANTEM Symposium on Antenna Technology and Applied Electromagnatics, Augest, 1986.

[31] Balanis, C.A., **Antenna Theory Analysis and Design,** Harper & Row, Publishers, New York, 1982.

[32] Russo, P.M., Rudduck, R.C., and Peters, L.Jr., " A Method for Computing E-Plane Patterns of Horn Antennas, " *IEEE Trans. Ant. Prop.*, Vol. AP-13, March 1965, pp. 219-224.

[33] Kouyoumijian, R.G. and Pathak P.H., " A uniform Geometrical Theory of Diffraction for an Edge in a Perfectly Conducting Surface, " *Proc. IEEE*, Vol. 62, No. 11, November 1974, pp. 1448-1461.

[34] Pathak, P.H. and Kouyoumijian, R.G., " An Analysis of the Radiation from Apertures in Curved Surfaces by the Geometrical Theory of Diffraction, " *Proc. IEEE*, Vol. 62, pp. 1438-1447, 1974.

[35] Harrington, R.F., **Time-Harmonic Electromagnetic Fileds,** McGRAW-HILL COMPANY, New York, 1961.